UC Berkeley
UC Berkeley Electronic Theses and Dissertations

Title
Crust-Lithosphere-Asthenosphere Dynamics in Mantle Plume Provinces with Emphasis on the Galápagos

Permalink
https://escholarship.org/uc/item/7b424658

Author
ORELLANA, FELIPE

Publication Date
2017

Peer reviewed|Thesis/dissertation

eScholarship.org Powered by the California Digital Library
University of California

Crust-Lithosphere-Asthenosphere Dynamics in Mantle Plume Provinces with Emphasis on the Galápagos

By

Felipe Orellana

A dissertation submitted in partial satisfaction of the

requirements for the degree of

Doctor of Philosophy

in

Earth and Planetary Science

in the

Graduate Division

of the

University of California, Berkeley

Committee in charge:

Professor Mark Richards, Chair
Professor Bruce Buffett
Professor Rudolph Wenk
Professor James Sethian

Summer 2017

Abstract

Crust-Lithosphere-Asthenosphere Dynamics in Mantle Plume Provinces with Emphasis on the Galápagos

by

Felipe Orellana

Doctor of Philosophy in Earth and Planetary Science

University of California, Berkeley

Professor Mark Richards, Chair

Hotspot tracks, which most geoscientists attribute to the effects of mantle plumes on the overlying lithospheric plates, are characterized by distinct bathymetry, gravity signatures, structural geology, volcanology, petrology, and geochemistry; motivating us to try to understand the dynamics behind the space-time-histories of these systems. Making use of classical geodynamic paradigms, such as highly-viscous fluids (Stokes flow, for the mantle and/or lithosphere), elastic plate behavior, and heat flow, we develop conceptual frameworks to explain a number of distinct hotspot track features, and present quantitative models aimed at elucidating their origins.

There is much diversity among the population of mantle plume hotspot tracks on the Earth's oceanic crust. For example, there are marked differences in the style of their bathymetry, as well as in their gravimetric signals, and also in the isotopic signature of extruded lavas. At the same time, important underlying differences are given by the age of the lithospheric plates under which the mantle plumes are impinging, lithospheric elastic thickness, the heat (or buoyancy) flux of individual mantle plumes, their melt production, crustal thickening, the proximity of spreading centers, etc. In the first chapter of this dissertation, making use of scaling theory, we show that for most oceanic hotspot tracks, the character of bathymetric expression (primarily rough vs. smooth topography) can be explained by three independent primary underlying factors – plate thickness, or equivalently plate age; plate speed; and plume buoyancy flux – combined into a single parameter, R, the ratio of plume heat flux to the effective thermal capacity of the moving plate overlying the plume.

The Galápagos archipelago (off the west coast of equatorial South America), part of a >20 Ma old hotspot track formed by the underlying Galápagos mantle plume, currently exhibits a broad geographic distribution of volcanic centers of surprisingly variable age, unusual spatial patterns of geochemical enrichment, spectacular and enigmatic bathymetric features, important lithospheric and elastic thickness discontinuities, pronounced regional faults, the presence of the Nazca-Cocos spreading center nearby, and a Nazca plate – Galápagos hotspot relative velocity

that varied through time. These factors have combined to create what is arguably the most complex mantle plume province on Earth, rivaled in this regard perhaps only by the Reunion and the Kerguelen-Ninetyeast hotspot provinces. The present-day Galápagos archipelago sits over a broad massive platform that has been formed primarily by intrusion and secondarily by extrusion, and that exhibits remarkable bathymetric gradients (comparable to those on the Hawaiian hotspot track). In the second chapter of this dissertation we show that some of these bathymetric features may be reasonably explained in the context of thermo-mechanical processes occurring on locally-weak crust/lithosphere, responding to internal gradients in lithostatic stresses, and that these processes of Quaternary history continue to the present day.

Studies in evolutionary biology, dating back to Darwin's famous discoveries, have shown that many of the endemic Galápagos species (flora and fauna) must have evolved from species derived largely from South and Central America. Thus there is much scientific incentive to complement current phylogenetic knowledge regarding the origins of these endemic Galápagos species, with state-of-the-art geophysical models for the emergence and subsidence of the islands habitat on which these species must have evolved, most of which is no longer above sea level ! The third chapter of this dissertation represents a preliminary effort in this direction, combining multiple sources of dynamic topography during and following the formation of the Carnegie/Cocos ridges, which were constructed by the Galápagos mantle plume. We show that plate tectonic reconstructions, mantle plume dynamics, and crustal processes combined can reasonably account for changes in elevation along the Carnegie Ridge, that strongly support the idea that seamounts along most of this ridge were above sea level. In the regard, we note the irony that many Galápagos species, such as the famous marine iguanas, are older than the Galápagos Islands themselves, an observation explained perhaps by understanding the dynamic history of the Galápagos-Carnegie hotspot track through time, conforming to a spatio-temporal progression defined by the Nazca plate – Galápagos hotspot relative motion. These findings coming purely from geophysics, support a likely hypothesis/scenario of South American species migrating over now-submerged paleo-archipelagos along the Carnegie Ridge, finally giving rise to the present-day Galápagos flora and fauna.

Dedication

I dedicate this work to the soft grasses..the plants..the trees and the deep forests..

I dedicate this work to those tiny solid grains in the interplanetary space..to those small planetesimals..that once gave birth to this Earth and the life that on it developed..

Contents Outline

Table of Contents

List of Figures

Acknowledgements

This 6 years-PhD was possible primarily thanks to the financial support of *Comisión Nacional de Investigación en Ciencia y Tecnología*, CONICYT, Chile; a tax-based governmental organization that awarded me a 4-years scholarship including tuition and fees, monthly stipend and partial health coverage. I also want to acknowledge the economic support of the Earth and Planetary Science department here at UC Berkeley, that provided me a regular complementary stipend to accommodate for the cost of living in California. Lastly, I am thankful for the Esper Larsen Fund at UC Berkeley from which I obtained economic support during some of the last semesters of the PhD.

Regarding individuals, I would like to give my greatest thanks to my advisor Prof. Mark Richards, for having invited me to come to Berkeley for the PhD in the first place, and then for his continued support, challenging scientific discussion, and his advice throughout the entire program.
Also very importantly, I would like to express my most sincere gratitude to my second advisor, Prof. Bruce Buffett, for his disposition, kindness and openness to discussion throughout my studies.

I want to thank professors Rudy Wenk and Michael Manga for their complement on my dissertation development.

I also want to thank professor James Sethian from the mathematics department, not only for being part of my committee, but also for his cheerful kindness and scientific support on details.

I am grateful for the crucial computational support of Charley Paffenbarger and Stephen Thompson, for being friendly and helpful system administrators.

I would like to thank the administrative staff that facilitated my legal/financial processes, in particular to Margie Winn and Judith Coyote.

I am also thankful for all my fellow graduate students here at Berkeley, and perhaps in particular I want to thank Tushar Mittal, Robert Martin-Short, Seth Saltiel, William Hawley, Sierra Boyd, Brent Delbridge, Christopher Johnson, Carolina Muñoz, Jesse Hahm, Daniele Rosa and Kevin Driver (postdoc).

Beyond Berkeley, I want to thank Dennis Geist (NSF) and Karen Harpp (U. Colgate, U. Idaho).

Overseas, I would like to thank Prof. Sally Gibson (U. Cambridge, UK) for her helpful criticism and friendly support during all these years.

On the Chilean side, I would like to thank Prof. Eduardo Contreras-Reyes at the Departamento de Geofísica, Universidad de Chile; who provided not only technical advice but also continued

moral support throughout my studies.

Finally, I would like to thank my family (and my extended family) in Chile, for their unconditional support during all these years that I have been abroad. And of course, I am thankful for all my friends, both in Chile and in the USA.

Curriculum Vitae

At the time I started my graduate studies here at UC Berkeley, I had a B.S. in Geophysics and an M.S. in Geophysics, both from Universidad de Chile. During my master's thesis I worked under the guidance of Prof. Denis Legrand, and I worked on earthquake source seismology, primarily focused in modeling rupture histories from a probabilistic point of view; and secondarily I also focused on accelerograms data analysis. Finally I performed an application to invert for the source of the 2001, Peru, Mw=8.4 Arequipa, subduction earthquake.

After graduation, I spent 4 years working in the private industry in Chile, in the realm of applied Geophysics. Firstly I worked in geophysical exploration, specifically and primarily analyzing MT, TEM, Gem and OhmMapper (and secondarily seismics and gravimetry) data to search for minerals, groundwater and lost objects. Secondly, I worked in the geotechnical area, specifically performing numerical simulations in elasto-plasticity in rock mechanics, to understand and assess the stress-strain fields and failure in jointed porous rock masses, all oriented to improve mining operations safety.

During my doctoral studies here at Berkeley, I have focused in tectonophysics and its relation to asthenosphere-mantle convection. Particularly I have focused on the way the asthenosphere, lithosphere and crust exchange mass and thermal energy, with specific attention in the effects observed on the shallow crustal regions, intrusion and extrusion, but most importantly on the bathymetry itself. Aside from this, I spent some time working in planetary dynamos magneto-hydro-dynamics. In summary, I have put most of the emphasis of my PhD on planetary fluid dynamics.

Chapter 1

Rough versus Smooth Topography along Oceanic Hotspot Tracks: Observations and Scaling Analysis

by

Felipe Orellana Rovirosa and Mark Richards

Chapter Abstract

Some hotspot tracks are topographically smooth and broad (Nazca, Carnegie/Cocos/Galápagos, Walvis, Iceland), while others are rough and discontinuous (Easter/Sala-y-Gomez, Tristan-Gough, Louisville, St. Helena, Hawaiian-Emperor). Smooth topography occurs when the lithospheric age at emplacement (LAE) is young, favoring intrusive magmatism, whereas rough topography is due to isolated volcanic edifices constructed on older/thicker lithosphere. The main controls on the balance of intrusive versus extrusive magmatism are expected to be the hotspot swell volume-flux Q_s, plate-hotspot relative speed v, and lithospheric elastic thickness T_e, which can be combined as a dimensionless parameter $R = (Q_s / v)^{1/2} / T_e$, which represents the ratio of plume-heat to the lithospheric heat-capacity. Observational constraints show that, except for the Ninetyeast Ridge, R is a good predictor of topographic character: for R <1.5 hotspot tracks are topographically rough and dominated by volcanic edifices, whereas for R >3 they are smooth and dominated by intrusion.

Orellana-Rovirosa, F., and M. Richards (2017), Rough versus smooth topography along oceanic hotspot tracks: Observations and scaling analysis, *Geophys. Res. Lett.*, 44, 4074–4081, doi:10.1002/2016GL072008.

1.1 Introduction

Many oceanic hotspot track segments can be characterized in terms of smooth or rough topography, likely reflecting the relative roles of intrusive versus extrusive magmatism (absence or dominance of volcanic edifices). The two conspicuous examples that motivated this study are noticeable transitions from rough to smooth topography along the Easter Island hotspot track (rough Easter/Sala y Gomez chains versus broad and smooth Nazca Ridge segment), and the Tristan da Cunha hotspot track (rough Tristan/Gough chains versus relatively smooth Walvis Ridge segment) (see Figures 1.1a and 1.1b). Smooth topography examples, with across-axis widths ≥120 km, include the Rio Grande Rise, the Carnegie/Cocos/Galápagos system, Iceland, the Tuamotu Ridge, Broken Ridge, and various segments along the Ninetyeast Ridge/Kerguelen and Réunion/Chagos/Lacadive track. Gravity studies show that these systems are currently in near-Airy isostatic equilibrium [*Dingle and Simpson*, 1976; *Couch and Whitsett*, 1981; *Pilger*, 1981; *Watts*, 2001; *Hampel et al.*, 2004], and plate tectonic reconstructions show that the lithospheric age of emplacement was young; hence, the overlying plate was thermally thin and rheologically weak, consistent with petrological models for the role of intrusion along young oceanic hotspot tracks [*Farnetani et al.*, 1996; *Richards et al.*, 2013].

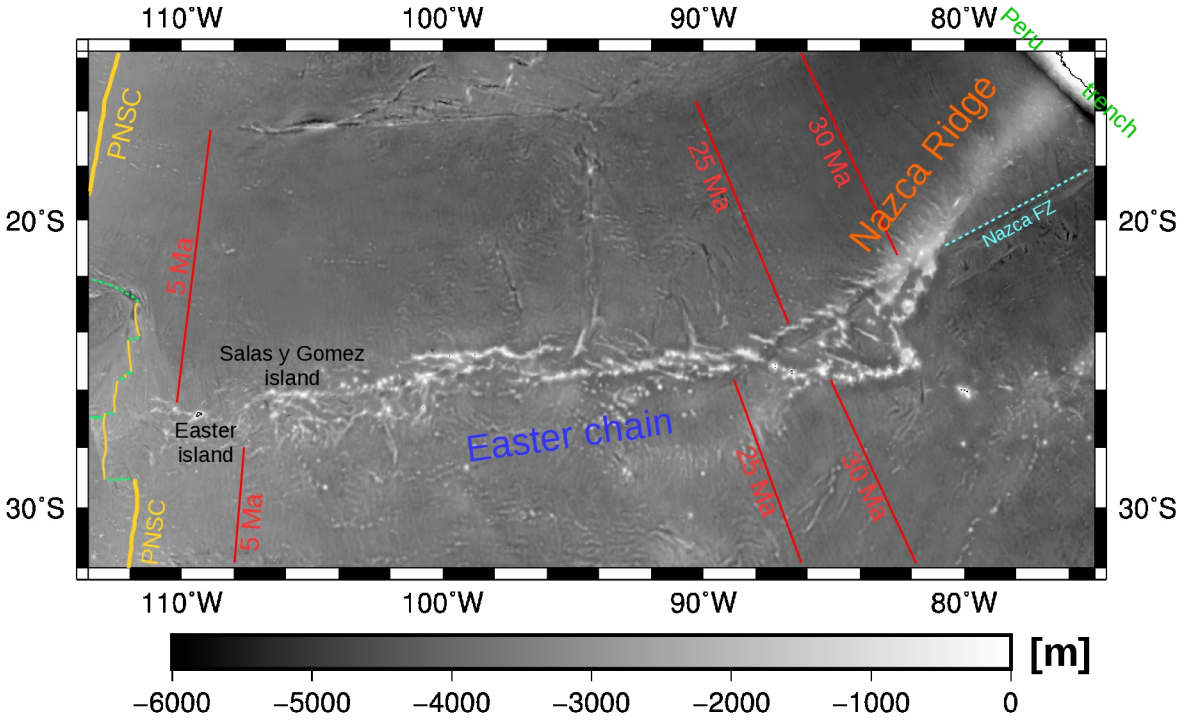

Figure 1.1(a). Topographic map of the Nazca-Easter hotspot track region. Volcanically-active Easter Island and Salas-y-Gomez chain marks the most recent activity of the Easter hotspot beneath lithosphere of age >7 Ma (Figure 1.2). Extending eastward ~2500 km, this initially rough hotspot track exhibits horizontal length scales <40 km. It transitions to the Nazca Ridge, emplaced on very young lithosphere (*Pilger and Handschumacher* [1981]), and characterized by a smooth, elevated topographic rise > 200 km wide (due to thickened crust but absent large volcanic edifices, Figure 1.2), extending another 1000 km northeastward before encountering the Peruvian subduction zone. PNSC stands for Pacific-Nazca spreading center, also known as the East Pacific Rise.

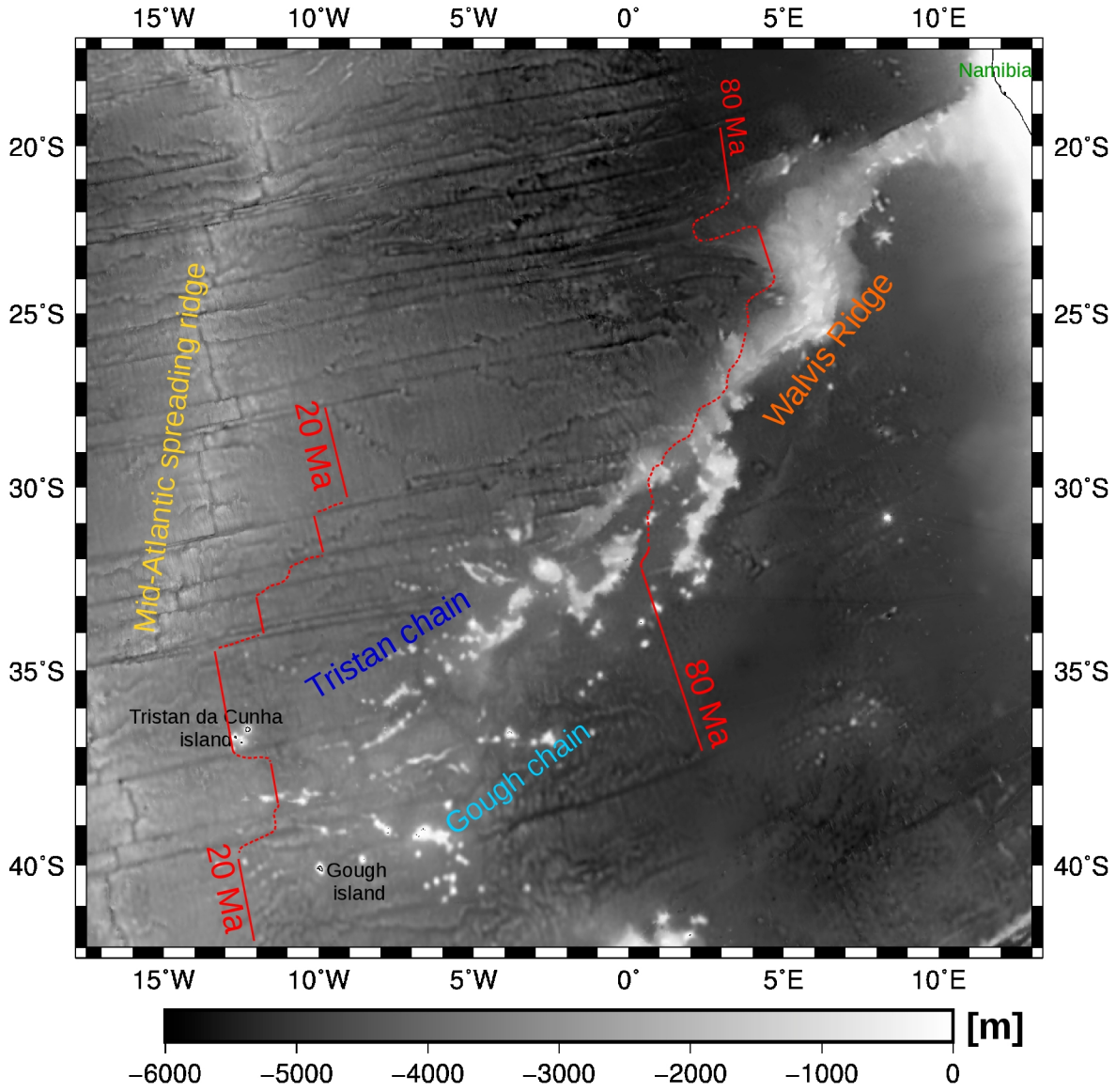

Figure 1.1(b). Topographic map of the Walvis-Tristan-Gough hotspot track region. The broad and smooth Walvis Ridge, off the west coast of Africa, formed as an "near/on-ridge" system starting ~130 Ma ago and is characterized by a smooth, elevated topographic rise ~330 km wide. At about 80 Ma, the westward-moving Mid-Atlantic (spreading) Ridge left (after crossing over) the Tristan hotpot (*Kumar* [1979], *O'Connor and Duncan* [1990], *Sleep* [2002]), the latter producing rough hotspot track topography characterized by islands and seamounts with horizontal length scales <70 km. The Tristan plume is currently active beneath lithosphere of age ~ 22 Ma.

In contrast, other hotspot tracks are relatively rough and discontinuous, dominated by islands and seamounts with horizontal widths ≤ 60 km. Besides the Easter/Sala y Gomez and Tristan/Gough chains, examples include the Louisville chain, St. Helena track, Juan Fernandez Ridge, and most of the Hawaiian-Emperor chain, among many others. These systems were formed on old and

thick oceanic lithosphere [*Pilger,* 1981; *Calmant et al.,* 1990; *Lyons et al.,* 2000, *Hieronymus and Bercovici*, 2001; *Watts,* 2001; *Hillier*, 2007; *Contreras-Reyes et al.,* 2010] with significant elastic lithospheric strength at the time of emplacement.

These distinct styles of topographic/bathymetric expression among different hotspot tracks present an opportunity to better understand the underlying processes controlling hotspot activity. In particular, the abrupt transitions along the two systems illustrated in Figure 1.1 suggest a relatively simple geodynamic explanation in terms of just a few key parameters.

1.2 A Simple Scaling Relation

We hypothesize that smooth hotspot topography occurs when the overlying lithosphere is weak and thin (young), unable to support large volcanic complexes [*Feighner and Richards,* 1994], thus allowing for broadly intrusive magmatism in the lower crust to dominate over extrusion [*Richards et al.,* 2013; *Orellana-Rovirosa and Richards,* 2015]. Accordingly, smooth topography should occur when the thermal energy available from the plume is sufficient to thin the lithosphere as it passes over the plume. To estimate the ratio of available plume heat to lithospheric heat capacity, we consider a strip of hot, buoyant plume material (as in *Sleep* [1996]) of thickness s beneath a plate of thickness T_e that is moving at relative speed v, generating a topographic swell of width L (perpendicular to the motion of the plate) and average height h. Assuming that isostatic balance holds roughly at the horizontal length scale of the swell, we have

$$s \cdot (\rho_m - \rho_p) \cdot g = h \cdot (\rho_m - \rho_w) \cdot g \qquad (1)$$

where g is the acceleration of gravity, and the densities ρ_m , ρ_p and ρ_w are, respectively, those of the mantle, the hot plume material, and water (assuming submerged topography). Multiplying by the swell width L and plate velocity v, assuming that the mantle plume density difference is due to the average excess plume temperature $\theta_p - \theta_m$ with thermal expansivity α_v , we obtain

$$s \cdot L \cdot v \cdot \rho_m \cdot \alpha_v \cdot (\theta_p - \theta_m) = h \cdot L \cdot v \cdot (\rho_m - \rho_w) \qquad (2)$$

or
$$s \cdot L \cdot v \cdot \rho_m \cdot C_p \cdot (\theta_p - \theta_m) = (C_p / \alpha_v) \cdot h \cdot L \cdot v \cdot (\rho_m - \rho_w) \qquad (3)$$

where the heat capacity is C_p. The left side of this equation is just the plume excess heat-flux, thus

$$\dot{U}_P = (C_p / \alpha_v) \cdot h \cdot L \cdot v \cdot (\rho_m - \rho_w) \qquad (4)$$

Defining $\dot{U}_L$ as the thermal energy rate necessary to raise the overlying lithospheric mantle temperature to that of the underlying mantle, θ_m (at the base of the elastic lithosphere), and

approximating a roughly linear geotherm with θ_M right at the Moho (and uppermost mantle), we obtain the rate of heating necessary to effectively 'remove' the overlying lithosphere

$$\dot{U}_L = L \cdot T_e \cdot v \cdot \rho_m \cdot C_p \cdot (\theta_m - \theta_M)/2 \qquad (5)$$

or $\dot{U}_L = L \cdot T_e \cdot v \cdot (C_p/\alpha_v) \cdot (\rho_M - \rho_m)/2$ (after multiplying through by α_v/α_v) (6)

where ρ_M, ρ_m are reference temperature-dependent densities of the lithospheric mantle (at the corresponding temperatures). We now form the heat flux ratio

$$R_0 = \dot{U}_p / \dot{U}_L = (h/T_e) \cdot 2 \cdot (\rho_m - \rho_w)/(\rho_m - \rho_M) \qquad (7)$$

We expect that when R_0 is large (>1), the lithosphere will be thermally reset by the plume, resulting in a larger fraction of magmatic intrusion into the crust, and hence relatively smooth topography.

Unfortunately, the scarcity of published estimates of hotspot-swell heights *h* (aside from *King and Adam* [2014]), renders the above formula somewhat impractical. Therefore, we instead consider a closely-related scaling formulation: Recognizing the swell volume flux $Q_s = L \cdot h \cdot v$ as the surface expression of the plume buoyancy, we consider the alternative dimensionless ratio:

$$R = \sqrt{(Q_s/v)} \; / \; T_e \qquad (8)$$

(We noted at the outset that Q_s, v, and T_e would likely be the main controlling independent variables for any particular hotspot track, so that they could likely be combined into a dimensionless group sufficient to characterize the observations). The numerator of this function is the geometric-mean linear dimension of the swell cross-section. Statistical analysis of the hotspot swell data compiled by *King and Adam* [2014], as well as some theoretical considerations, suggest the function $(Q_s / v)^{1/2} = (L \cdot h)^{1/2}$ is approximately proportional to *h*, the average swell height (see additional figures at the end of the chapter). Thus, the dimensionless parameters R_0 and R are both approximately proportional to h/T_e, and hence to each other, so that both characterize the ability of the plume to thermally erode the overlying lithosphere, and may suffice to predict a plume's topographic expression. Because estimates for Q_s, v, and T_e have been compiled for hotspot tracks by numerous authors (Figure 1.2), we examine how smoothness and roughness are correlated with estimated values of R along different oceanic hotspot tracks.

1.3 Results

Figure 1.2 contains data on hotspot tracks for which the parameters in the scaling relation for R are sufficiently constrained in the literature, and uses various symbols to indicate the character of topography – smooth (orange circles), rough (blue diamonds), and transitional (brown squares). R is computed for topographically-coherent segments along individual hotspot tracks. Figure 1.3 plots these estimates of R versus the estimated lithospheric age at emplacement (LAE). Figures 1.2 and 1.3 show a largely consistent relation between R and topographic character: for $R < 1.5$ topography tends to be rough, for $1.5 < R < 3$ topography is transitional, and for $R > 3$ topography tends to be smooth, consistent with the energy ratio hypothesis contained in the formulations for R_0 and R in the previous section. Exceptions to these trends are treated in the discussion section.

	age [Ma]	Qs [m3/s]	v [cm/yr]	Te [km]	LAE [Ma]	R	+-R Error	Bathymetry	HTL [km]
Nazca	43	0.42 ?	7.39	3.5 ?	0 ?	**3.83**	-1.5 , +2.0	S	200-240
Nazca	35	0.42	7.39	3.5	0	**3.83**	-0.7 , +1.0	S	100-200
Trans	26.5	0.42	8.32	3.5	0	**3.61**	-0.5 , +0.6	T	30-150
Easter	15	0.84	9.25	6.2	3.04	**2.73**	-0.4 , +0.4	R	< 40
Easter	0	0.84	9.25	9.4	7.0	**1.80**	-0.3 , +0.3	R	< 35
Walvis	130	0.531 ?	2.8	7.5 ?	0 ?	**3.26**	-1.5 , +2.0	S	200-250
Walvis	100	0.531	2.8	7.5	0	**3.26**	-1.0 , +1.3	S	200-270
Trans	80	0.531	2.62	7.5	0	**3.37**	-0.6 , +0.8	STR	50-190
Tristan-Gough	40	0.332	2.44	11.6	10.8	**1.79**	-0.4 , +0.5	R	30-70
Tristan-Gough	0	0.390	2.44	16.45	21.5	**1.37**	-0.3 , +0.4	R	10-30
Louisville	60	0.698	4.5	22.5	40	**0.98**	-0.4 , +0.5	R	< 50
Louisville	35	0.698	7.4	26.3	55	**0.66**	-0.3 , +0.4	R	< 60
Louisville	12.5	0.698	6.4	24.5	47.5	**0.76**	-0.2 , +0.3	R	< 35
Louisville	0	0.698	6.4	19.4	30	**0.96**	-0.2 , +0.3	R	< 10
Carnegie	15	0.11 ?	3	4.5	0	**2.39**	-1.5 , +2.0	ST	50-100
Galapagos	5	0.33	3.7	5	2	**3.36**	-0.6 , +1.0	S	120-180
Galapagos	0	0.33	3.7	11.8	11	**1.42**	-0.3 , +0.5	T	50-100
Iceland	9	0.32 ?	0.5 ?	4.5 ?	0 ?	**9.99**	-4.0 , +10.0	S	400-470
Iceland	0	0.64	0.5 ?	15.9	20	**4.00**	-1.5 , +6.0	S	400-470
Hawaii	47	1	6.27	31.8	80	**0.71**	-0.3 , +0.3	R	20-50
Hawaii	30	2.5	6.27	32.3	82.9	**1.10**	-0.2 , +0.2	R	15-80
Hawaii	15	7.5	9.2	32.8	85.4	**1.55**	-0.2 , +0.2	T	120-160
Hawaii	8	4.2	9.2	33.03	86.6	**1.15**	-0.1 , +0.2	R	40-90
Hawaii	2	12.5	9.2	33.2	87.6	**1.97**	-0.1 , +0.2	T	160-200
Hawaii	0	3.02	9.2	33.3	88	**0.97**	-0.1 , +0.2	RT	100-140
Ninetyeast	77	0.18 ?	10	7.9	5	**0.95**	-0.5 , +2.0	ST	160-250
Ninetyeast	73	0.18 ?	10	5	0	**1.51**	-0.5 , +2.0	ST	200-300
Ninetyeast	62	0.18 ?	12	5	0	**1.38**	-0.5 , +1.5	ST	100-150
Ninetyeast	55	0.18 ?	12	5	0	**1.38**	-0.5 , +1.0	ST	140-240
Ninetyeast	45	0.18 ?	7	13.7	15	**0.66**	-0.5 , +1.0	ST	140-240
St. Helena	50	0.16	2.2	16.80	22.5	**0.90**	-0.8 , +1.0	R	10-40
St. Helena	20	0.27	2.15	20.19	32.5	**0.99**	-0.6 , +0.8	R	10-50
St. Helena	0	0.13	2.1	20.95	35	**0.67**	-0.3 , +0.4	R	< 40
Reunion	40	0.233 ?	3.4 ?	4	0	**3.67**	-1.5 , +2.0	S	170-280
Reunion	30	0.465	2.8	14.8	17.5	**1.55**	-0.5 , +0.8	ST	100-200
Reunion	20	0.465	2.5	23.8	45	**1.02**	-0.4 , +0.6	T	80-180
Reunion	0	0.465	1.9	27.4	60	**1.01**	-0.3 , +0.4	T	90-150

Figure 1.2: Summary information for the hotspot tracks with sufficient published constraints: Left to right: hotspot track age [Ma], swell volume flux Q_s [m^3/s], plate-hotspot horizontal relative speed v [cm/yr], lithospheric elastic thickness T_e [km], lithospheric age at emplacement LAE [Ma], non-dimensional function R, approximate error estimates on R, qualitative topographic style assessment (coded as in Figure 1.3), characteristic horizontal (transverse) topographic length-scale HTL [km]. Away from spreading centers, T_e was computed using the age-dependent thickness defined by the 450ºC isotherm, following *Watts* [1978].

Corresponding published values of T_e were used at spreading centers. For the swell volume-fluxes Q_s a factor of ½ is applied for on-ridge systems. Exceptions are Walvis ridge where the on-ridge value at 80 Ma is taken from *Adam et al*. [2007], and Galápagos where a tentative 1/3 factor was used when the hotspot was located mainly on the Cocos plate side.

The results of Figure 1.3 show some scatter in the relation between bathymetric character and *R*, which is not unexpected given uncertainties in the underlying data. Additionally, magma emplacement mode (intrusion versus extrusion) may also depend upon other lithospheric properties not captured by *R*, since lithospheric properties are not solely dependent upon age or elastic/thermal thickness. For example effective lithospheric permeability to melt transport (e.g., via fractures and diking) is poorly understood and may depend upon the state of stress. Episodes of plate-motion reorganization likely cause abrupt stress-field changes, and hence changes in fracture-density. Pacific-Nazca plate motion reorganization between 30 and 25 Ma (*Pilger and Handschumacher* [1981]), which caused only a slight bend in the Hawaiian and Louisville ridges (*Lonsdale* [1988], *Wessel and Kroenke* [2009]), appears to have coincided with a dramatic change in the Nazca-Easter system, wherein several branches of elongated bathymetry may be the result of lithospheric fractures (such as the one aligned with the Nazca fracture zone; see Figure 1.1a).

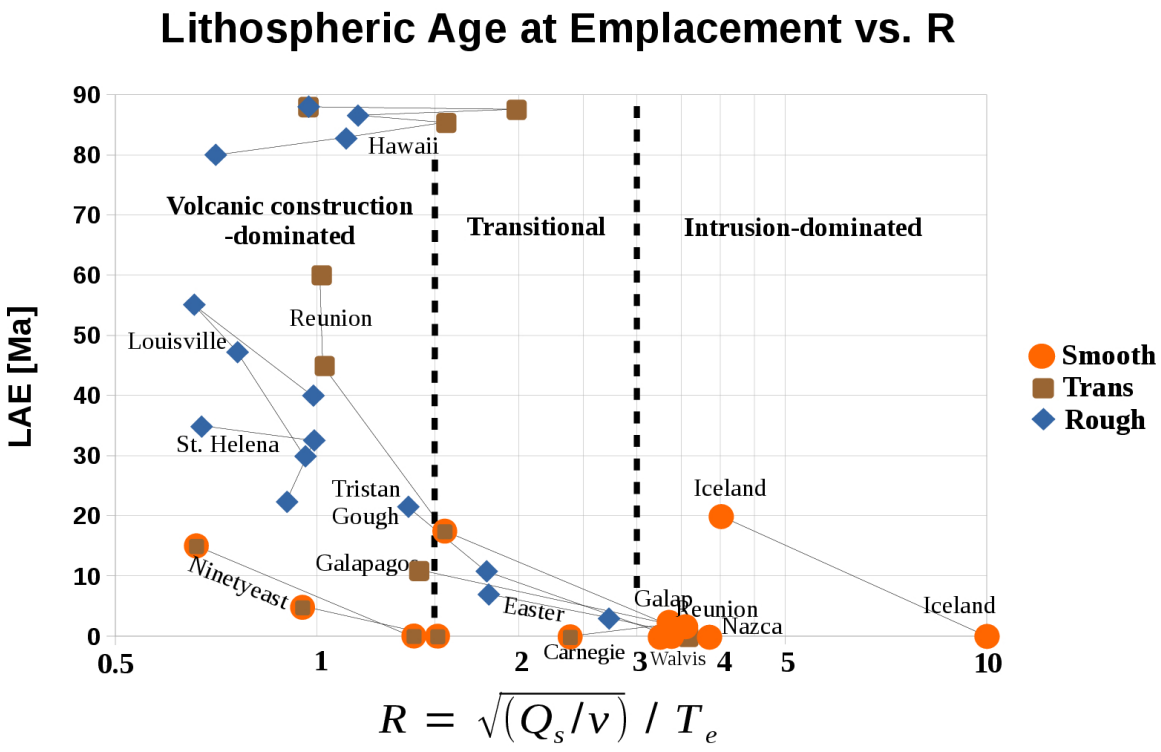

Figure 1.3. Lithospheric age at time of magma emplacement LAE [Ma] versus the dimensionless heat flux ratio *R*, from data in Figure 1.2. Symbols indicate the topographic style. Away from spreading centers, the lithospheric elastic thickness $T_e \sim (\mathrm{LAE})^{1/2}$. The Hawaiian plume appears as an outlier due to a much older LAE and a very high buoyancy flux. There is an overall trend: the systems become smoother as *R* increases.

Figure 1.2 also lists a measure of the characteristic range of horizontal lengthscales for each hotspot track segment, labeled the Horizontal Topographic Lengthscale (HTL). These HTL ranges represent systematic estimates of the horizontal linear dimension of the characteristic topographic features, taken in the across-track direction for smooth (continuous) tracks, and in any direction for isolated volcanic edifices (rough tracks). Figure 1.4 indicates the expected tendency for HTL to increase as the heat flux ratio *R* increases. This relation also implies topological changes: At low *R* values the seamounts are small, isolated and disconnected from each other; as *R* increases they are broader and more frequent (more closely spaced) leading to increased connectivity (this connectivity of the bathymetric bumps also implies their overlapping). Above a threshold of *R*~3, the topographic features are essentially broad platforms, with most magmatism being intrusive (*Feighner and Richards* [1994], *Richards et al.* [2013], *Orellana-Rovirosa and Richards* [2015]). Deviating from this trend (red bars) are the Ninetyeast Ridge (with HTL up to 300 km), and to some extent Reunion (with HTL up to 180 km) and the transition region along Nazca-Easter (HTL as low as 30 km), all of which were influenced by pre-existing fracture zones (see section 1.4).

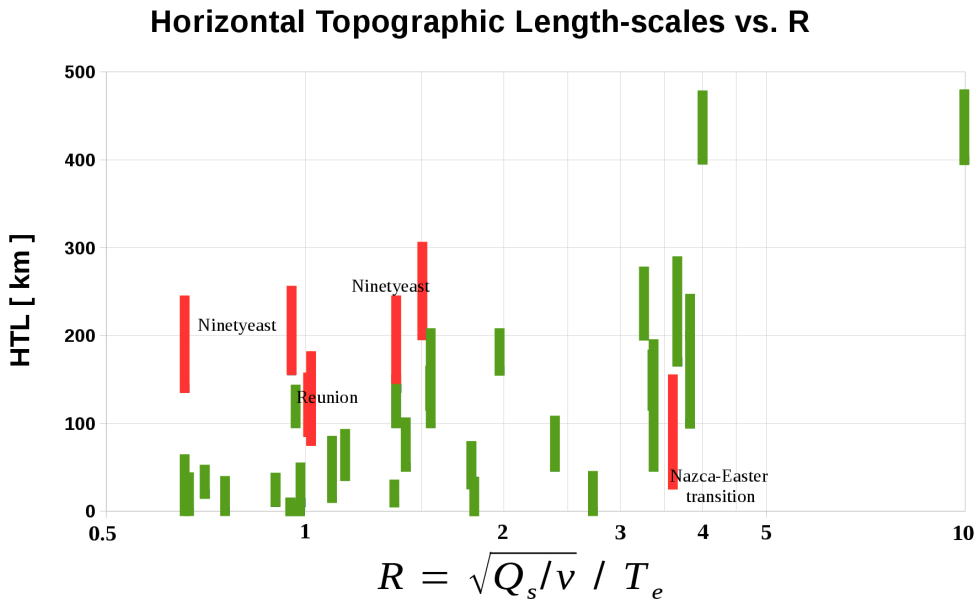

Figure 1.4. Horizontal Topographic Lengthscale HTL [km] versus the dimensionless heat flux ratio *R*. For each computed *R* value, a range in HTL (measured from Google Earth) is presented (Figure 1.2). The overall set of observations (green bars) shows the expected increase of HTL with *R*. Deviating from this trend (red bars) are the Ninetyeast Ridge, and to some extent Reunion and the Nazca-Easter transition region (see text).

1.4 Discussion

The principal observations motivating this study are the conspicuous transitions from smooth to rough topography along the Easter and Tristan hotspot tracks (Figures 1.1a and 1.1b). These transitions are explainable in terms of very young (near-ridge) versus relatively mature (off-ridge) lithospheric emplacement environments. We have attempted to cast these observations into a larger context by examining other hotspot tracks where sufficient constraining data exist, and by developing a scaling parameter R_0 , the ratio of available plume heat to lithospheric heat capacity. This scaling is directly related to the parameter R which largely captures the observed behavior in terms of the controlling variables Q_s, v and T_e. Using the dimensionless parameter R_0 (equation 7) instead of R (equation 8) would simply introduce a factor of ~4.9 in the scaling (a shift in the numerical R values for smooth versus rough topography). Using the estimated thermal lithospheric thickness (perhaps corresponding to the 1250° C isotherm) instead of the estimated elastic thickness T_e (corresponding to the 450°C isotherm) would, likewise, merely scale the R values by a constant factor of ~0.2, and the conversion factor from R to R_0 would become ~1.5. We find T_e preferable, because it can be compared with present-day estimates from gravity and bathymetry analysis.

For the scaling calculations we have performed, there is a transition from rough to smooth topography in the approximate range $1.5 < R < 3$ for most of the hotspot tracks examined, and this transition is generally gradual: (i) At 80 Ma, the Mid-Atlantic Ridge moved away from Tristan plume (*Nurnberg and Muller* [1991]) with a gradual bathymetric transition: the single-branched broad Walvis rise splits into two narrower (~90 km width) branches (Tristan and Gough) with visible individual seamounts. In this region R decreases from ~3.3 to ~2.0 (during 80-60 Ma). (ii) During the period 8 to 1 Ma ago, the Hawaiian plume increased its buoyancy flux by a factor of ~3 (*Wessel* [2016]), while v and T_e did not change substantially. Correspondingly, in topographic expression, the ridge horizontal length-scale increased from ~60 km to ~200 km, accompanied by a notable increase in continuity/connectivity. In this interval, R increases from ~1.2 to ~2.0.

The Ninetyeast Ridge deviates from the global trend (Figure 1.3), exhibiting transitional to smooth morphology at rather low values of R (<1.6). Spreading ridge jumps (perhaps controlled by the plume itself causing zones of weakness), as well as the apparently variable relative motion, v, between the Indian plate and the Kerguelen/Ninetyeast hotspot, cause the LAE values to vary in ways not well-captured by the formulation used here. The lack of robust estimates for the Kerguelen plume buoyancy flux prior to 40 Ma makes the problem more challenging.

Moreover, we note that there is a pervasive N-S trending set of fracture zones parallel to the Ninetyeast hotspot track (*Sreejith and Krishna*, [2013, 2015]), perhaps promoting “upstream” migration of plume material and magma from the mantle plume source through the fractures. This might weaken the lithosphere in advance of the principal large-scale magmatism (that typically occurs only above and downstream of the source), thus facilitating lithospheric deformation and intrusive magmatism, and potentially leading to smoother bathymetry.

The Reunion hotspot system deviates slightly from the expected trend, with transitional morphologies at rather low values of R~1. This may be due to biased estimates of the Reunion plume buoyancy flux owing to the Mahanoro-Wilshaw and Mauritius fracture zones that bound the last ~30 Ma of hotspot track formation (*Torsvik et al.*, [2013]).

Some complexity arises when the moving spreading-centers are in the close vicinity of mantle plumes: a fraction of the plume material may drain toward the spreading center and then diverge due to plate spreading, creating subordinated V-shaped axial tracks in addition to the principal hotspot track, as pointed out by *Sleep* [2002]. These tracks are evident in some cases, but otherwise they tend to be merged with the rest of the bathymetric signals especially on young lithosphere where massive intrusion and magmatism shapes the bathymetry.
Older hotspot-related volcanic edifices formed initially above sea level are subject to erosional flattening, which could skew the evaluation of topographic character to some degree for older hotspot tracks. For example on Walvis Ridge (age>80 Ma) and northern Ninetyeast Ridge (age>70 Ma) the bathymetric character was likely rougher back in time. Nevertheless, present-day near-ridge systems such as Iceland (or to some extent Galápagos) exhibit highly smooth topography. These systems have present-day LAE values>10 Ma, perhaps comparable to the near-ridge Walvis Ridge prior to ~100 Ma.

Although the scaling parameter $R(Q_s, v, T_e)$ is not a perfect predictor of the character of hotspot track topography, or of the balance of intrusive to extrusive magmatism, it does account to first-order for many of the global observations in Figure 1.2 in terms of the expected controlling variables. Some scatter in the results indicates additional complexity, such as lithospheric properties altered by stress and fracturing, or other inherited lithospheric properties not captured simply by plate age and elastic thickness.
The formulation presented here emphasizes the recognition of the main controlling variables of the problem and its understanding from a functional perspective. The present study suggests a useful framework for future modeling studies of the development of hotspot-track topography, especially in regards to the balance of intrusive *versus* extrusive processes during hotspot track emplacement.

1.5 Acknowledgements

The authors thank Sally Gibson, Eduardo Contreras-Reyes, Dennis Geist, Seth Saltiel and Tushar Mittal for helpful suggestions on an earlier version of this manuscript, and Norm Sleep and Shijie Zhong for their constructive reviews.
Consultation of details regarding the data and processes, when further beyond the supporting information, should be directed to the first author at "felipeorellanarovirosa@gmail.com".
This work was supported by CONICYT Chile, the US National Science Foundation and the Esper Larsen Fund at UC Berkeley.

1.6 Supporting Information (published): Details on the calculation of *R* values:

Easter chain: (26.5 - 0) Ma, average Qs=0.84 m^3/s, *Davies* (1988), *Sleep* (1990), *King and Adam* (2014). Te(LAE)~[3.5 , 9.4] km, *Watts* (1978), *Kruse et al.* (1997). Mean v ~ 2450 km / 26.5 Myr = 92.45 km/Ma. More details in references+.
Nazca Ridge: (43 - 26.5) Ma: on-ridge average Qs = 0.42 m^3/s (half the off-ridge value), Te~3.5 km *Cochran* (1979), mean v = 1220 km / 16.5 Ma = 73.9 km/Ma. More details in *Feighner and Richards* (1995), *Sleep* (2002), *Hampel et al.* (2004) and references+.
(+) *Pilger and Handschumacher* (1981), *Couch and Whitsett* (1981), *Wilder* (2003), *Hillier* (2007).

Tristan-Gough: {80,40,0} Ma, average Qs={0.531, 0.332 , 0.39} m^3/s relative values proportional to the ones in Adam (2007). Absolute values: average from references*.
Te(LAE)~{7.5, 11.6, 16.5} km, *Watts* (1978). Mean v ~ 1950 km / 80 Ma = 24.38 km/Ma.
Walvis Ridge: (130-80) Ma, average Qs=0.531 m^3/s value proportional to the one in Adam (2007), absolute value: average from references*. Te~7.5 km (on ridge), *Cochran* (1979).
mean v ~ 1400 km / 50 Ma = 28 km/Ma.
More details in *Goslin and Sibuet* (1975), *Dingle and Simpson* (1977), *Detrick and Watts* (1979), *Kumar* (1979), *Kostoglodov et al.* (1981), *O'Connor and Duncan* (1990), *Nurnberg and Muller* (1991), *Feighner and Richards* (1995), *Sleep* (2002), *Gibson et al.* (2005).
(*) *Davies* (1988), *Sleep* (1990), *Adam et al.* (2007), *O'Connor et al.* (2012), *King and Adam* (2014).

Louisville: (60-0) Ma: Qs=0.698 m^3/s, average from *Davies* (1988), *Sleep* (1990), *Turcotte and Shubert* (2002), *King and Adam* (2014). Te~Te(LAE), *Watts* (1978). (0-25) Ma: v ~ 1600 km / 25 Ma = 64 km/Ma; (25-44) Ma: v ~ 1400 km / 19 Ma = 73.7 km/Ma; (44-75) Ma: v ~ 1350 km / 30 Ma = 45 km/Ma.
More details in *Lonsdale* (1988), *Geli et al.* (1998), *Lyons et al.*(2003), *Hillier* (2007), *Wessel* (2009), *Contreras-Reyes et al.*(2010).

Galápagos: Off-ridge Qs=0.33 m^3/s average from *King and Adam* (2014) and *Sleep* (1990);
Te~Te(LAE); v ~ 37 km/Ma, *Werner et al.* (2003), with average v ~ 600 km/14.5 Ma = 40 km/Ma.
For on-ridge and Cocos-plate-located hotspot period, a 1/3 factor was applied on Qs. There, v for the Carnegie ridge on Nazca plate is given by the half-spreading rate v~30 km/Ma. On-ridge Te~4-5 km (PNSC) *Cochran* (1979), *Feighner and Richards* (1995), *Ribe and Delattre* (1998), *Sleep* (2002).

Iceland: Present-day Qs=0.64 m^3/s average from *King and Adam* (2014) and *Sleep* (1990); speed v < 10 km/Ma (w.r.t. Eurasia); Te(LAE)~16 km. On-ridge period: 0.5xQs; Te~4.5 km, *Cochran* (1979). More details in *Feighner and Richards* (1995), *Phipps Morgan* (1997), *Ribe and Delattre* (1998), *Foulger* (2002), *Bjarnason* (2008), *Mihalffy et al.* (2006), *Torsvik et al.* (2015).

Hawaii: Present-day Qs=3.02 m^3/s, average from *Davies* (1988), *Sleep* (1990), *Turcotte and Shubert* (2002), *King and Adam* (2014). Past values in proportion to estimates by *Wessel* (2016). Te~Te(LAE), *Watts* (1978). (47-25) Ma: v ~ 1380 km / 22 Ma = 62.7 km/Ma; (25-0) Ma: v ~ 2300 km / 25 Ma = 92 km/Ma. More details in *Watts and Ten Brink* (1989), *Ribe and Christensen*(1999), *Watts* (2001), *Hillier* (2007).

Ninetyeast: {77,73,62,55,45} Ma, Qs=0.18 m^3/s, *King and Adam* (2014). Te~Te(LAE) *Watts* (1978) and references. (0-25) Ma: v ~ {100,100,120,120,70} km/Ma relative variation proportional to the full spreading-rate on *Sreejit and Krishna* (2015), absolute values given by *Sreejit and Krishna* (2015, 2013). More details in *Detrick and Watts* (1979), *Royer* (1991), *Mukhopadhyyay and Krishna* (1995), *Frey et al.*(2000), *Krishna et al.* (2001), *Coffin et al.* (2002), *Duncan* (2002).

St. Helena: Present-day Qs=0.13 m^3/s, average from *Davies* (1988), *Sleep* (1990), *Turcotte and Shubert* (2002), *Adam* (2007), *King and Adam* (2014). Past values in proportion to estimates by *Adam* (2007). Te~Te(LAE), *Watts* (1978). (50-20)Ma: v ~ 650 km / (50-20) Ma = 21.67 km/Ma, (20-0)Ma: v ~ 420 km/ (20-0) Ma = 21 km/Ma. More details in *Kostoglodov et al.*(1981), *Nurnberg and Muller* (1991).

Reunion: Present-day Qs=0.465 m^3/s, average from *Davies* (1988), *Sleep* (1990), *Turcotte and Shubert* (2002), *King and Adam* (2014). A factor 0.5x for on-ridge value. Off-ridge Te~Te(LAE), *Watts* (1978); on-ridge Te~4 km given by references. (50-30)Ma: v ~ 670 km / (50-30)Ma = 33.5 km/Ma, (30-10)Ma: v ~ 540 km / (30-10) Ma = 27 km/Ma, (20-0)Ma: v ~ 370 km / (20-0)Ma = 18.5 km/Ma. More details in *Phipps Morgan* (1997), *Tiwari et al.* (2007), *Torsvik et al.* (2013).

For present-day ages of the systems, the elastic thickness 'T_e' was complemented with the values available from gravimetry analysis on those references.
Google Earth software and plugin 'Age of the Lithosphere for Google Earth' were used in measurements of distance and ages, complementing the available values from literature.

1.7 Additional (unpublished) figures for the chapter

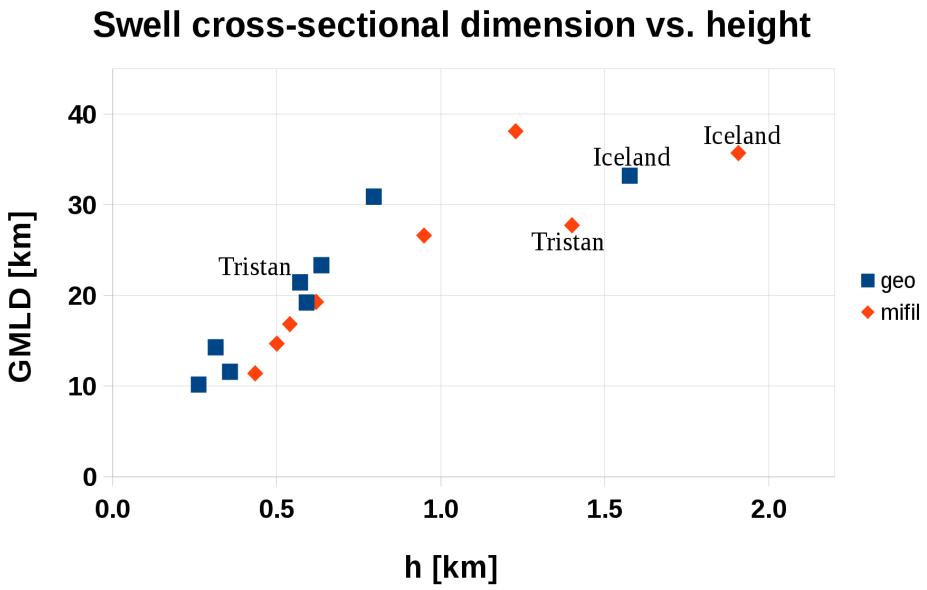

Additional Figure 1.A1: Geometric Mean Linear Dimension (GMLD) vs. Hotspot Swell Average Height (h) for all the systems of this study (except Ninetyeast Ridge), using the two geometrical assessments of *King and Adams* [2014]. Note that GMLD = $(Q_s / v)^{1/2} = (L \cdot h)^{1/2}$. Discarding Iceland and the MiFil-area assessment of Tristan, the GMLD is nearly proportional with the swell dimension h. Thus $L \sim h$, which implies that the aspect ratio is approximately constant over the scales.

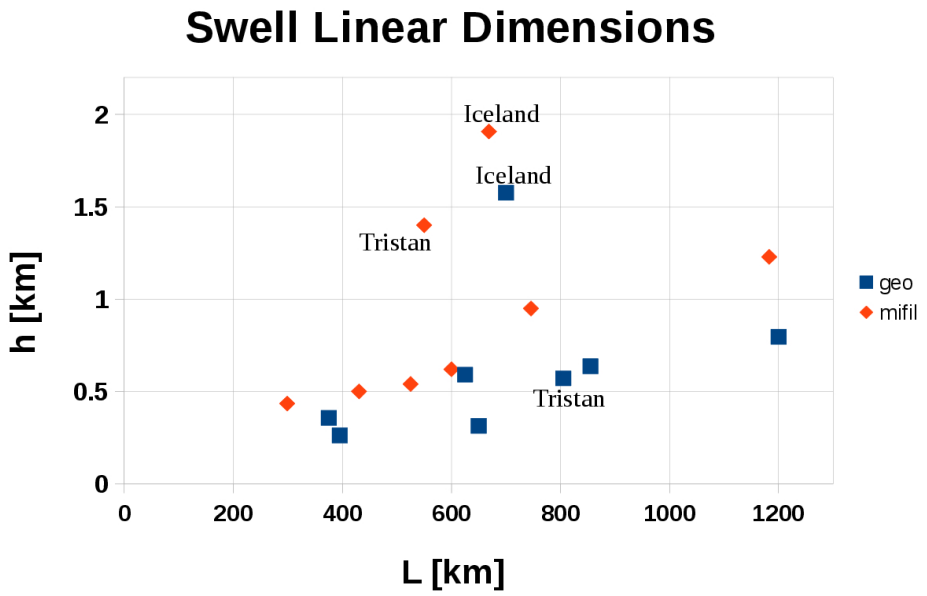

Additional Figure 1.A2: Hotspot Swell Average Height (h) vs. Transverse Width (L) for all the systems of this study (except Ninetyeast Ridge), using the two geometrical assessments of *King and Adams* [2014]. Discarding Iceland and the MiFil-area assessment of Tristan, the swell dimensions are to good degree mutually proportional, or $L \sim h$, which implies that the aspect ratio is approximately constant across the scales.

1.8 References

Adam, C., V. Vidal, and J. Escartín (2007); 80-Myr history of buoyancy and volcanic fluxes along the trails of the Walvis and St. Helena hotspots (S. Atlantic), *Earth Planet. Sc. Lett.*, 261 (3), 432-442.

Bjarnason, I. P. (2008), An Iceland hotspot saga, JÖKULL No. 58, 3-16.

Calmant, S., J. Francheteau and A. Cazenave (1990), Elastic layer thickening with age of the oceanic lithosphere: a tool for prediction of the age of volcanoes or oceanic crust, *Geophys. J. Int.*, 100, 59-67.

Cochran, J. R. (1979), An Analysis of Isostasy in the World's Oceans 2. Midocean Ridge Crests, *J. Geophys. Res.*, 84, nB9, 4713-4729.

Coffin M.,F., M. S. Pringle, R. Duncan, T.P. Gladczenko, (2002), M. Storey, R.D. Muller, L.A. Gahagan (2002), Kerguelen Hotspot Magma Output since 130 Ma, *J. Petrology*, 43,1121–1139.

Contreras-Reyes, E., I. Grevemeyer, A.B. Watts, L. Planert, E.R. Flueh, and C. Peirce (2010), Crustal intrusion beneath the Louisville hotspot track, Earth Planet. Sci. Lett. , (289), 323–333, doi:10.1016/j.epsl.2009.11.020.

Couch, R., and R. Whitsett (1981), Structures of the Nazca ridge and the continental shelf and slope of southern Peru, *Geological Soc. America*, memoir 154.

Davies, G. (1988), Ocean bathymetry and mantle convection: 1. Large-scale flow and hotspots, *J. Geophys. Res*., 93, B9,10,467-10,480, DOI: 10.1029/JB093iB09p10467

Detrick, R.S., and A.B. Watts (1979), An analysis of isostasy in the world's oceans, 3. Aseismic ridges; *J. Geophys. Res*, 84, n B7, 3637-3653.

Dingle, R.V., and E. Simpson (1977), The Walvis ridge: a review, Special publications, Geodynamics: Progress and Prospects, v5.

Duncan, R. (2002), A time frame for Construction of the Kerguelen plateau and Broken ridge, *J. Petrology*, 43, n7, 1109-1119.

Farnetani, C., M.A. Richards and M. Ghiorso (1996), Petrological models of magma evolution and deep crustal structure beneath hotspots and flood basalt provinces, *Earth Planet. Sc. Lett.*, 143, 81-94.

Feighner, M., and M.A. Richards (1994), Lithospheric structure and compensation mechanisms of the Galápagos Archipelago, *J. Geophys. Res.*, 99, 6711-6729.

Feighner, M., and M.A. Richards (1995), The fluid dynamics of plume-ridge and plume-plate interactions: an experimental investigation, *Earth Planet. Sc. Lett.*, 129, n 1-4, 171-182.

Foulger, G. (2002), Plumes, or plate tectonic processes?, https://community.dur.ac.uk/g.r.foulger/Offprints/Astron-Geo.pdf.

Frey F. et al. (2000), Origin and evolution of a submarine large igneous province: the Kerguelen Plateau and Broken Ridge, southern Indian Ocean, *Earth Planet. Sc. Lett.*, 176, 73-89.

Geli L., D. Aslanian, JL. Olivet, I. Vlastelic, L. Dosso, H. Guillou, H. Bougault (1998), Location of Louisville hotspot and origin of Hollister Ridge: geophysical constraints, *Earth and Planet. Sc. Lett.*, 194, 31-40.

Gibson, S., R.N. Thompson, J.A. Day, S.E. Humphris, A.P. Dickin (2005), Melt-generation processes associated with the Tristan mantle plume: constraints on the origin of EM-1, *Earth Planet. Sc. Lett.* 237, 744 – 767.

Goslin, J., J. Sibuet (1975), Geophysical study of the easternmost Walvis Ridge, South Atlantic: Deep structure, *Geological Soc. America Bull.*, 86, 1713-1724.

Hampel, A., N. Kukowski, J. Bialas, C. Huebscher and R. Heinbockel (2004), Ridge subduction at an erosive margin: The collision zone of the Nazca Ridge in southern Peru, *J. Geophys. Res.*, 109, B02101, doi:10.1029/2003JB002593.

Hieronymus, F., D. Bercovici (2001), A theoretical model of hotspot volcanism: Control on volcanic spacing and patterns via magma dynamics and lithospheric stresses, *J. Geophys. Res.*, 106, n. B1, 683-702.

Hillier, J.K. (2007), Pacific seamount volcanism in space and time, *Geophys. J. Int.*, 168, 877–889.

King, S. D., and C. Adam (2014) Hotspot Swells Revisted, *Phys. Earth Planet. Int.*, 235, 66-83, DOI: 10.1016/j.pepi.2014.07.006.

Kostoglodov, V., M.G. Kogan and E. Magnitskaya (1981), Isostasy of the Southern Mid-Atlantic Ridge'

Long-Wavelength and Short-Wavelength Effects, *J. Geophys. Res.*, 86, B9, 7825-7841.

Krishna K., Y. P. Neprochnov, D. Gopala Rao, and B. N. Grinko (2001), Crustal structure and tectonics of the Ninetyeast Ridge from seismic and gravity studies, *Tectonics*, 20, n. 3, 416-433.

Kruse, S., J. Zhengrong, D. Naar, and R. Duncan (1997), Effective elastic thickness of the lithosphere along the Easter Seamount Chain, *J. Geophys. Res.*, 102, n. B12, 27,305-27,317.

Kumar, N. (1979), Origin pf paired aseismic rises Ceara and Sierra Leone rises in the equatorial, and the RioGrande rise and Walvis ridge in the south Atlantic, *Marine Geology*, 30 (1979), 175-191.

Lonsdale, P. (1988), Geography and History of the Louisville Hotspot Chain in the Southwest Pacific, *J. Geophys. Res.*, 93, n. B4, 3078-3104.

Lyons, S., D. Sandwell and W. Smith (2000), Three-dimensional estimation of elastic thickness under the Louisville Ridge, *J. Geophys. Res.*, 105, B6, 13.239-13,252.

Mihalffy, P., B. Steinberger and H. Schmeling (2008), The effect of the large-scale mantle flow field on the Iceland hotspot track, *Tectonophysics*, 447, 5-18.

Mukhopadhyyay, M. and M. Krishna (1995), Gravity Anomalies and Deep Structure of the Ninetyeast Ridge North of the Equator, Eastern Indian Ocean - A Hot Spot Trace Model,Marine Geophysical Researchers, 17, 201-216.

Nurnberg, D., and D. Muller (1991), The tectonic evolution of the South Atlantic from Late Jurassic to present, *Tectonophysics*, 191, 21-53.

O'Connor, J. and R. Duncan (1990), Evolution of the Walvis Ridge-Rio Grande Rise Hot Spot System: Implications for African and South American Plate Motions Over Plumes, *J. Geophys. Res*., 95, n BI1, 17,475-17,502.

O'Connor, J., W. Jokat, A. P. Le Roex, C. Class, J. R. Wijbrans, S. Keßling, K. F. Kuiper, and O. Nebel (2012), Hotspot trails in the South Atlantic controlled by plume and plate tectonic processes, *Nature Geoscience*, 5, 735-738, DOI: 10.1038/NGEO1583.

Orellana-Rovirosa, F., and M.A. Richards (2015), Evidence and models for lower crustal flow beneath the Galápagos platform, Geochem. Geophys. Geosyst., 16, doi:10.1002/2015GC006136.

Phipps Morgan, J. (1997), The generation of a compositional lithosphere by mid-ocean ridge melting and its effect on subsequent off-axis hotspot upwelling and melting, *Earth Planet. Sc. Lett.*, 146, 213-232.

Pilger, R., and D. Handshumacher (1981), The fixed-hotspot hypothesis and origin of the Easter-Sala y Gomez-Nazca trace, *Geological Soc. America Bull.*, Part I, 92, 437–446.

Ribe, N.M., and W. L. Delattre (1998), The dynamics of plume-ridge interaction III. The effects of ridge migration, *Geophys. J. Int.*, 133, 511-518.

Ribe. N.M. and U.R. Christensen (1999), The dynamical origin of the Hawaiian volcanism, *Earth Planet. Sc. Lett.*, 171, 517-531.

Richards, M., E. Contreras-Reyes, C. Lithgow-Bertelloni, M. Ghiorso, and L. Stixrude (2013), Petrological interpretation of deep crustal intrusive bodies beneath oceanic hotspot provinces: *Geochem. Geophys. Geosys.*, 14, n3, 604–619.

Royer, J.-Y., J. W. Peirce, and J. K. Weissel (1991), Tectonic constraints on the hot-spot formation of Ninetyeast Ridge, in Proc. ODP Sci. Results, edited by J. K. Weissel, et al., 121, 763–776, Ocean Drilling Program, College Station, TX.

Sleep, N. (1990), Hotspots and Mantle Plumes' Some Phenomenology, J. Geophys. Res., 95, n. B5, 6715-6736.

Sleep, N. (1996), Lateral flow of hot plume material ponded at sublithospheric depths, *J. Geophys. Res*., 101, n. B12, 28,065-28,083.

Sleep, N. (2002), Ridge-crossing mantle plumes and gaps in tracks, *Geochem. Geophys. Geosyst.*, 3(12), 8505.

Sreejith, K.M. and K. S. Krishna (2013), Spatial variations in isostatic compensation mechanisms of the Ninetyeast Ridge and their tectonic significance, *J. Geophys. Res*., 118, 5165–5184, doi:10.1002/jgrb.50383.

Sreejith, K. M., and K. S. Krishna (2015), Magma production rate along the Ninetyeast Ridge and its relationship to Indian plate motion and Kerguelen hot spot activity, *Geophys. Res. Lett.*, 42, 1105–1112.

Tiwari, V.M., I. Grevemeyer, B. Singh and J. Phipps Morgan (2007), Variation of effective elastic thickness and melt production along the Deccan–Reunion hotspot track, *Earth Planet. Sc. Lett.*, 264, 9 – 21.

Torsvik, T., H. Amundsen, R. Trønnes, P. Doubrovine, C. Gaina, N. Kusznir, B. Steinberger, F. Corfu, L. Ashwal, W. Griffin, S.Werner, and B. Jamtveit (2015), Continental crust beneath southeast Iceland:
http://www.pnas.org/lookup/suppl/doi:10.1073/pnas.1423099112/-/DCSupplemental

Torsvik, T., H. Amundsen, E. Hartz, F. Corfu, N. Kusznir, C. Gaina, P. Doubrovine, B. Steinberger, L. Ashwal and B. Jamtveit (2013), A Precambrian microcontinent in the Indian Ocean, *Nature Geoscience*, 6, 223–227, doi:10.1038/ngeo1736.

Turcotte, D., and G. Shubert (2002), *Geodynamics*, second edition, Cambridge University Press, NY.

Watts, A.B. (1978), An analysis of isostasy on the world's oceans, 1, Hawaiian-Emperor seamount chain, *J. Geophys. R.*, 83, 5989-6004.

Watts, A.B. and U.S. Ten Brink (1989), Crustal Structure, Flexure, and Subsidence History of the Hawaiian Islands, *J. Geophys. Res*., 94, n B8, 10,473-10,500.

Watts, A.B., (2001). Isostasy and flexure of the lithosphere. Cambridge Univ. Press, Cambridge.

Werner, R., K. Hoernle, U. Barckhause, and F. Hauff (2003), Geodynamic evolution of the Galápagos hotspot system (Central East Pacific) over the past 20 m.y.: Constraints from morphology, geochemistry, and magnetic anomalies, *Geochem. Geophys. Geosys.*, v.4, 12, 1108.

Wessel, P. and L.W. Kroenke (2009), Observations of geometry and ages constrain relative motion of Hawaii and Louisville plumes, Earth and Plan. Sc. Lett., 284, 467–472.

Wessel, P. (2016), Regional–residual separation of bathymetry and revised estimates of Hawaii plume flux, *Geophys. J. Int.*, 204, 932–947 , doi: 10.1093/gji/ggv472.

Wilder, D. (2003), Relative motion history of the Pacific-Nazca (Farallon) plates since 30 Ma ago, M.S. Thesis, College of Marine Science, University of Florida, Florida, USA.

Software:

Google Earth software (version 7.1.8.3036), plus special plugin 'Age of the Lithosphere for Google Earth', http://nachon.free.fr/GE/Welcome.html

Data:

Global Satellite-derived Bathymetry and Gravity Anomaly http://topex.ucsd.edu/cgi-bin/get_data.cgi ; http://topex.ucsd.edu/grav_outreach/.

Chapter 2

Evidence and models for lower crustal flow beneath the Galápagos platform

by

Felipe Orellana Rovirosa and Mark Richards

Chapter Abstract

The volcanic Galápagos Islands are constructed upon a broad platform, with their active westernmost islands marking the current position of the hotspot. Built upon young oceanic lithosphere (<15 Ma), this platform exhibits unique morphologic features including a system of stepped terraces on the southwestern escarpment with 3 km-relief, contrasting with gentle slopes off the eastern platform toward the Carnegie Ridge. Considering horizontal lithostatic pressure differences associated with this relief, along with high temperatures within the young, hotspot-affected lithosphere, it is likely that lower crustal flow contributes significantly to crustal deformation within the Galápagos platform. Using a 2D, isostatic, thin-sheet approximation for the Stokes flow equation with (Newtonian) space-time dependent viscosity, we suggest that the bathymetric rim along the eastern platform region (where gravimetry indicates Airy isostasy) near Española Island may be the expression of a mature lower crustal flow front developed over the last ~3 Myr; horizontal mass displacements (~50 km) associated with this crustal flow episode may have advected mantle plume geochemical signatures towards the southeast, and in directions not necessarily parallel to the hotspot track. Also, the stepped terraces along the southwestern platform may be explained by lower crustal flow-associated backward tilting of the bathymetric surface that, although resulting in small angular changes (~0.1 deg), effectively hinders the horizontal flow of lava sheets. This backward-tilting process was likely restricted to the last ~1 Ma or less, and may be a unique event involving extrusion of lavas from within the southwestward-marching lower-crustal flow front.

Orellana-Rovirosa, F., and M. Richards (2015), Evidence and models for lower crustal flow beneath the Galápagos platform, *Geochem. Geophys. Geosyst.*, 16, doi:10.1002/2015GC006136.

2.1. Introduction

The Galápagos Islands exhibit many unusual characteristics relative to other ocean-island provinces, features made famous of course by Darwin's extraordinary geological and biological discoveries there in the 19th Century. From the physiographic and geologic standpoint, this island archipelago and the surrounding seafloor display features that remain largely unexplained to this day, including the early-noticed "Darwinian trends" of structural and volcano alignment, the occurrence of volcanism across a broad elevated platform, the diversity of lava and volcano types, and the complicated spatial and temporal patterns of geochemical signatures that must reflect the interaction between the Galápagos hotspot (mantle plume) and the adjacent Galápagos Spreading Center (GSC), located just to the north of the Galápagos archipelago (illustration on Figure 2.1a). The thickened crust of the paired Cocos and Carnegie Ridge systems has resulted from the location of the Galápagos hotspot approximately beneath the GSC for the past ~20 million years [*Werner et al.*, 2003].

An unusual characteristic of the Galápagos Archipelago is the broad distribution of volcanism, which extends well outside of the present mantle plume location beneath the lithosphere [*Villagomez et al.*, 2014]. Another related aspect is the somewhat non-time-transgressive eruptive history along the E-W direction of Nazca plate motion relative to the hotspot reference frame [*Geist et al.*, 1988]. The plume is currently located beneath the large, active shield volcanoes that have formed Fernandina and Isabela Islands (Figure 2.1b), yet there has also been recent volcanism on some of the easternmost islands such as San Cristobal, as well as older eruptions in the central platform, e.g., Santa Fe Island [*Geist et al.*, 1988]. Adding to this complicated scenario is that the trace element and isotopic signatures of the Galápagos volcanoes do not fit the expected pattern – although the plume signature along the GSC becomes stronger as the Galápagos hotspot is approached from both east and west [*Detrick et al.*, 2002; *Christie et al.*, 2005], the most depleted island and seamount signatures are found in the center of the archipelago, while the most hotspot-like (enriched) signatures are found around the margins of the platform [*Geist et al.*, 1988; *Hoernle et al.*, 2000]. This pattern may result from thermal entrainment effects within the plume [*Richards and Griffiths*, 1989], inherent heterogeneous "streaks" within the plume [*Farnetani and Hofmann*, 2012], lithospheric thickness variations [*Gibson and Geist*, 2010], or perhaps unknown aspects of plume-ridge interaction [*Feighner and Richards*, 1995; *Ito et al.*, 1997; *Ito and Bianco*, 2014; *Gibson et al.*, 2015].

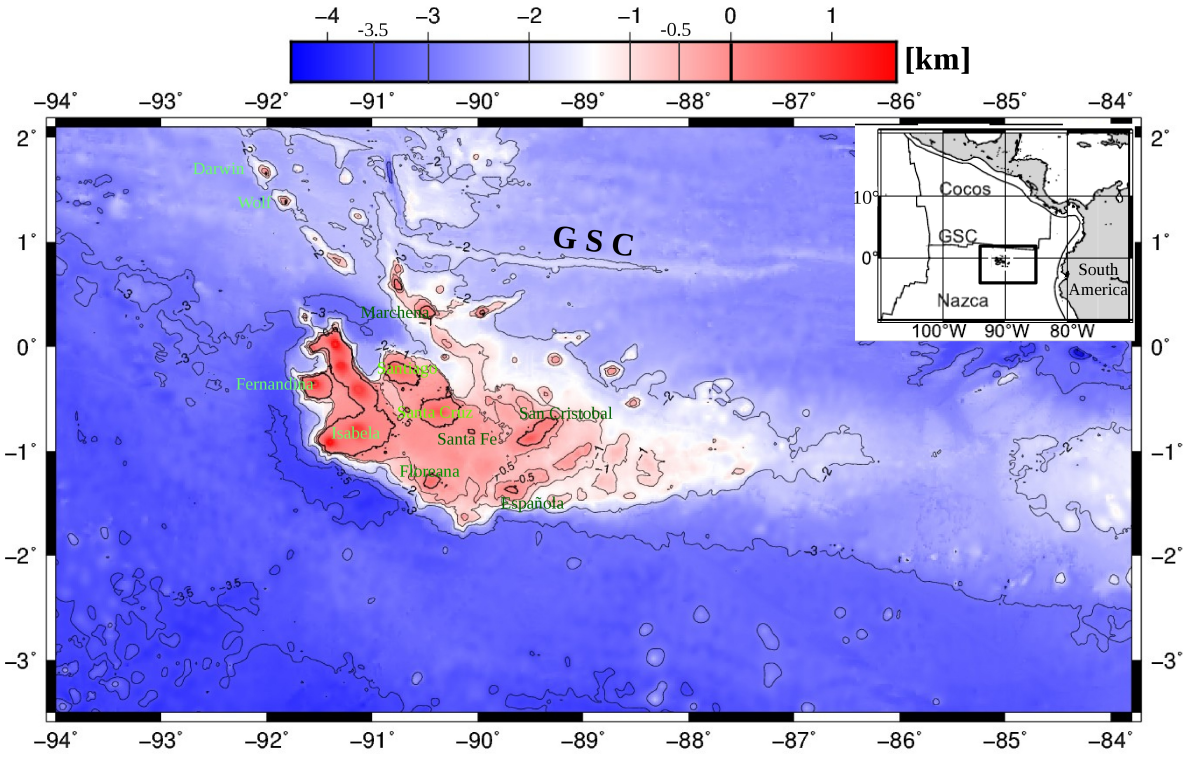

Figure 2.1a. Geographic context and bathymetry of the Galápagos archipelago. The Galápagos islands span equatorial latitudes, and are the sub-aerial expression of a broad and thick volcanic platform constructed on young (<15 Myr) crust and lithosphere. The Galápagos hotspot is located under the westernmost area of the archipelago, where there is also a higher concentration of active volcanic centers.

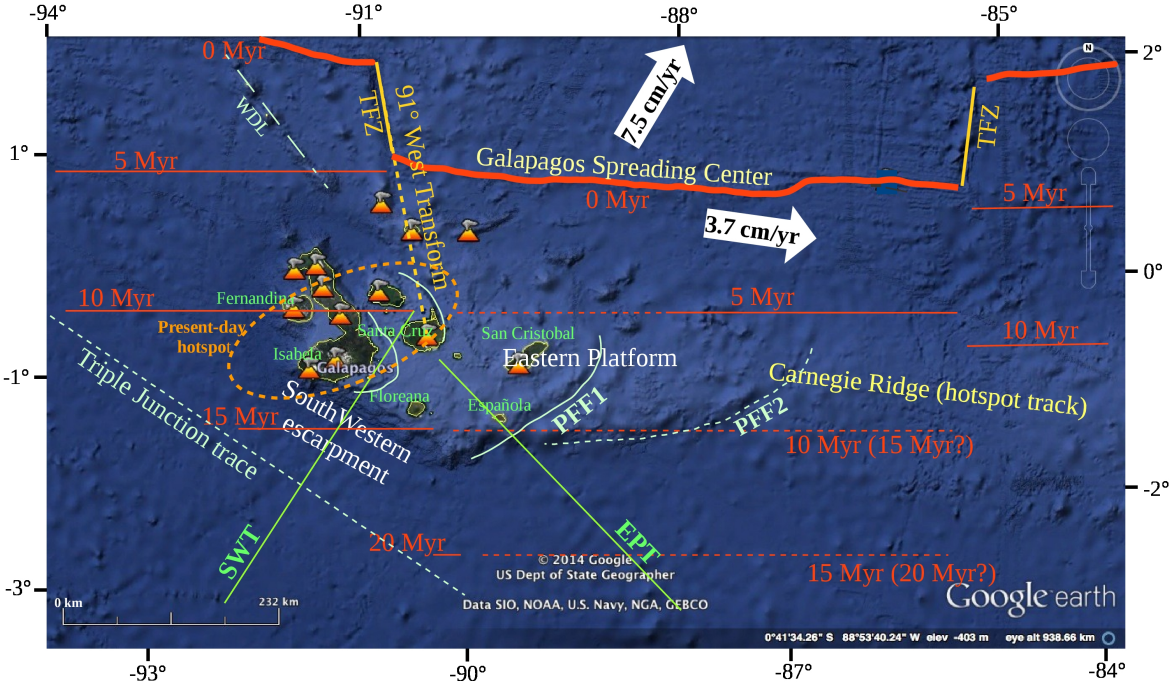

Figure 2.1b. Geologic setting of the Galápagos: Young crust is created at the GSC (reference isochrons in red), and is offset by the right-lateral 91°W transform fault zone (TFZ), creating a ~5 Myr age discontinuity mainly in the northern Galápagos [*Mittelstaedt et al.*, 2012]. The active volcanoes are the surface expression of extensive hotspot-associated magmatism, processes that have constructed the crustal platform and thermally reset the lithospheric age. The orange dashed ellipse marks the inferred present-day location of the hotspot [*Villagomez et al.* 2014]. Thick white arrows show the plates' velocities with respect to the deep-hotspot reference frame [*Werner et al.*, 2003; *Cuffaro and Doglioni*, 2007; *Morgan and Morgan*, 2007]. On the eastern platform region, remarkable bathymetric features with elongated rim morphology are the surface expression of Proposed (lower crustal) Flow Fronts (PFF1 and PFF2). Green straight lines are the modeled transects: (SWT) South-Western transect and (EPT) Eastern platform transect. WDL is the Wolf-Darwin lineament.

These fascinating features and many others, have been intensively studied since Darwin's early explorations, with most of the emphasis being on the volcanology and geochemistry of the islands, and more recently of the surrounding seamounts [*White et al.*, 1993; *Harpp and White*, 2001], as well as the tectonic evolution of the region [*Hey et al.*, 1972; *Hey and Vogt*, 1977]. Figure 2.2 illustrates the recent evolution of the Galápagos Archipelago in stages, starting approximately 3 million years ago, during which most of the present-day platform and volcanic islands have developed [*Geist et al.*, 2008]. The sequence of events illustrated in Figure 2.2 suggests a question that seems to have hardly been addressed in previous studies of the Galápagos system: To what extent has the broad, relatively flat Galápagos platform, much of it lying within just several hundred meters of sea level, formed as the result of volcanic (extrusive) construction that can be associated with the main island-forming volcanoes and surrounding seamounts, and to what extent has it formed by intrusion of plume-derived magma into the lower crust with subsequent horizontal (gravity-current) flow of this material? In this paper we explore the possibility that after crustal intrusion, horizontal spreading may exercise a first-order control on the construction of the modern Galápagos platform (last ~6 Ma), as well in relation with the analogous Cocos and Carnegie Ridges dating back to 20 Ma.

A number of lines of evidence suggest that lower crustal flow is important in the formation and evolution of the Galápagos platform. First, the breadth and flatness of the platform itself is otherwise difficult to explain solely in terms of volcanic processes. Indeed, the situation may be somewhat analogous to the on-ridge Iceland hotspot, where lower crustal intrusion and horizontal flow are thought to play major roles in shaping the Iceland Plateau as a whole [*Jones and Maclennan*, 2005]. Second, the morphology and underlying seismic structure of the Cocos and Carnegie Ridges suggest that most of the thickened crust found there is intruded gabbro plus perhaps other more mafic rock [*Hooft et al.*, 2010; *Villagomez et al.*, 2011], with some evidence that lower crustal flow along the Carnegie Ridge at about 1° 10' S latitude likely continued after and extended southward beneath surface volcanic construction along the ridge [*Richards et al.*, 2013; see also *Sallares et al.*, 2003, 2005].

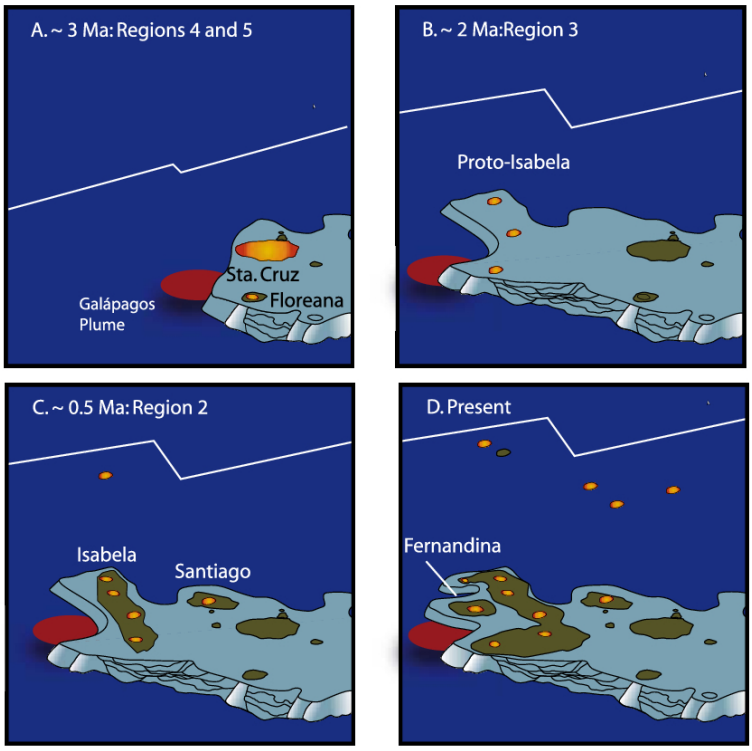

Figure 2.2. Evolutionary model for the Galápagos archipelago (after *Geist et al*. [2008]). Growth of the archipelago has been affected by the northward migration of the GSC. The archipelago alternates between phases where sub-aerial volcanoes grow on top of a stacked -terrace platform at the leading edge of the hotspot (e.g., ~3 Ma and 0.5 Ma to present) and other phases where only the terraces form (e.g., ~2 Ma). The estimated ages of the volcanoes are conjectural. The 'Regions' are defined by *Geist et al*. [2008].

A third line of evidence, and a major focus of this paper, comes from some of the more recently formed structural features of the modern Galápagos platform. The Great Southwest Escarpment (GSE) is one of the most enigmatic, unexplained features found at any hotspot province on Earth (Figure 2.3). Running along the SW margin of the present platform, the seafloor here drops about 3 km to abyssal depths over a horizontal distance of only about 30 km, or an average slope of about 10% (or 5.7 degrees). It does not appear that this escarpment is caused by a master normal fault [*Feighner and Richards*, 1994], but rather that it is made up of huge, back-stepping or terraced lava flows accumulated in a systematic way [*Geist et al.*, 2008]. In this paper we suggest that the GSE may be explained by a lower crustal flow front capped by lava flows which in turn may originate in neighboring platform volcanoes as well as local breakouts in the flow front itself as it moves southwestward.

Lavas erupting on the platform surface and near the escarpment flow over the subhorizontal portions defined by this surface, which is itself made up of older basaltic lava flows that, under normal conditions, would exhibit slope-angles of less than 1 degree [*Stephen Self*, 2014, personal communication*; Deschamps et al.*, 2014; *Umino*, 2012]. Any process altering these surface slope-angles is likely to alter the style (dynamics) of future lava flows, as the driving force is the down-slope gravity component with lava viscous braking controlled by cooling.

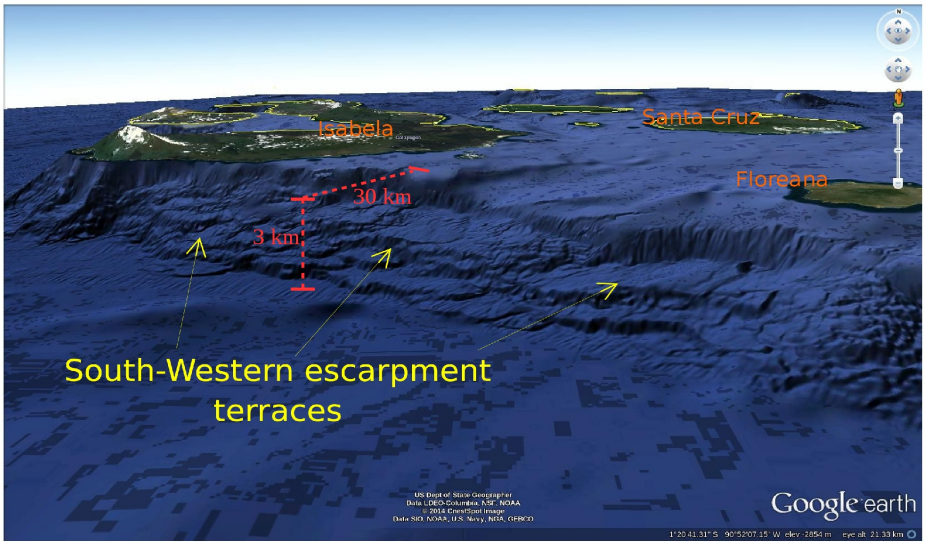

Figure 2.3. Oblique view of the Southwestern escarpment of the Galápagos volcanic platform. The unique system of stepped terraces was formed by basaltic lava flows. A vertical exaggeration factor of 3 has been applied.

We hypothesize that southwestward-directed regional mass transport in the deep crustal regions, occurring on time scales of order ~10^5 yrs., is likely to tilt the (local) bathymetric surface of the platform rendering it more horizontal in time, and thus producing an exceptional environment for lava flows that is less favorable for long distance travel. In this way, new lava flows will likely travel shorter distances, creating a receded, backward-stepping set of terraces. Finally for this area, we will discuss and show that the possibility of additional geomorphic shaping mechanisms, like the ones given by paleo-sealevels effects, is unlikely.

Figure 2.1a indicates several other elongated bathymetric escarpments bounding the platform toward the east that, although less dramatic than the GSE, we suggest may also have been shaped by regional deformation of the lower crust. Unfortunately, no high resolution bathymetric imaging has been done on these latter features, and so it is presently difficult to know to what extent they may be analogous to the present-day GSE. However, it is reasonable to suppose that the processes occurring at present along the GSE may be similar to the processes that formed the bounding escarpments along the southern slopes of the Carnegie Ridge and the northern slopes of the Cocos Ridge (with some subsequent geomorphic reshaping).

In this way, a fourth line of evidence and also a major focus of this work, is the observation that in the eastern regions of the Galápagos archipelago, the platform decreases in elevation with a striking morphology: a pronounced, gently curved bathymetric escarpment or rim that extends over approximately 180 km, east from Española and San Cristobal islands and representing the platform natural boundary to the east (PFF1 in Figure 2.1b, where "PFF" refers to "proposed flow front"). This rim-like bathymetric feature, with roughly 1.5 km of platform relief and showing remarkable horizontal continuity, does not seem to be created purely by volcanic construction and regional crustal intrusion. Following several lines of argument, we suggest that this bathymetric feature may have been influenced by lower crustal flow occurring on a hotspot-

affected weak crust, and that after roughly ~3 Myr of evolution it may now be in a mature dynamical stage, probably evolving very slowly or perhaps even "frozen". For this area, we will additionally discuss how paleo-sealevel effects might have played a role in geomorphic shaping, specifically in the upper parts of this escarpment.

East of the PPF1 escarpment, elevations decrease smoothly while otherwise showing mainly one gentle rim (PFF2 in Figure 2.1b) that also exhibits remarkable continuity, until it finally merges into the Carnegie ridge, the distinctive and broad bathymetric high that smoothly extends toward the Nazca-South America subduction zone, and which is believed to be part of the Galápagos hotspot track [*Richards et al.*, 1989, *Werner et al.*, 2003] in response to the relative Nazca plate velocity.

Lastly, the phenomena of lower crustal intrusion (inflation by feeding) and lower crustal flow (relaxation) appear ubiquitous in ocean island settings from both the theoretical standpoint and from numerous high-quality seismic refraction studies along other hotspot tracks [*Richards et al.*, 2013]. Furthermore, at least several hotspot tracks formed either at spreading ridges or on very young oceanic lithosphere (e.g., the Ninety-east Ridge between latitudes 5°N and 27° S on the Indian plate, and the Nazca Ridge offshore of Peru on the Nazca plate) appear to be remarkably smooth, that is, lacking in major volcanic edifices, suggesting most of the volume of excess crust is emplaced by lower crustal intrusion and flow. We hypothesize that in many of these ocean island systems (Galápagos, Iceland, Ninety-east, Nazca, Easter Island, and likely others) the dominant form of crustal thickening and aseismic ridge construction is likely intrusion and lower crustal gravity flow while the mantle plume is located at or near a spreading ridge on young oceanic lithosphere.

Here we develop models for lower crustal flow beneath the Galápagos platform in order to address these observations, and in order to suggest further tests of the lower crustal flow hypothesis. A particular focus is the possibility that the unusual back-stepping lava terraces along the GSE may be shoaled due to backward-tilting as a lower crustal flow front progresses southwestward from the center of the active platform. If such flow is indeed occurring beneath the Galápagos, it may help explain why the platform is so broad, and why it is bordered by conspicuous escarpments. The lateral spread of intrusive magmas may also be related to the curious patterns of geochemical signatures noted above [*Harpp and White*, 2001; *Hoernle et al.*, 2000], as well as the long-noted extraordinary variety of volcanic products and forms occurring on the islands [*Christie et al.*, 1992].

2.2. Methods

Our modeling approach follows from the work of *Jones and Maclennan* [2005], who described the crust beneath the Iceland Plateau as a Stokes fluid with variable viscosity. In turn, their study follows from the work of *Huppert* [1982] and *McKenzie et al.* [2000]. Our approach goes beyond that of *Jones and Maclennan* [2005] in several ways that allow better application to the Galápagos. A complete mathematical description is found in Appendix A, notes on the numerical implementation are in Appendix B, and benchmarking and sensitivity analyses are given in Appendix C.

2.2.1 Physical Formulation

We model lower crustal flow in two Cartesian dimensions, so that 3-D out-of-plane flow is not included. This simplifies the analysis and computation, and is justified because both of the suggested "flow front" morphologies we focus upon are linear features. Figure 2.1b shows the two transects: a Southwestern platform transect (SWT) and an Eastern platform transect (EPT). The crust and mantle are assumed to be in isostatic equilibrium, i.e., vertical movements are rapid compared to horizontal flow response times. Mass transport is computed using a 2D thin-sheet approximation of the Stokes equation, where the crust is described as an incompressible Newtonian fluid whose viscosity varies in time and space. In the thin-sheet approximation, the system is, at all times, of horizontally-extended geometry, and all variables are assumed to have much longer characteristic length scales in x than in z, so that

$$v_x \gg v_z \quad \text{and} \quad \frac{\partial()}{\partial x} \ll \frac{\partial()}{\partial z} \qquad \text{(1 and 2)}$$

where the velocities v_x , v_z are with respect to a reference frame attached to the moving Nazca plate.

2.2.1.1 Boundary Conditions

The following boundary conditions are applied in our models (illustration in Figure 2.4):

1. We impose zero mass flux across the vertical boundaries at both ends of the model box. Zero horizontal velocity on the platform highland lateral boundary (located over central platform points), taken as x=0 at the left model box boundary, is justified by the fact that the central platform is spreading (by deformation) in opposite directions, thus horizontal velocities are presumably small in the central area. The zero horizontal velocity on the distal boundary (at x=L, where L is the transect length) recognizes that normal (background) oceanic crust located far away from the platform and the volcanic centers is not affected by lower crustal flow within the platform.

2. Horizontal velocities are zero on the lower boundary (Moho), assuming that upper mantle rocks have higher creep strength than crustal rocks [*McKenzie et al.*, 2000]. This is not an entirely satisfactory assumption within the central platform, where plume-derived magmas are heating both the mantle and crust. Vertical motion at the Moho is determined by isostasy.

3. We impose zero horizontal velocity at the upper boundary (bathymetry), where the cold uppermost crust behaves rigidly with respect to the softer lower crust below. We do not consider brittle failure of the upper crust, although such behavior could be used post-facto to infer stress patterns. Vertical motion here is found by solving the governing equations.

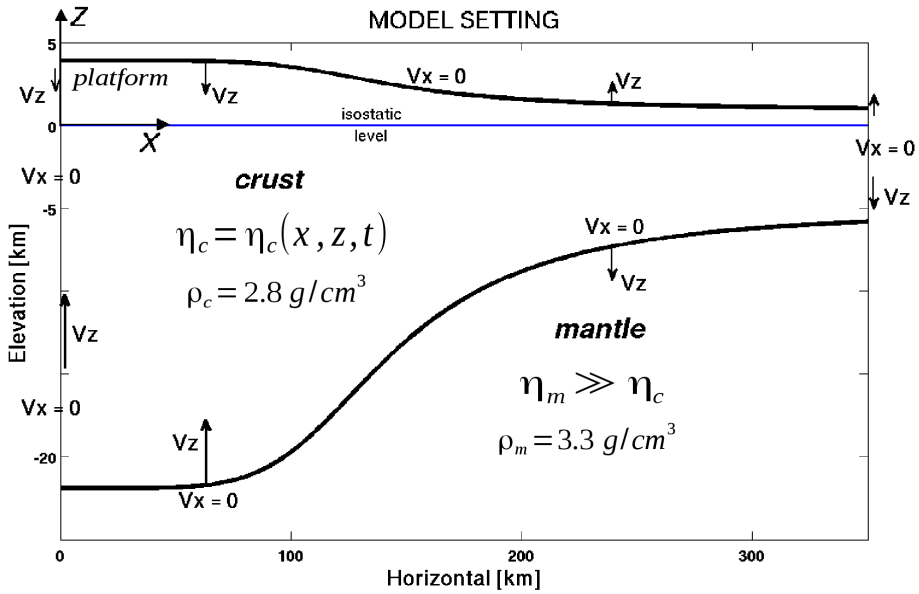

Figure 2.4. Model sketch: The 2.8 g/cm^3 crust is in isostatic equilibrium with a 3.3 g/cm^3 mantle, therefore providing our reference level for the elevation. Mass transport is computed using a 2D thin-sheet approximation of the Stokes flow equation, where the crust is described as a Newtonian fluid with space- and time-dependent viscosity. The imposed boundary conditions are summarized as zero mass flux at the lateral boundaries, and horizontally-rigid upper and lower boundaries.

The above boundary conditions are formulated mathematically in Appendix A.

2.2.1.2 Initial Condition

Due to the nature of the partial differential equations we are solving, the initial condition for the velocity field is determined by the initial conditions of the topography (bathymetry) and the initial temperature field, which in turn determines the initial viscosity structure. Let's consider *x* as the horizontal coordinate, *t* the time, and *h(x,t)* the bathymetric height function.

We adopt an arbitrary but convenient form for the initial bathymetry function:

$$h(x,0) = h_{crust} + h_{platform}(x) \tag{3}$$

where: $h_{crust} = \frac{6[km]}{(1+f)}$ (4)

(with $f = \frac{\rho_c}{(\rho_m - \rho_c)}$ an isostatic factor);

therefore h_{crust} is the constant elevation of the top of a 6 km-thick background crust over the isostatic equilibrium reference level (determined by the combination crust vs. mantle densities). This equilibrium level is taken here as the reference for the vertical coordinate, so the crustal lower boundary is defined simply by $-f \cdot h(x,t)$.

$$h_{platform}(x) = \frac{H_{plat}}{\sqrt{\left[1 + \left(\frac{x}{x_0}\right)^{Nsteep}\right]}} \tag{5}$$

is the platform thickness function, with N_{steep} an even number and H_{plat} the platform's initial maximum thickness. This initial platform function mathematically corresponds to the Butterworth filter equation.

The platform's horizontal length scale is ~35% of the model box's horizontal length, $x_0 = 0.35\,L$. The effect of the value of the exponent N_{steep} is investigated in the sensitivity analysis of Appendix C. The effect of the functional form for the initial bathymetric profile is also addressed in Appendix C.

2.2.1.3 Variable Viscosity

Like *Jones and Maclennan* [2005] we assume that viscosity is solely a function of temperature:

$$\eta = \eta_{solidus}\, e^{[(a/T_{om}) - a]} \tag{6}$$

upon which we impose the restriction $\eta_{min} \leqslant \eta \leqslant \eta_{max}$ in accordance with physical criteria (Appendix A.3).

This is a reasonable approximation for the range of depths and thermodynamic conditions present in the crust, where pressure-dependence of viscosity is of secondary importance. The thermal field consists of two components: (1) Thermal aging of the crust, described by a half-space cooling model and adapted for sub-horizontal topography [*Jones and Maclennan*, 2005]. Additionally, a constant horizontal age gradient is considered due to the lithospheric age increase moving southward from the Galápagos spreading center. (2) A hot thermal perturbation of variable strength (decreasing away from the platform area) is added to account for the continuous injection of magma into the lower crust due to the melting mantle plume beneath the platform, which, of course, is the cause of the widespread volcanism. This component has the form of a 2D Gaussian perturbation centered at the platform side of the model box and at Moho depths. For simplicity, its amplitude remains constant in time.

A complete description of the Temperarure-Viscosity parameterization is given in Appendix 2.7.A.3 section.

2.2.2 Modeling Calculations

The model equations (Appendix 2.7.A) are obtained from the thin-sheet approximation of Stokes flow with space- and time-dependent viscosity, and are solved numerically using finite differences in space and time. The computer program was written in C language and is available from the first author upon request. Post-calculation output graphics, plots and animations were done in Matlab. The finite difference grid adapts to the time-changing geometry of the crust. Integrals over the vertical coordinate were carried out using Simpson's rule for quadrature. Time integration of the controlling equation was done using an explicit second-order Runge-Kutta scheme, also known as the "improved Euler method." This scheme yields second order accuracy. Numerical solution was intrinsically carried out in non-dimensional form with scaling parameters based on L (system's horizontal length), c (aspect ratio), ρ_c, ρ_m (crust and mantle mass densities), and η_{ave} (average crustal viscosity). Our code was benchmarked successfully with iso-viscous solutions from *Huppert* [1982] and *McKenzie et al*. [2000] (see Appendix 2.7.B).

2.3. Results

We present two models here in detail. The first is intended to apply to the Southwestern Escarpment Transect (SWT) and the second to the Eastern Platform Transect (EPT). These two models were optimized to match approximately the bathymetric and age constraints, and the reader is referred to the model sensitivity analysis in Appendix 2.7.C for a detailed explanation of model parameter trade-offs.

Table 1. Model Parameter Values

Parameter	SW Transect	EP Transect	
L	350 km	350 km	Transect horizontal length
H_{plat}	3 km	2 km	Platform height at x=0
x_c	0.35	0.35	Platform horizontal length scale *
n_{steep}	10	6	Escarpment slope exponent *
BCT	6 km	6 km	Background crustal thickness
L_{Tx}	0.3	0.45	Thermal pert. horizontal length scale*
L_{Tz}	2.3	2.3	Thermal pert. vertical length scale*
η_{min}	$4 \cdot 10^{17}$ Pa·s	$1 \cdot 10^{17}$ Pa·s	minimum viscosity
$\eta_{solidus}$	$4 \cdot 10^{18}$ Pa·s	$1 \cdot 10^{18}$ Pa·s	solidus viscosity
η_{max}	$4 \cdot (10^{22}+10^{23})/2$ Pa·s	$1 \cdot (10^{22}+10^{23})/2$ Pa·s	maximum viscosity
$Age_{ini}(x=0)$	9 Myr	4.5 Myr	Initial crustal age at x=0
$\Delta age_{transect}$	10 Myr	8.5 Myr	Along-transect age variation **
$T_{evolution}$	1 Myr	3 Myr	Total evolution time span
ρ_{crust}	2.8 g/cm^3	2.8 g/cm^3	crust density
ρ_{mantle}	3.3 g/cm^3	3.3 g/cm^3	mantle density

(*) The parameters x_c, n_{steep}, L_{Tx}, L_{Tz} are non-dimensional

(**) The age variation '$\Delta age_{transect}$' along the EP transect could be larger (by ~5 Myr), depending upon the history of motion of the 91°W transform, following Mittelstaedt et al. [2012].

The parameters Hplat, xc, nsteep, apply solely as initial conditions.

2.3.1 Southwestern Escarpment Transect

This transect (Figure 2.1b, "SWT") is 350 km long and spans from the central platform across the Great Southwestern Escarpment and onto apparently normal seafloor of age ~20 Ma. The central platform lithospheric reference age at the northeastern end of the transect (and west from the 91°W transform fault) is 10 Ma. These are just reference ages, considering that in our model a hot-thermal perturbation will be superimposed in association with the plume and active volcanism (implying thermal rejuvenation). The reference viscosity values are $visc_{min}=4 \times 10^{17}$, $visc_{solidus}=4 \times 10^{18}$, and $visc_{max}=4 \times (5.5 \times 10^{22})$, all in [Pa·s], the factor 4 finally chosen to yield an adequate process duration; all in reasonable agreement with *Jones and Maclennan* [2005], *Hirth and Kohlstedt* [1996], *Mackwell et al.* [1998].

The somewhat arbitrary initial condition includes a 3 km-high platform with a slope exponent of $N_{steep} = 10$, approximately matching the present-day heights over the background seafloor. We assumed a 6 km-thick background crust, in agreement with *Ito et al.*, [1997], and with seismic studies for the Nazca plate [*Contreras-Reyes and Carrizo*, 2011]. The initial background thermal field is referenced to 1 Myr ago, consistent with the approximate age of this part of the platform [*Harpp and White*, 2001; *Geist et al.*, 2008] so that the reference ages of the thermal field were 9 Ma and 19 Ma at the northeastern and southwestern ends of the transect, respectively. The effect of continued heating associated with magmatic intrusion into the platform is simulated by a hot thermal perturbation with length-scale $L_{Tx} = 0.3$ (see Appendix 2.7.A), (Table 1 summarizes the model parameter values for the transect). As will be seen, within less than 1 Myr the model quickly relaxes toward a natural quasi-steady-state profile in bathymetry and particles velocity.

Figure 2.5 shows snapshots of the evolution of this model over a 1 Myr period from the initial condition in terms of the viscosity and horizontal velocity fields. The viscosity field evolves only slightly (solely by crustal aging or cooling, while dominated by the hot thermal perturbation), while the horizontal velocities decrease by more than an order of magnitude as the model "relaxes" from its initial bathymetric profile shape to a more stable flow front shape. As expected, the flow is mainly confined to a lower-crustal region where there is a constructive combination of low viscosity (hot and weak material) and a non-zero driving force (bathymetric gradient above).

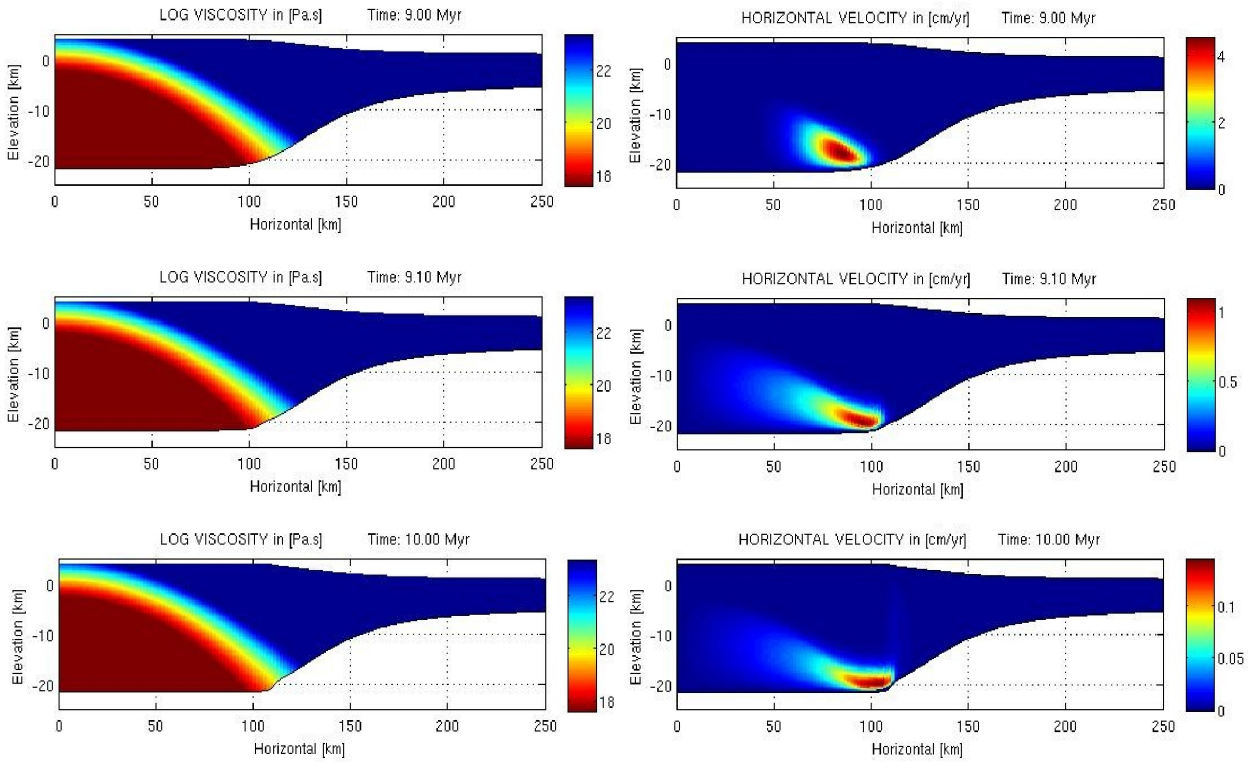

Figure 2.5. Southwestern platform transect system evolution. Note the changing scale of the horizontal velocity component. The system evolves rapidly during the early stages, hence the uneven spacing of the snapshot times. The small region affected by lower crustal flow driving forces moves slightly away from the hot and weak region, and the background crust cools down by aging; therefore further flow and deformation are hampered with time. Original model box's right end has been cropped for illustration purposes.

As suggested in the introduction, for this transect we are particularly interested in the evolution of the bathymetric gradient, with the hypothesis that backward tilting of the behind-the-escarpment region may be the cause of the unusual observed backward-stepping lava terraces. With regards to typical submarine volcanic morphologies, mere fractions of a degree of backward tilting would suffice to limit the extent of lava flows spreading away from the platform toward the SW.

Figure 2.6 shows the bathymetry, its slope, and the time-derivative of the slope (bathymetric tilting rate or angular velocity) at the logarithmic times {9.0, 9.01, 9.1, 10} Ma. As time progresses, there is a slight decrease (total of ~40 m) in platform height while an acute escarpment-hinge with an increased slope region just below develops, all accompanied by horizontal advancement. The tilting rate exhibits two opposite-sign regions: a forward tilting (steepening) region at the foot of the escarpment and a backward tilting (becoming more horizontal) region at the top and behind it. Figures 2.7, 2.8 and 2.9 show essentially the same information, displayed as two-dimensional plots over a continuum time domain (9-10 Ma). The color-coded plot of the tilting-rate shows the backward-tilting region in hot colors. The rates decrease in time (asymptotic behavior) as they translate horizontally with the flow front.

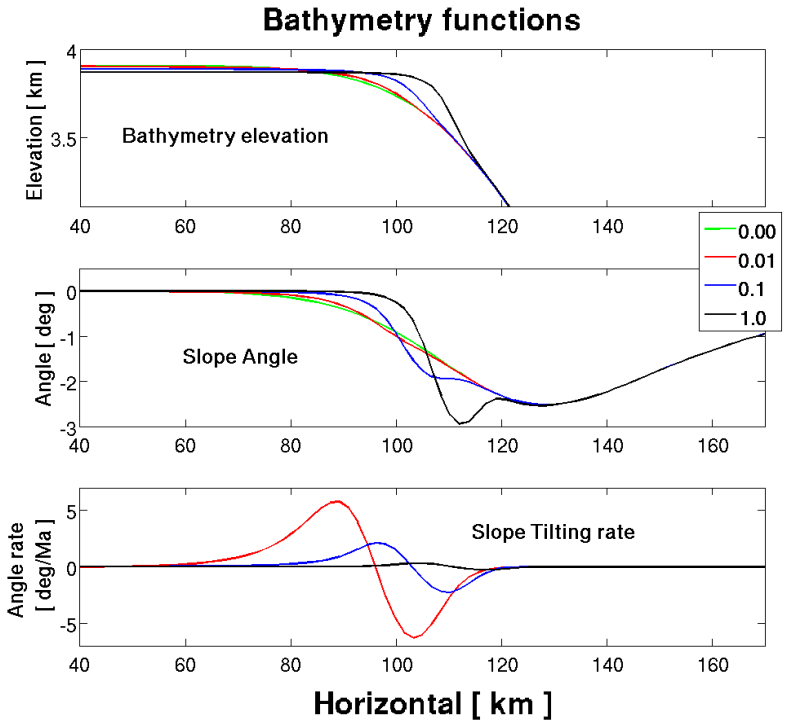

Figure 2.6. Topography functions: *h(x,t)* and spatio-temporal derivatives (slope angle and slope-angle time rate). Time snapshots are represented by color code. Legend at center-right is valid for the three plots; color goes as green-red-blue-black as time increases: numbers indicate millions of years since reference initial time (9 Myr).

Figure 2.7. Bathymetry as a function of *x* and *t*. Measure is in km referenced to the buoyancy level (isostatic) of a 6 km-thick crust (2.8 gr/cc) over the mantle (3.3 gr/cc).

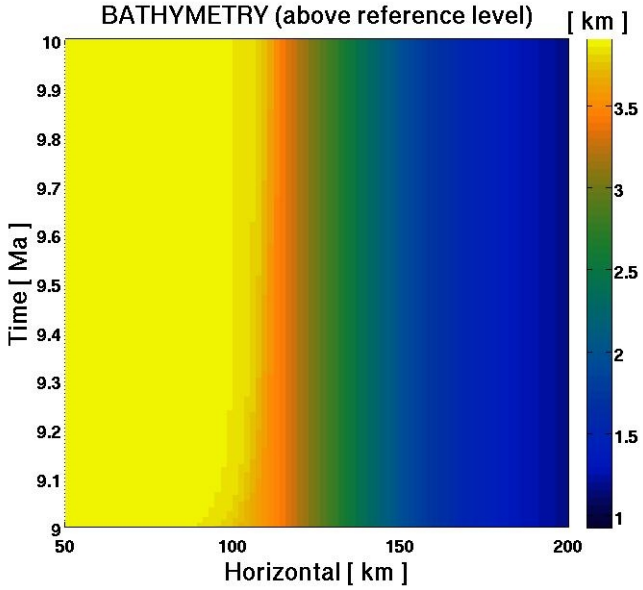

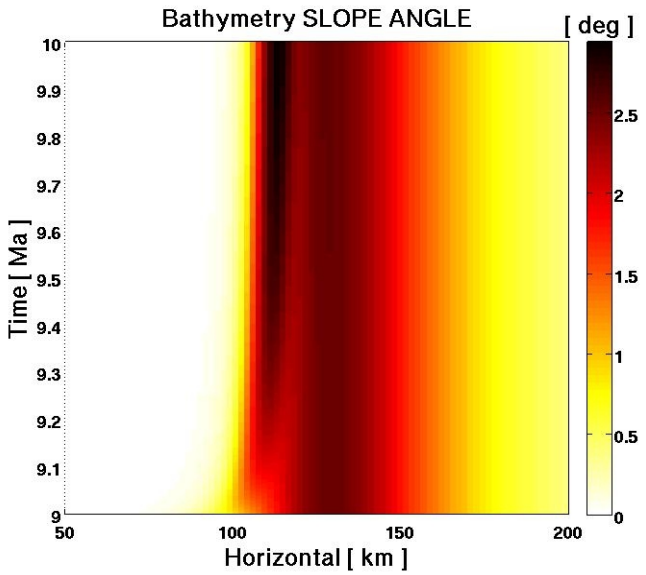

Figure 2.8. Bathymetry slope angle as a function of *x* and *t*. Angle measured in degrees, orientational sign discarded.

Considering a bathymetric surface segment (between fixed points in the horizontal) and measuring its slope-angle vs. time gives an account of the angular conditions that would control the spreading of lava flows over this bathymetric surface segment. For instance, we have isolated a fixed 10-km interval in the horizontal: (81,91) km (grid-dependent), and we have measured the spatial average of the bathymetric slope-angle over it, as a function of time (double checked by integrating the space-average tilting-rate over time), then plotted this in Figure 2.10. The result is that an initial slope-angle of ~0.28 degrees is progressively reduced in time, rendering the surface more horizontal, down to a final slope-angle of ~0.01 degrees after 1 Myr. The process is rapid at the beginning: roughly 90% of the angular reduction occurs during the first quarter million-years. This behavior can also be appreciated in the bathymetry-derivatives profiles of Figure 2.6.

Similar results are obtained for other averaging intervals in the proximity of the platform edge and the escarpment, and in general for other sets of parameter values. The initial average slope over the chosen interval, the process duration, and the final slope over the interval were found after a parameter-space search, and are geologically relevant in a submarine volcanic environment [*Stephen Self*, 2014, personal communication]. For instance, the viscosity values were chosen in order to adjust the duration of the process, and are specific for this study transect. Owing to the viscosity values and the length-scale of the hot thermal perturbation, the horizontal particle displacements (mass transport) in the lower crust during the 1 Myr time span are about 8 km: the flow is braked by the high viscosities beneath the escarpment and the off-platform crust. In this way we tried to mimic the flexural conditions prevailing there as suggested by the gravimetry-inferred lithospheric compensation mechanisms [*Feighner and Richards*, 1994].

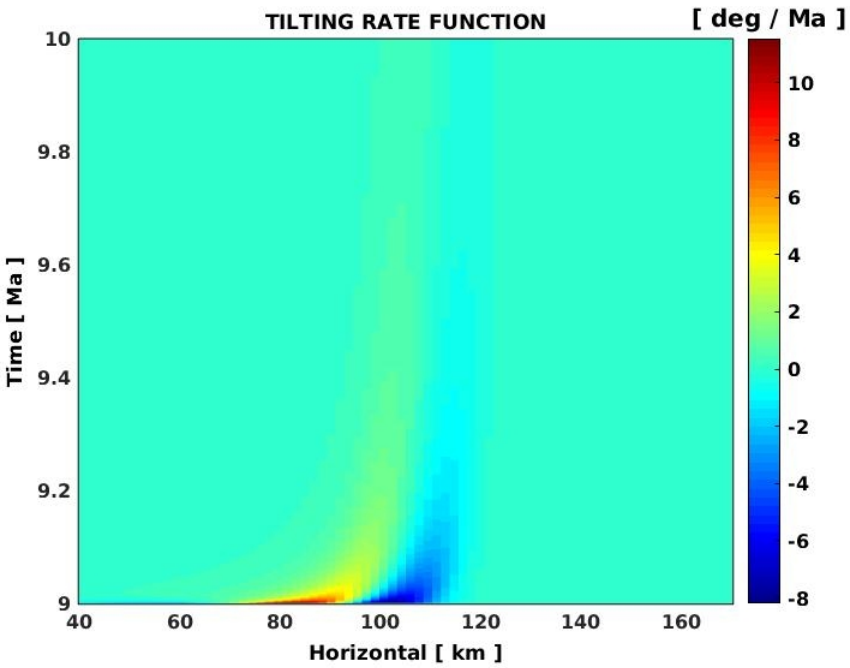

Figure 2.9. Bathymetric tilting rate, as a function of *x* and *t*. A forward tilting region (cold colors) on the foot of the escarpment and a backward tilting region (warm color) at the top of it are present, with high rate values at the beginning and attenuating in time.

Mass transport away from the platform-center due to lower crustal flow causes the sub-horizontal portion of the platform bathymetry to become more horizontal as the flow progresses. While this process occurs generally for these types of dynamical settings, in our model a highly viscous (stiff) crust suffering minimal mass transport produces the required backward-tilting (fractions of a degree) of the sub-horizontal platform region behind the escarpment.

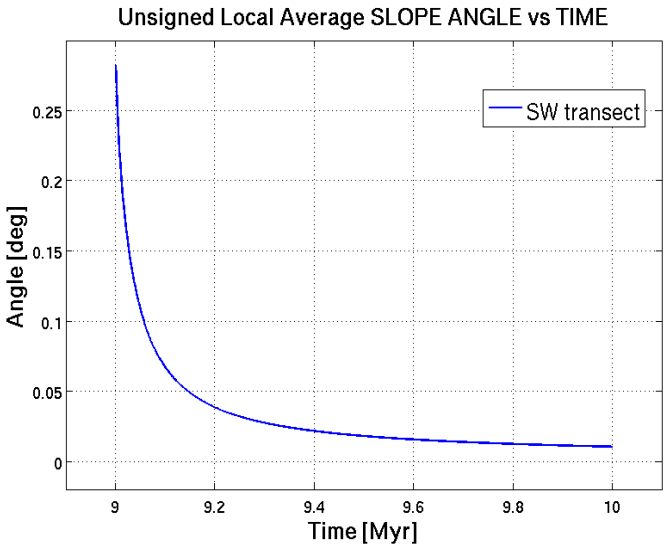

Figure 2.10. Slope angle vs. time, as defined by the bathymetry of the sub-horizontal platform's upper edge. Plotted value is the unsigned local average slope angle over the interval *x* in [81,91] km (values chosen according to the grid). Over this 10 km length span, the tilting rate has a backward sense at all times. At 0.25 Myr after the initial time, the tilting process has reduced the initial angle by 88%.

2.3.2 Eastern platform transect

This transect (Figure 2.1b, "EPT") is 350 km-long and extends from present-day background crust reference thermal ages of 7.5 Myr under the central platform (and east from the 91°W transform fault), to 16 Myr (or possibly as much as 20-22 Myr following *Mittelstaedt et al.* [2012]) off the platform toward the southeast.

The reference viscosity values are $visc_{min}=10^{17}$, $visc_{solidus}=10^{18}$, $visc_{max}= 5.5 \times 10^{22}$; all in [Pa·s]. The value of $visc_{max}$ was chosen as the arithmetic mean between 10^{22} and 10^{23}. The system is not very sensitive to these parameters, and the values chosen are reasonable for the shallow crust. The other two viscosity values were chosen to obtain reasonable time scales and a significant degree of flow-front advance in the bathymetry (a likely effect owing to the weak thermo-mechanical conditions) (see sensitivity analysis in Appendix 2.7.C, section on time scales and front advancement vs. viscosities). These values are in reasonable agreement with *Jones and Maclennan* [2005], *Hirth and Kohlstedt* [1996] and *Mackwell et al.*[1998].

For the initial condition on bathymetry a 2 km-thick platform was chosen. This platform thickness value is justified because: (i) present-day local platform relief is between 1 and 2 km (approximately); and (ii) owing to the mechanically weak conditions on the eastern platform region, the construction of a thick, high elevation volcanic platform is precluded by relaxation of the lower crust. The initial bathymetry slope exponent is $N_{steep} = 6$. This value was chosen after exploration of its effect on the final state of the bathymetry after 3 Myr of evolution (see Appendix 2.7.C). We assumed a 6 km-thick background oceanic crust, in reasonable agreement with *Ito et al.* [1997] and with *Contreras-Reyes and Carrizo* [2011]). Table 1 summarizes the model parameter values for the transect.

The initial condition on the thermal field is referenced to 3 Myr ago, so the reference thermal ages at the transect extremes are 4.5 Myr at the platform-center end and 13 Myr (or perhaps up to 18 Myr) at the off-platform end toward the southeast (this uncertainty does not have a big effect on the system behavior due to locally high viscosities). Nevertheless, the duration of this tectonic episode, even after parameter exploration, is considered a weakly constrained quantity. Certainly, construction and morphological shaping episodes within this area of the platform have occurred during the last ~5 million years [*Geist et al.*, 2008], but the timing uncertainties are large (see discussion section). The hot thermal perturbation's horizontal length scale was, after parameter space investigation, chosen to be $L_{Tx} = 0.45$. This rather large value is consistent with the weak central platform and hotspot track type of environment [*Feighner and Richards*, 1994], and with the transect location and orientation. Figure 2.11 shows snapshots of the model evolution over the 3 Ma time-span. Owing to the asymptotic behavior exhibited by the system, snapshot time-spacings are chosen accordingly, and the snapshot times represent the reference ages of the background crust at the platform-center end of the transect (from 4.5 to 7.5 Myr).

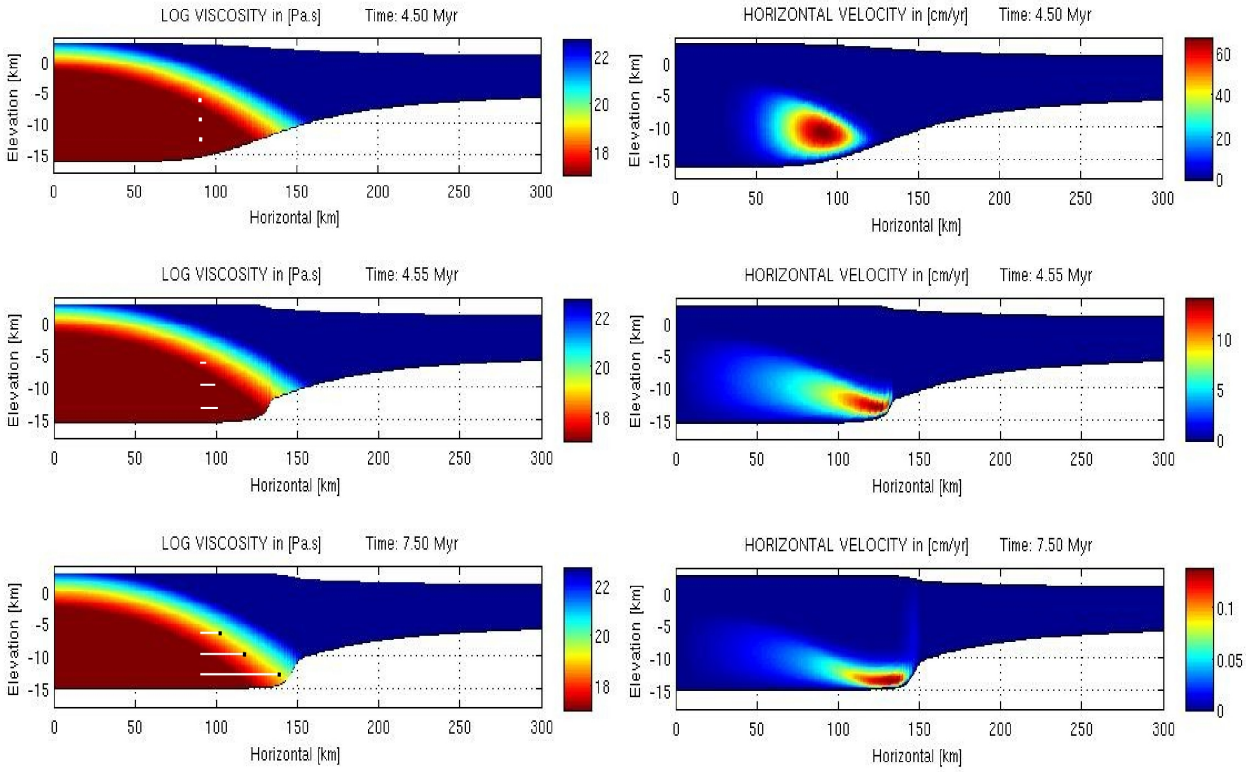

Figure 2.11. Eastern platform transect system evolution. Note the changing scale of the horizontal velocity component. The system evolves rapidly during the early stages, hence the uneven spacing of the snapshot times. The material portion affected by lower crustal flow driving forces moves away from the hot and weak region. After a transient period lasting less than 1 Myr, the system has developed a bathymetric flow front that advances without changing its shape significantly. The flow front evolves asymptotically toward a steady state. Original model box's right end has been cropped for illustration purposes. We have estimated the position of three particles vs. time to show accumulated displacement: drawn as white markers leaving a tail (shown only on the left plots), with their final position as black dots. Vertical motion has been neglected.

The viscosity field evolves only slightly (solely by thermal aging and barely resolved by the color scale) and is dominated by the hot thermal perturbation. The horizontal velocities decrease dramatically in time: the region of high velocities, initially with values of about 50 cm/yr, becomes progressively confined to a narrow and deep crustal region with final values of order 0.1 cm/yr causing the “relaxation” of the system from its initial bathymetric profile shape to a more stable flow front. As expected from the theoretical standpoint, flow is mainly confined to a lower-crustal region where there is a constructive combination of low viscosity (hot and weak material) and a non-zero driving force (bathymetric gradient above). The initial platform thickness is 2 km (full bathymetric height 2.909 km above the isostatic reference level), and after 3 Myr of evolution the final thickness is 1.79 km (2.699 km over the reference) (see Figures 2.12 and 2.13), close to the observed bathymetric height differences across the eastern platform

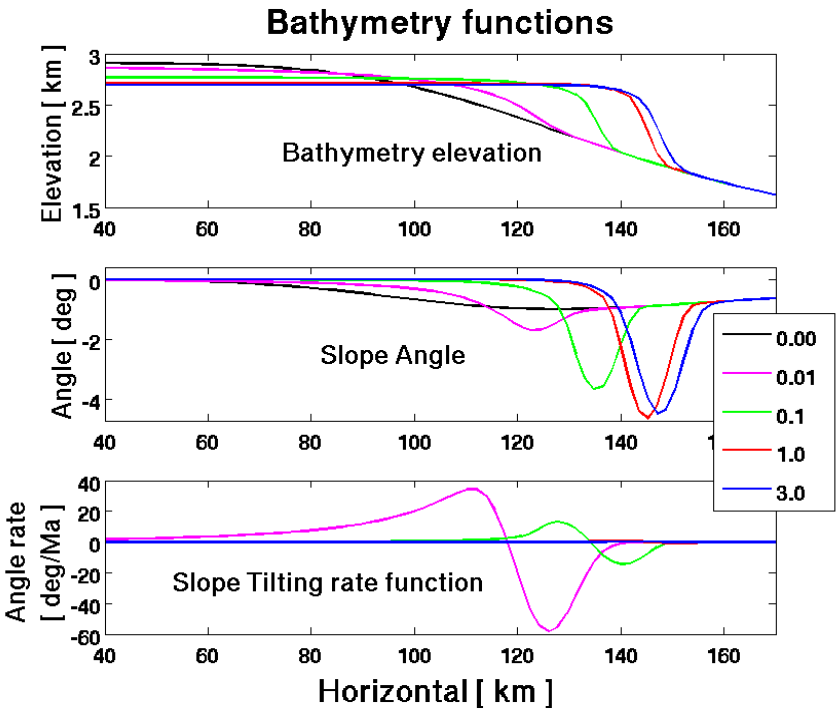

Figure 2.12. Topography functions: *h(x,t)* and spatio-temporal derivatives (slope angle and slope angle-time rate). Time snapshots are represented by color code. Legend at center-right is valid for the three plots; numbers indicate millions of years since reference initial time (4.5 Myr).

escarpment of about 1.5 km (over horizontal distances of around 20 to 30 km, measured along the transect). This height reduction is a consequence of mass conservation: the platform "deflates" by evacuation of the material from its lower regions. The system develops a well-defined bathymetric front of increasing slope. Figure 2.14 (upper) shows the locus of maximum slope (green) vs. time, and the loci of slope 20% of that maximum (red). Within these limits the average slope is computed (region of at least 20% the maximum) and it is found to increase in time up to a final value of ~5.4% (Figure 2.14, lower). This value is approximately the observed present-day slope value of the eastern platform escarpment in the vicinity of Isla Española (Figure 2.1a).

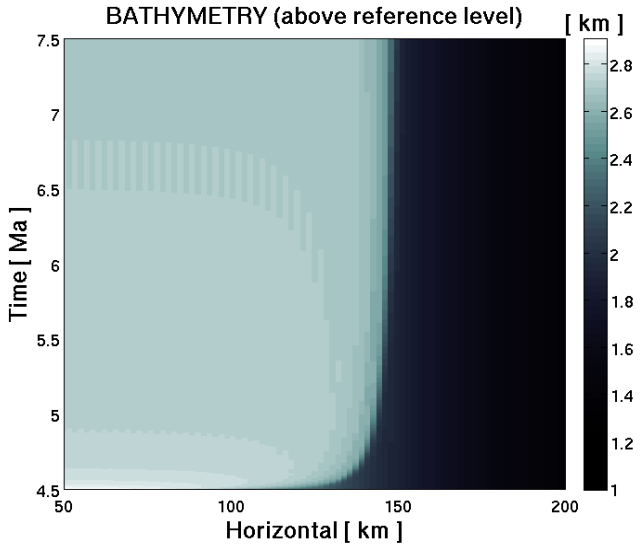

Figure 2.13. Eastern platform bathymetry evolution during the 3 Myr model time span. The system evolves rapidly during the early transient period. After roughly 0.5 Myr, the bathymetry shows a well-defined front that advances asymptotically toward a steady state.

The system experiences surface flow front displacement of order 30 km during the 3 Myr time-span (Figures 2.11-2.14), but we note that given the boundary condition the horizontal velocity is zero on the bathymetric surface. Therefore this front merely follows the isostatic response to the redistribution of mass underneath. Total maximum horizontal particle displacements within the deforming lower crust are of order ~50 km (shown in Figure 2.11). This displacement is away from the central platform and along the direction of the transect. This result has geochemical implications that are treated in the discussion section.

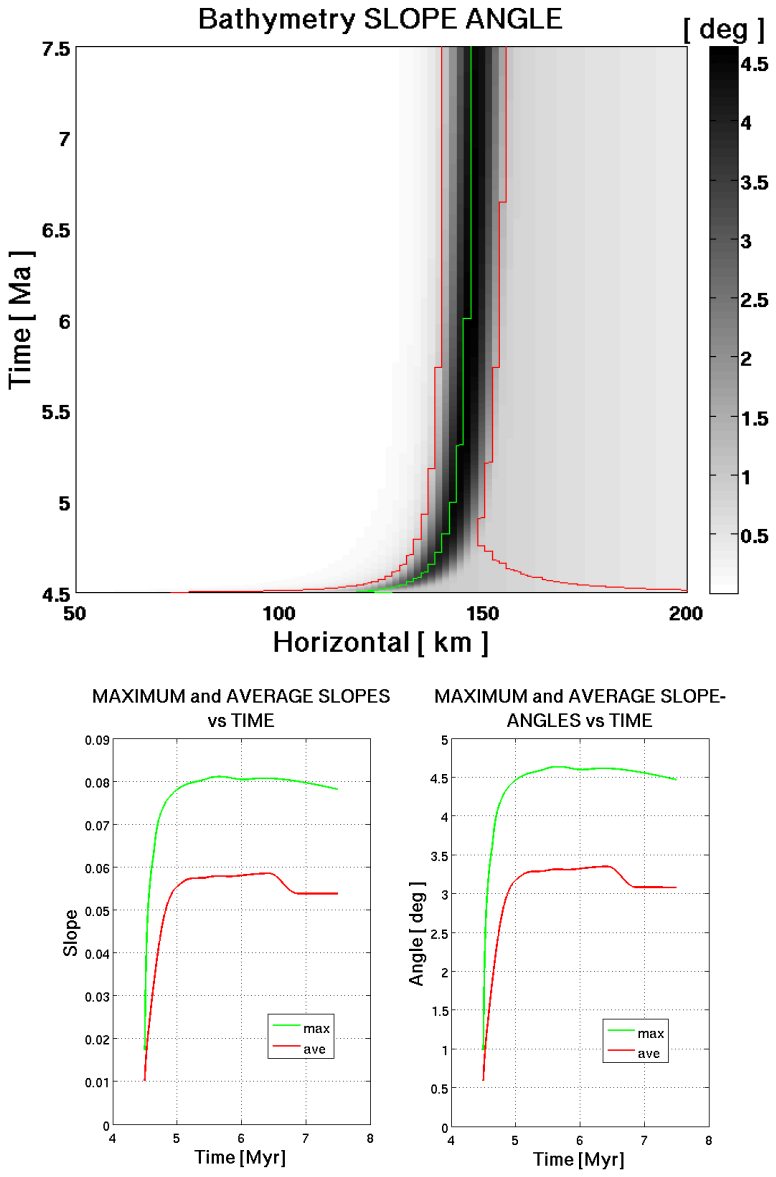

Figure 2.14. Bathymetric Slope Angle function (above) with markers for the maximum slope location (green) and the points where the slope is 20% of the maximum (red). Using these slope-value defined bounds, the spatial average flow-front slope is computed as the mean value inside that region, for all times. These values are then plotted as slope and slope angle (below).

In summary, the bathymetric contrasts (lithostatic pressure gradients) on this young hotspot-affected lithosphere suggest that lower crustal flow is likely, and our simulations account reasonably for some basic observed bathymetric features; hence, our label 'Proposed Flow Front One' (PFF1) in Figure 2.1b.

2.4. Discussion

2.4.1 Southwestern escarpment transect

Feighner and Richards [1994] showed that the Great Southwestern Escarpment (GSE) and nearby off-platform crust are located over flexurally supported lithosphere with elastic thickness ~12 km, but that its upper edge is located over a narrow transition to near-Airy isostatic compensation towards the northeast [see *Feighner and Richards*, 1994; Figures 12a and 13a]. Therefore, the thermally weakened regions close to the escarpment may undergo lower crustal flow away from the platform towards the southwest, with flow blocked by the stronger off-platform lithosphere to the southwest that remains undisturbed by Galápagos-related volcanism.

A key focus of this study is to try to understand what processes control the emplacement of the spectacular lava flow terraces off the GSE as mapped by *Geist et al.* [2008]. A working hypothesis is that the seemingly-unique backward-stepping nature of these terraced flows indicates regional ("backward") tilting toward the central platform during emplacement. Surface slope-angles of massive lava flows cooled in oceanic environments, averaged over distance, are typically less than ~1 degree. These are the slopes that control the subsequent lava runoff of future extrusive events [*Stephen Self*, 2014, personal communication; *Deschamps et al.*, 2014; *Umino*, 2012]. Given that the driving force of any lava flow is the along-the-slope gravity component, a mere fraction-of-a-degree modification of the slope-angle on these surfaces would alter the runoff distance of future lava flows.

For the GSE, we have demonstrated that even very small amounts of lower crustal flow (less than 10 km of horizontal mass displacement) may suffice to tilt the bathymetric sub-horizontal upper parts of the platform (behind the escarpment's edge) in a backward sense, with total angular decreases of more than 90% of the initial slope-angles during a time span of 1 Ma. The platform surface, becoming more horizontal with the ongoing mass-transport in the lower crust, experiences a decreasing along-the-slope gravity component with time. Thus, lavas flowing over this backward-tilted surface would experience a decreased driving-force, which eventually may cause the full braking of the lava flow (by viscous dissipation), on the time-scale of thermal diffusion (cooling of the lava). Lava flows will then cool down and stop before the flow edge of older events (past eruptive episodes), creating a receded step. This mechanism may operate successively, thus creating a system of stepped terraces, significantly differing from typical basalt flow-fields in which lava flows cool down over horizontal distances not necessarily ordered with respect to previous flows. In this way, the mechanism outlined here and shown to operate for appropriate model conditions applying to the southwestern escarpment region, may explain the unique morphology of the GSE. A key aspect on the applicability of our idealized isostatic model to the real Earth scenario in which there is a spatial transition from isostasy (central platform) to flexure (off-platform) in the vicinity of the platform-edge, is given by the high viscosities on the under-the-escarpment and off-platform crustal regions chosen for the model, which are all above 10^{21} Pa·s, primordially owing to the short thermal perturbation length scale (L_{Tx} = 0.3, see snapshots on Figure 2.5), with minimal mass transport. We believe this 'highly damped' crustal flow scenario is appropriate for a region of the Galápagos crust bounded by a flow-resistant flexural lithosphere.

Aside from the volcanic sources on the platform, magmas might be extruded directly from the escarpment surface, stemming from a dike-and-sill complex that likely exists there beneath the platform surface as part of the magmatic system. The locations of the vents for the terrace-building lava flows are unknown, but the high-resolution imaging of *Geist et al.* [2008] suggests that lavas may be extruded directly from the GSE itself as massive 'break outs', producing a system of basaltic lobes.

Along the GSE numerous steps/terraces have been imaged [*Geist et al*., 2008], exhibiting widely different horizontal extents and vertical relief. A plausible scenario is that each step is the accumulation of several shoaled lava flows stemming from a single eruptive episode [*Geist et al.*, 2008]. The differences between the individual heights and volumes of different steps could then be related to the spatio-temporal eruptive behavior, modulated by bathymetric tilting associated with lower crustal flow. According to our models (Figures 2.5 - 2.10), eruptive events occurring during episodes with total durations of $<10^3$ years would experience a quasi-static bathymetric profile (owing to system response timescales $>10^4$ years), and progressive lava flows should produce the natural slope-angles of the bathymetric surface after cooling. For subsequent eruption episodes occurring ~ 10^4 - 10^5 years after a quiescence period (with few or no eruptions), owing to the accumulated tilting given the system's response, lava flows will encounter a more sub-horizontal surface. Figure 2.15 illustrates how long-term tilting between lava flows could result in backward-stepping lava terraces. Variations in the durations and volumes of eruptive episodes, as well as in the platform tilting-rates, would cause variations in the thicknesses and volumes of the terrace steps. The aforementioned timings, in accordance with our modeling results, are considered reasonable for Galápagos volcanism [*Nauman et al.*, 2002; *Geist et al.*, 2014].

Finally, we recognize that in some situations volcanic platforms in oceanic settings may be “planed off” by sea level erosional processes, as suggested for certain features along the Hawaiian ridge [e.g., *Mark and Moore*, 1987; *Moore*, 1987]. However, *Geist et al.* [2008] discuss at length why these mechanisms cannot explain the deeper (> 1 km depth) terraces along the GSE, and show that these terraces consist of a vast collection of rugged and irregular lobes, or “tongues” of basaltic lava flows. Some degree of continuity and smoothness (more familiar of coastlines erosional processes) are found only in the most shallow slopes of the GSE, where sea level effects might plausibly have come into play over the last few million years during which the GSE must have formed. However, the paleo-seashores suggested in the paleogeographic study of *Geist et al*. [2014] do not suggest that the GSE volcanic terrace features identified by *Geist et al*. [2008] were formed at or above sea level, instead, they suggest that such region of the platform grew totally under submarine conditions.

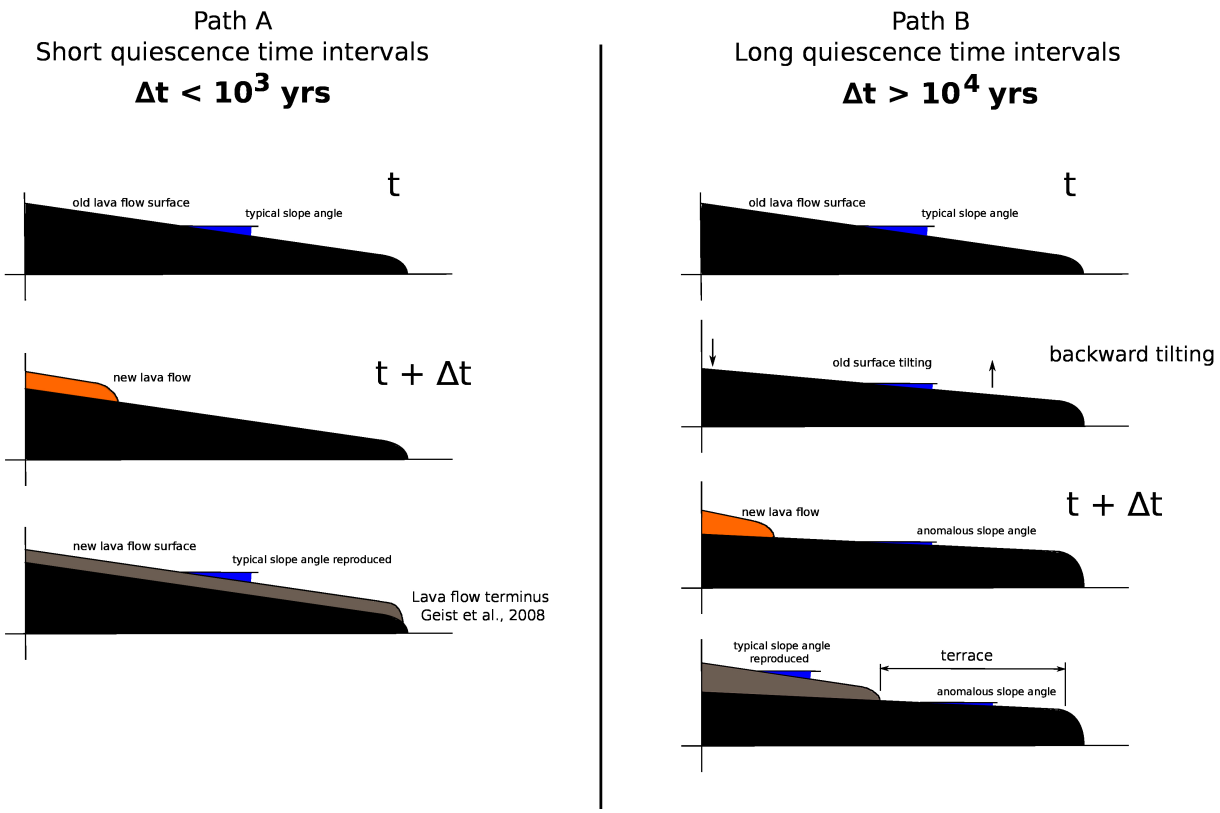

Figure 2.15. Two possible paths on volcanic construction over the platform surface: In Path (A) eruptions are relatively frequent (quiescence time intervals < 10^3 yrs) so that lava flows encounter typical slope angles. Subsequent flows, after traveling relatively long distances, cool and reproduce these typical slope angles. In Path (B) a period of quiescence of limited or null volcanic activity lasting more than 10^4 yrs allows enough time for platform surface backward-tilting in response to lower crustal flow, rendering the surface more horizontal, and thus altering the style of subsequent lava flows: long-distance flow is hindered. The system can take any of these paths during its evolution (emplacement of the escarpment), and certainly alternate them in a time sequence lasting million of years. Note 1: The timescale of individual lava flow (order ~days-weeks) is neglected, as it is very small compared with Δt. Note 2: Slopes have been exaggerated for illustration of the effect.

2.4.2 Eastern platform transect

The eastern platform exhibits less prominent bathymetric contrasts than the GSE, but with a distinctive morphological feature: a rim-like, asymmetric ridge or escarpment. This structure is about 180 km long, with Isla Española forming the most elevated part, and with mild horizontal curvature along its northern parts, just east of Isla San Cristobal. When measured along the study transect and neighboring areas, the associated elevation contrasts are ~1.5 km over horizontal distances of ~20-30 km, corresponding to slopes of ~5 - 6% (~3.2 degrees). The overall shape of this bathymetric structure suggests a front associated with lower crustal flow. Due to the eastward migration of the plate with respect to the Galápagos hotspot [*Hey*, 2010], the eastern platform was not only younger but considerably hotter and weaker in the recent past, likely undergoing intense deformation. Based on these considerations we hypothesize that this bathymetric rim is the surface expression of lower crustal flow away from the platform and towards the southeast, occurring over the last ~3 Myr, and now having reached a mature, or perhaps "stagnant" stage.

Feighner and Richards [1994] inferred a transition from near Airy isostasy to elastic flexure southeast from the present-day location of PFF1, close to Española island. Nevertheless, considering that 3 Ma ago this region was hotter and weaker due to the presence of the Galápagos plume [*Geist et al.*, 2008; *Werner et al.*, 2003], we propose that this area may have been relatively weak compared to the present-day GSE. In our modeling, this weakness is reflected in the younger effective plate ages, smaller viscosity values (factor of 4), and larger horizontal length scale of the hot thermal perturbation (L_{Tx} = 0.45). Crustal age uncertainties in the southeastern Galapagos (shown for example in Figure 2.1b) would imply bigger age gradients along the transect, but ultimately, they have only a small effect on the results presented here.

Our simulations used initial platform thicknesses of 2 km, as explained in the Results section. In our preferred simulation, after 3 Myr of evolution the model exhibits a final platform thickness of 1.79 km and a final average slope across the escarpment of ~5.4% (although this value is dependent on how the average is taken), consistent with observations. There is an initial transient period that depends on our arbitrary initial conditions, and lasts for about 0.5 Myr during which high strain-rates and rapid front advancement occur. As seen in Figures 2.13 and 2.14, the position of the surface front advances monotonically at a speed that decreases with time. The front's horizontal position behaves asymptotically in time (all variables showing decreasing time-rates).

In these simulations, the lower crust undergoes high shear-strains and suffers sub-horizontal mass displacement, represented by channelized flow whose velocity distribution is shown in Figure 2.11. Buoyant mantle-plume melts ascending through this deforming crust would not follow purely vertical trajectories, as they would be partially advected with the flow (away from their original mantle upwelling regions in the central-west platform) toward the southeast. Calculating typical values of total horizontal displacements due to flow of the lower crust in the 3 Myr time-span of our simulation, we find values of ~ 50 km (with more than 80% of it occurring during the first 1 Myr),(In relation with the uncertainties of these estimates, the off-platform crustal ages uncertainty for this transect may be as large as 5 Myr (following the study

of *Mittelstaedt et al.* [2012]), but nonetheless, their effect on the mobility of the lower crust is unimportant, as the viscosities in the off-platform region would be above 10^{21} Pa·s, and following our sensitivity analysis, an error of 10 km of total displacement would be too high). This 50 km-displacement (shown in Figure 2.16), whose magnitude is roughly the distance between Santa Fe and San Cristobal islands, is a significant fraction of the platform's horizontal extent. The horizontal displacement of these mantle-plume melts is proportional to the time they take in traversing the crust, which is in turn dependent upon whether they are creating a new flow channel (at the forefront of the mantle-plume tail) or exploiting a preexisting one (at some distance down-stream the hotspot track). *Keller et al.* [2013] show that the ascent speeds for melts that are creating a path through the crust, is of order 10-50 km/Myr; therefore, they would require a time of order ~1 Myr to ascend through the ~20 km-thick Galápagos crust. Accordingly, 3 or 4 Myr ago, the mantle-plume derived melts may have ascended slowly enough to have been advected horizontally by bulk transport within the lower crust, presumably carrying the plume isotopic signatures, for distances of order 40-50 km. If sufficiently buoyant to erupt at the surface, these melts might have given rise to volcanic centers extended toward the southeast of their mantle origins. Although speculative at this point, we mainly just wish to make the case that this advection process may need to be considered in future interpretations of the pattern of geochemical anomalies in the Galápagos.

This transport might therefore influence the horizontal spatial patterns of plume-like geochemical signatures, which have been the subject of considerable debate in the Galápagos [*Geist et al.*, 1988; *White et al.*, 1993; *Hoernle et al.*, 2000; *Harpp and White*, 2001]. Consider for instance the observation that the Galápagos platform exhibits more plume-like signatures on its margins [*Geist et al.*, 1988]. We note in particular the work of *Harpp and White* [2001], where complex patterns can be observed. See for example Figure 2.16 where the ratio $^{87}Sr/^{86}Sr$ shows an elongated maximum towards the southeast, perhaps consistent with directed lower crustal flow as along our eastern platform transect study, where the material flows away from the center towards the southeast. *Harpp and White* [2001]; attribute southeasterly-elongated geochemical anomalies, such as the one exhibited by the high $^{87}Sr/^{86}Sr$ of the FLO component (one of the isotopic components present in the Galápagos) to lithospheric dragging in the direction of plate motion with respect to the hostpot. Our models suggest a possible additional influence on the plume geochemical signature transport due to the deforming lower crust. Mass transport due to lower crustal flow may operate in a direction not parallel to plate motion.

The southernmost edge of the platform between Floreana and Española islands, in conjunction with the PFF1, exhibits considerable geometrical (horizontal) extension away from the hotspot track. Southeast-directed lower crustal flow occurring during the last ~3 Ma may have played a role in spreading and extending the crust locally [*Sally Gibson*, 2014, personal communication], therefore increasing, perhaps even controlling, the areal extent of the platform.

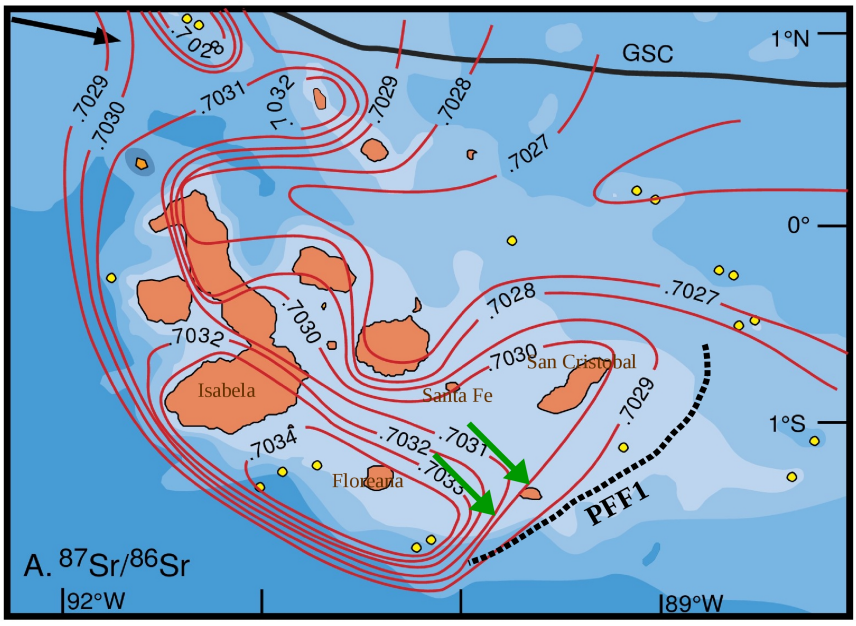

Figure 2.16. Map of the $^{87}Sr/^{86}Sr$ anomaly over the Galápagos archipelago, adapted from figure 7A of *Harpp and White* [2001]. Dashed black line marks the location of the Eastern platform escarpment, which we infer to be the surface expression of a lower crustal flow front (PFF1). Green arrows indicate the direction and magnitude of the lower crustal mass displacement, with a map-scaled length of 50 km. The elongated geometry of the Strontium isotopic anomaly might be partially explained by plate-hotspot relative movement, but here we suggest an extra component: lower crustal flow may play a role in transporting plume-like signatures with respect to the moving plate, slightly away from the hotspot track.

Another interesting feature of the eastern platform is that the present-day PFF1 is not entirely a one-sided escarpment (dipping east), as it also exhibits an elevation drop on its western side toward the central platform. Thus, there is a two-sided, or "symmetric-ridge" aspect to its morphology. The steeper eastern flank dominates the morphology, and we have modeled it as a one-sided surface flow-front. The western flank is less pronounced (lower relief and slope), and cannot be explained by the gravity flow model for lower crustal flow advancing from the central platform. We hypothesize instead that the small western slope is explained by cooling of the interior of the platform, representing a more mature stage of thermal evolution than for the GSE. Inspection of the left-hand panels of Figure 2.11 shows why this may be so: The hot thermal perturbation beneath the platform will dissipate in time as the hotspot migrates westward relative to the older part of the platform, so that an initially flat platform will sink progressively westward of the flow front as this cooling proceeds, for example, between Floreana and San Cristobal islands. Considering a local crustal thickness of ~18 km and a thermal expansion coefficient of 1.7×10^{-5} °K^{-1}, a subsidence of 100 m would require differential cooling of ~330 °K, explaining much of the ~150-200 m of the inferred local subsidence northwest from Española Island.

Regarding paleo-sealevel effects, the proto eastern platform began forming roughly ~6 Myr ago, when the hotspot located fully beneath the Nazca plate. At that time, the growing volcanic edifice was being constructed upon young plume-affected lithosphere, likely starting from fairly shallow water depths of order ~1 km. With local sea level responding to climate shifts and

plume-related dynamic topography, it is plausible that the upper parts of this proto-platform (perhaps at depths of ~0.5 km) might have formed paleo-shorelines. Accordingly, Figure 8 of *Geist et al.'s* [2014] paleogeographic reconstructions shows paleo-shorelines approximately along the present-day eastern platform escarpment ~0.5 km water-depth contour. However, a more prominent delineation of the present-day escarpment lies at the 1 km depth contour, markedly lower than the paleo-shorelines proposed by *Geist et al.* [2014]. But we also note that our eastern transect model suggests ~200 m of subsidence over a 3 Myr time span, better placing the paleo-shorelines as a cause for the present-day morphology. In any case, we suggest that it is likely that both lower crustal flow perpendicular to PFF1 and possibly paleo-shoreline effects may have contributed to the morphology of PFF1, and sorting out these effects would require high-resolution bathymetric imaging of this feature.

2.4.3 Other features possibly related to lower crustal flow

A number of other bathymetric features of the Galápagos platform (and the Carnegie Ridge to the east) may have formed as a result of episodes of lower crustal flow (Figures 2.1a and 2.1b). For example, a notable ridge to the east of the platform and forming part of the Carnegie ridge, labeled PFF2 (proposed flow front 2), shows gentle but distinctive elevation contrasts with a horizontal extent of ~250 km. The geometry of this feature is hypothesized to result from lower crustal flow starting approximately 9 Myr ago, when the hotspot was located beneath the lithosphere there. Flow would have been directed toward the SSE. Owing to local thermal ages of ~8-11 Myr and noting the lack of obvious major centers of volcanic construction, we infer relatively high lower crustal viscosities. Consequently, this flow front may be close to stagnation. We note that the reflection/refraction study of the Carnegie Ridge by *Sallarés et al.* [2005] indicates a remarkable feature consistent with the above inferences, where the thickened lower crust along the southern margin of the eastern Carnegie Ridge appears to extend horizontally beyond the bathymetric expression of volcanic construction toward the south. In other words, it seems possible that lateral spreading of warm lower crust may continue even after major volcanism has ceased. For this area, a role for paleo-sealevels in shaping the morphology is plausible, and indeed the paleo-seashores (*Geist et al.* [2014]) between 5 and 3 Myr bear some resemblance with the PFF2 escarpment. However, the local paleo-seashore is rather composed of paleo-islands, perhaps overlying a more continuous and connected feature like the one observed under the ocean today, so that sealevel erosion likely shaped only the most elevated parts of the present-day escarpment. We therefore suspect that this bathymetric feature, after been formed by magmatic intrusion, was mainly controlled by lower crustal flow and deformation.

Also shown in Figure 2.1b are localized bathymetric escarpments along the southeastern and eastern regions of Isabela island, and the northern regions of Santa Cruz island. These escarpments are important at the island length-scales and may have been created by recent volcanic construction. However, we suggest that they may be at least partially the result of recent lower crustal flow beneath this region of the platform, which is the hottest and weakest. Additional processes may have also shaped them, such as carbonate deposition on submarine slopes responding to eustatic changes.

Except for localized islands and seamounts, the central platform undergoes a smooth transition to regional background oceanic floor toward the north: no significant escarpments are observed [*Mittelstaedt et al.*, 2012]. The northern platform region represents a different dynamical regime, due to younger crustal ages and time-dependent plume-ridge interaction associated with the northward migration GSC relative to the hotspot [*Hey et al.*, 1972; *Ito et al.*, 1997].

2.4.4 Remarks on platform evolution

The Galápagos platform may be considerably more voluminous now than in the past [*Geist et al.* 2008], (Figure 2.2). Repeated and episodic crustal intrusion events are not only plausible, but also consistent with recent seismic studies. *Hooft et al.* [2010] presented seismic refraction results for the Galápagos platform, finding thickened crust and platform edges characterized by low P-velocity consistent with high porosity, whereas for the interior of the platform magmatic intrusion accounts for most of the crustal section, as evidenced by seismic velocities, where the gabbroic lower crust constitutes roughly 2/3 of the total crustal thickness. These results are consistent with the modeling results of *Feighner and Richards* [1994], where a platform crustal thickness of slightly more than 16 km is inferred, with the lower ~6-8 km likely being gabbroic intrusion added to the background crust [see also *Richards et al.*, 2013]. We also note that the westernmost islands of Isabela and Fernandina are constructed upon older lithosphere than the central platform [*Feighner and Richards*, 1994], and thus the process of lower crustal intrusion and flow there may be less prevalent.

2.4.5 Future studies

The results presented above suggest future studies that might lead to a better understanding of the evolution of the Galápagos Archipelago and GSC system. The greatest need is for combined seismic reflection and wide-angle refraction studies to resolve the structure of the crust, perhaps along transects such as those studied here. Seismic anisotropy studies could help confirm lower crustal flow, for instance on the eastern platform, due to a potential strain-driven orientation of minerals in the lower crust. In addition, the modeling work should be extended to include 3-D effects and to include predictions for stresses in the shallow crust associated with lower crustal flow, which in turn could be constrained by seismo-tectonic studies and topographic and bathymetric studies of faulting structures on the platform and islands. High-resolution gravimetric studies could help in developing a more robust model of crustal and elastic lithosphere thicknesses. Further consideration of the effects of 3-D (sub-horizontal) mass transport in the lower crust on the pattern of geochemical signatures might also modify interpretations of the latter. Lastly, more investigations are needed to clarify the nature of the extraordinary lava terraces along the SW escarpment, their sources, and related tectonic structures.

2.4.6 On the asymptotic behavior of the flow fronts

In our models, the velocities of both the lower crust particles and the advancing bathymetric front become progressively slower with time. Different histories are found for the two study transects (owing to different initial conditions, parameters and temperature fields), but both evolve toward asymptotic states.

The asymptotic behavior of flow fronts arising in gravity currents is mathematically and experimentally understood for iso-viscous systems, e.g., *Huppert* [1982]. After long times our simulations reach monotonic asymptotic states. For our case with space- and time-dependent viscosity, the crustal velocities are locally proportional to the product $\eta^{-1} h^2 \partial h / \partial x$, where x is the horizontal coordinate of some point, η the viscosity, and h the bathymetric height above it.

The reasons for these systems to acquire asymptotic trends are several:

1. There is a shrinking of the driving forces-affected region, due to horizontal narrowing of the escarpment, therefore a decrease in the volume of the mobile region.
2. The platform becomes more horizontal in time, therefore the deep regions under it (located at the rear of the mobile region) become less mobile (even though their viscosity is almost invariable due to the locally dominant hot perturbation).
3. The off-platform crust viscosities, the highest in the system at all times, increase due to the half-space cooling component there dominant.
(Owing to the continuity equation, conditions (1,2 and 3) already imply a progressive stagnation of the mobile region.)

4. The platform height h decreases in time (at all x), causing a reduction in the driving forces (also below the escarpment).
5. Both the escarpment and the mass below it move away from the hot and weak regions, thus their viscosities increase with time.
6. In the vast majority of our simulations, the escarpment slope increases in time, but finally acquires a constant value.

Mathematically, systems whose velocities trend toward zero can tend to different asymptotes, depending upon how each of these velocities behave asymptotically. They can asymptotically approach a final, bounded displacement, or a monotonically growing, unbounded one. Unfortunately, from our simulations we cannot distinguish between these two cases. Finally, the question is geologically irrelevant: the Galápagos platform will be subducted beneath South-America in a finite amount of time.

2.5 Conclusions

The Galápagos platform, formed perhaps with a larger component of intrusion than extrusion, exhibits several characteristics that suggest flow of its lower crust. We have presented numerical models that include viscous relaxation of the lower crust and exhibit flow-fronts whose geometries resemble the observed present-day bathymetric escarpments in the Galápagos platform.

The conspicuous escarpment along the southwestern margin is formed by a system of stepped terraces that might be explained by lower crustal flow, which would produce backward tilting of the sub-horizontal platform surface thereby hindering the long-distance flow of lavas and potentially producing the stepped morphology. Both the observed present-day morphology and the paleo-geographic reconstructions of *Geist et al.* [2014] rule out the possibility of paleo-sealevels as having an effect here.

The extended escarpment on the eastern platform region may, according to our models, be satisfactorily explained by flow of the lower crust during the last ~3 Myr, producing a well-defined bathymetric front, with the whole system evolving asymptotically towards the present-day configuration. This lower crustal flow episode may be associated with horizontal mass transport: mantle plume geochemical signatures could potentially be advected 50 km towards the southeast, which might be related to the geographically elongated isotopic anomalies found by *Harpp and White* [2001]; and increase the platform's horizontal extension. Both the paleo-bathymetric configuration and the paleo-geographic reconstructions of *Geist et al.* [2014] seem to indicate that paleo-sealevels may also had an effect in the upper parts of the eastern platform.

Similar dynamical regimes may have occurred in the past to the east of the platform, such as the southern escarpment on the Carnegie ridge, and perhaps currently in other smaller, more recent escarpments on the central/western platform.

The phenomenon of lower crustal flow as a mechanism for tectonic deformation, already noted for Iceland by *Jones and Maclennan* [2005] and here inferred to operate in the Galápagos, must be common in hotstpot provinces emplaced upon young oceanic lithosphere [*Richards et al.*, 2013], such as the Azores and Easter islands as well as in aseismic ridges like the Ninety-east and Nazca ridges.

2.6 Acknowledgements

The authors thank Stephen Self, Sally Gibson and Eric Mittelstaedt for their insightful comments, and also thank Karen Harpp and William White for providing material from their 2001 work, as well as Dennis Geist for material from his 2008 work. We thank David Sandwell for directing us to the Scripps (UC San Diego) database (available at http://topex.ucsd.edu/cgi-bin/get_data.cgi.), and Charley Paffenbarger (UC Berkeley) for computational and technical support. We also thank our editor Cin-Ty Lee, reviewer Garret Ito and an anonymous reviewer, for constructive comments on the manuscript. The information used for this paper is properly cited and referred to in the reference list. This work was supported by the US National Science Foundation and CONICYT (Comisión Nacional de Investigación en Ciencia y Tecnología)-Chile.

2.7. Appendix A: Physico-mathematical description

2.7.A.1 Conservation laws

We consider a 2D Stokes fluid with velocity field $v_i = v_i(x, z, t)$, with $i = (1, 2)$ representing x and z components and t the time; subjected to a homogeneous gravitational field $\vec{g} = -g\hat{z}$ (which implicitly defines the orientation of the vertical axis). The relevant conservation laws are:

$v_{i,i} = 0$ Conservation of mass for incompressible fluid (continuity) (A1)

$\sigma_{ij,j} + \rho g_i = 0$ Conservation of linear momentum for Stokes flow (A2)

and

$$\sigma_{ij} = -p\,\delta_{ij} + 2\eta\left[\frac{1}{2}(v_{i,j} + v_{j,i}) - \frac{1}{3}v_{k,k}\,\delta_{ij}\right] + \psi\, v_{k,k}\,\delta_{ij} \quad \text{(A3)}$$

is the general constitutive equation for a Newtonian isotropic fluid with symmetric stress tensor (with shear viscosity η and volume viscosity ψ).

which, using (A1), simplifies to: $\sigma_{ij} = -p\,\delta_{ij} + \eta(v_{i,j} + v_{j,i})$ (A4)

In this formulation, we will allow $\eta = \eta(x, z, t)$

Given the continuity and constitutive equations, the horizontal component of the momentum equation can be written as:

$$0 = -p_{,x} + 2(\eta\, v_{x,x})_{,x} + \left[\eta(v_{x,z} + v_{z,x})\right]_{,z} \quad \text{(A5)}$$

where we have assumed a 2D system, so that all the partial derivatives with respect to the other horizontal component (*y*) vanish.

We use a thin-sheet approximation defined by the two following conditions:

$v_x \gg v_z$ sub-horizontal mass flow

and

$a_{,x} \ll a_{,z}$ where a is any dependent variable of the system, which means that the system has, at all times, horizontally elongated features.

Keeping only dominant terms of the momentum equation (in relation with the thin-sheet approximation), and regarding the pressure gradient as an unknown quantity, we get:

$$0 = -p_{,x} + (\eta\, v_{x,z})_{,z} \quad \text{(A6)}$$

which is an approximate version of the horizontal component of the momentum equation.

We assume a lithostatic pressure field:

$$p(x,z,t)=\rho g\left[h(x,t)-z\right] \tag{A7}$$

with *h(x,t)* being the height of the bathymetry over the isostatic reference level, and *z* the vertical coordinate, positive upwards.

Thus, $p_{,x}=\rho g h_{,x}$ (A8)

and consequently, the momentum equation can be recast as:

$$\left(\eta v_{x,z}\right)_{,z}=\rho g h_{,x} \tag{A9}$$

Integration over the vertical coordinate *z* gives:

$$\eta(x,z,t)v_{x,z}(x,z,t)-\eta(x,z_0,t)v_{x,z}(x,z_0,t)=\int_{z0}^{z}\rho g h_{,x}dz \tag{A10}$$

which, after trivially integrating its right side, we will write in a more generic form:

$$v_{x,z}(x,z,t)=\frac{1}{\eta(x,z,t)}\left[c(x,t)+\rho g h_{,x}z\right] \tag{A11}$$

with $c(x,t)=\eta(x,z_0,t)v_{x,z}(x,z_0,t)-\rho g h_{,x}z_0$

being the “integration constant” for *z*, which is a function of *x* and *t* here. We don't know the vertical gradient of the horizontal velocity at this point, so it is not possible to evaluate this function for now. Instead, we will readily obtain a computable expression for it when evaluating the boundary conditions.

Another integration over the *z* coordinate gives:

$$v_x(x,z,t)=v_x(x,z_0,t)+\int_{z_0}^{z}\frac{1}{\eta(x,z',t)}\left[c(x,t)+\rho g h_{,x}z'\right]dz' \tag{A12}$$

2.7.A.2 Boundary conditions

Upper and lower boundaries are considered horizontally rigid:

$$v_x(x,h,t)=0 \quad \text{and} \quad v_x(x,-f\,h,t)=0 \qquad \text{(A13 and A14)}$$

where $f=\dfrac{\rho_c}{(\rho_m-\rho_c)}$ is a 'crust-mantle' isostatic equilibrium factor, and always with $h=h(x,t)$.

Taking $z_0 = -f\,h$ (isostatic Moho) the condition at the lower boundary yields:

$$v_x(x,z,t)=\int_{-fh}^{z}\frac{1}{\eta(x,z',t)}\left[c(x,t)+\rho g h_{,x} z'\right]dz' \qquad \text{(A15)}$$

and then, the condition at the upper boundary yields:

$$c(x,t)=-\left[\int_{-fh}^{h}\frac{1}{\eta(x,z',t)}dz'\right]^{-1}\cdot\int_{-fh}^{h}\rho g h_{,x}\frac{z'}{\eta(x,z',t)}dz' \qquad \text{(A16)}$$

So, factoring out, finally we can write:

$$v_x(x,z,t)=\rho g h_{,x}\left[\int_{-fh}^{z}\frac{z'}{\eta(x,z',t)}dz'-s(x,t)\int_{-fh}^{z}\frac{1}{\eta(x,z',t)}dz'\right] \qquad \text{(A17)}$$

with $s(x,t)=\dfrac{\displaystyle\int_{-fh}^{h}\frac{z''}{\eta(x,z'',t)}dz''}{\displaystyle\int_{-fh}^{h}\frac{1}{\eta(x,z'',t)}dz''}$

(with z', z'' being auxiliary integration variables with the same scaling and dimensions as z).

We assume zero mass flux at the vertical walls (x=0 and x=L) of the model box, more specifically:

$$v_x(x=0,z,t)=0 \quad \text{and} \quad v_x(x=L,z,t)=0 \qquad \text{(A18 and A19)}$$

for the whole range $-fh\leqslant z\leqslant h$.

2.7.A.3 Temperature and Viscosity structure

The thermal structure consists of two ingredients: (1) A half-space cooling model (with locally defined depth coordinate, i.e., *depth=depth(x,z,t)*, and thermal age being horizontally dependent upon the age gradient *Dt/dx*), and (2) A hot thermal perturbation with Gaussian form in *x* and *z* as described in the main text.

(1) Starting with a definition of homologous temperature ($T_{om} = T / T_{solidus}$) that depends on the solidus thermodynamic conditions, the analytic solution of the temperature vs. depth and time given by the half-space cooling model (with initial temperature $T_{solidus}$ and upper boundary temperature 0° Celsius) is:

$$T_{om} = erf\left(\frac{depth}{2\sqrt{(\kappa t)}}\right) \tag{A20}$$

where the time t=0 corresponds to when the half space was at the solidus temperature, zero thermal age; therefore t can be approximately equated with the age of the background crust (related to its distance to the spreading ridge).

If we adapt this model to a thin-sheet system, in which the bathymetric surface is sub-horizontal, we can take

$$depth(x,z,t) = h(x,t) - z \tag{A21}$$

and follow up with the aforementioned solution, with negligible error regarding the flatness of the bathymetry. This is exactly the same description adopted by *Jones and Maclennan* [2005].

If in addition, in this study we consider the crust as having a differential age progression along the horizontal, in such a way that we can define a gradient in crustal age, $Age_{grad} = d(Age) / dx$, provided that we know the location of the study transect. Here, this gradient is assumed constant and applied along the full transect length.

With these ingredients, a modified and approximate version of the half-space cooling temperature solution can be adopted:

$$T_{om}^{HSC}(x,z,t) = erf\left\{\frac{h(x,t) - z}{2\sqrt{[\kappa(t + Age_{grad}\, x)]}}\right\} \tag{A22}$$

(2) In addition to the previous description, given the evidence of diapirism and volcanism throughout the Galápagos platform and with it being sustained in geologic time, it is likely that not only a high vertical geothermal gradient is present, but also that a high-temperature region extends from the Moho and up to shallow depths in the central platform area under the volcanoes, which creates a horizontal thermal gradient component relative to the cold off-platform background crust. Consequently, we have imposed a hot thermal perturbation in trying to mimic this geologic scenario in a simple way. The perturbation is taken to be a bi-dimensional, unit-amplitude Gaussian function (with horizontal and vertical length scales L_{Tx} and L_{Tz}

respectively). A Gaussian function was preferred because it represents the kernel of the diffusion equation.

$$T_{om}^{hot}(x,z,t)=\exp[-(\frac{x}{L_{Tx}})^2+\left\{\frac{[f\,h(0,t)+z]}{[L_{Tz}\,f\,h(0,t)]}\right\}^2] \quad \text{(A23)}$$

Which is a Gaussian function centered on the platform side of the model box (x=0) and at the time-dependent Moho depth ($z(t) = - f\,h(0,t)$). This definition implies the vertical advection of the perturbation.

The vertical length scale value L_{Tz} is chosen to produce acceptable surface values of the viscosity (considered volumetric averages over length scales given by the grid size). On the other hand, the value of L_{Tx} determines how horizontally extended the weak area under the central platform is, and is considered a model parameter to be investigated.

This hot thermal perturbation, taken to be homologous, is added to the temperature function previously defined.

$$T_{om} = T_{om}^{HSC}+T_{om}^{hot} \quad \text{(A24)}$$

Homologous temperatures greater than one are obtained in the vicinity of the hot thermal perturbation's center, which implies that the system has, on volumetric local averages (over grid-point-centered domains with grid spacing side-lengths), a fraction of partial melting.

Using a thermal diffusivity of $\kappa=10^{-6}m^2/s$, and after transforming temperature units (Celsius to Kelvin), the viscosity is computed as a function of the homologous temperature:

$$\eta=\eta_{solidus}\,e^{[(a/T_{om})-a]} \quad \text{(A25)}$$

with $T_{om}=T_{om}(x,z,t)$ and where a nominal value $a=40$ was adopted from *Jones and Maclennan* [2005].

Finally, in consideration of homologous temperatures greater than unity and with the overall behavior of the exponential equation for viscosity, some restrictions are applied: a lower bound on the viscosity value is imposed following geological constraints that render the exponential formula inaccurate when the viscosity is well below the solidus viscosity due to partial melting. For example, viscosities lower than one tenth of the solidus viscosity (here assumed close to 10^{18} Pa·s) are not allowed. Similarly, a viscosity upper bound is imposed with regard to constraints on tectonic processes, from which it is understood that the real macroscopic viscosity values are not well represented by the expression for viscosity we are using. For instance, maximum viscosities greater than 10^{23} Pa·s are not considered. This approach is in agreement with *Jones and Maclennan* [2005].

$\eta_{min}\leqslant\eta\leqslant\eta_{max}$ with these bounds being among the parameters investigated in this study.

2.7.A.4 Governing equations

As we see from the equation for velocity, the controlling variable is the bathy/topo -graphic height *h(x,t)*, so we need an equation for it:

The mass conservation equation (A1) allows us to write:

$$v_{z,z} = -v_{x,x} \quad \text{thus} \quad \int_{z1}^{z2} v_{z,z}\,dz = -\int_{z1}^{z2} v_{x,x}\,dz$$

so that

$$v_z(x,z_2,t) - v_z(x,z_1,t) = \int_{z1}^{z2} v_{z,z}\,dz = -\int_{z1}^{z2} v_{x,x}\,dz \qquad \text{(A26)}$$

Now, choosing $z_1 = -f\,h(x,t)$ (isostatic Moho), and $z_2 = h(x,t)$ (bathymetry)

then $v_z(x,z_1,t) = -f\,\dot{h}(x,t)$ and $v_z(x,z_2,t) = \dot{h}(x,t)$ (A27 and A28)

(where the upper dot represents the partial derivative with respect to time).

Thus, equation (A26) can be written as:

$$v_z(x,h,t) - v_z(x,-fh,t) = -\int_{-fh}^{h} v_{x,x}\,dz \qquad \text{(A29)}$$

The boundary conditions (A13) and (A14) allow the partial derivative with respect to *x* inside the integral in (A29) to be taken outside of it, and then considering (A27) and (A28), equation (A29) yields:

$$\dot{h}(x,t) + f\,\dot{h}(x,t) = -\left(\int_{-fh}^{h} v_x\,dz\right)_{,x} \quad => \quad \dot{h}(x,t) = \frac{-1}{1+f}\left(\int_{-fh}^{h} v_x\,dz\right)_{,x}$$

which can be finally written in a more extended and explicit form:

$$\frac{\partial h(x,t)}{\partial t} = \frac{-1}{1+f}\frac{\partial}{\partial x}\left(\int_{-fh(x,t)}^{h(x,t)} v_x(x,z,t)\,dz\right) \qquad \text{(A30)}$$

This equation means that any material column in the crust changes its total vertical length ($(1+f)\cdot h(x,t)$) in time according to the net volume flux across its boundaries. This is a direct consequence of mass conservation.

The numerical solution of the two governing equations ((A17) and (A30)) is carried out in a non-dimensional form with the following reference scales:

Length: L (the horizontal length of the model box, here being equal to 350 km for both study transects); defining a scale for x.

System aspect ratio (vertical over horizontal): c = { [6 [km]/(1+f)] + H_{plat} }/L ; defining a scale for $z = cL \cdot z'$

with [6 [km] / (1+f)] being the elevation of the upper surface of a 6 km-thick (oceanic) crust over the isostatic reference level in compensation with the mantle, and H_{plat} being the initial platform maximum thickness.

Viscosity: a mean value η_{ave} is used to scale with the overall system behavior. To estimate the right value using a simple algorithm before run, is difficult due to the strong spatial variability of the viscosity. We have instead, estimated it by trial and error, with the objective of fitting the model timescales, which are mainly controlled by the low-viscosity mobile regions.

For example, a useful expression is: $\eta_{ave} = \left(\eta_{min}^{a} \eta_{sol}^{b} \eta_{max}^{c}\right)^{1/(a+b+c)}$ (which is a power-weighted geometric mean of the system reference viscosities) where $a > b > c$ (an example being $a = 8, b = 5, c = 1$).

Mass-density and gravity are referenced to $\rho_c = 2.8\, gr/cm^3$ and $g = 9.8\, m/s^2$, respectively.

With these quantities, a natural scale for velocity can be obtained from the final equation for the horizontal velocity component (equation (A17)):

$$V_0 = \rho_c g c^3 L^2 / \eta_{ave}$$

and with it, a possible time scale can be found: $\tau = L/V_0$ so that $\tau = \dfrac{\eta_{ave}}{\rho_c g c^3 L}$

In the code, a further constraint is applied on τ to obtain desired times scales.

In these last two expressions, we note their dependence on the driving force, the aspect ratio, the absolute size of the system, and the average viscosity.

With these characteristic scales, the governing equations (in non-dimensional form) to be considered are:

$$\frac{\partial h'(x',t')}{\partial t'} = -\left(\frac{V_0\, \tau}{(1+f)L}\right) \frac{\partial}{\partial x'} \left(\int_{-fh'(x',t')}^{h'(x',t')} v'_x(x',z',t')\, dz' \right) \qquad \text{(A31)}$$

$$v'_x(x',z',t') = \rho' g' h'_{,x'} \left[\int_{-fh'}^{z'} \frac{\tilde{z}}{\eta'(x',\tilde{z},t')} d\tilde{z} \; - s(x',t') \int_{-fh'}^{z'} \frac{1}{\eta'(x',\tilde{z},t')} d\tilde{z}' \right] \qquad \text{(A32)}$$

with $s(x',t') = \dfrac{\displaystyle\int_{-fh'}^{h'} \frac{\breve{z}}{\eta'(x',\breve{z},t')} d\breve{z}}{\displaystyle\int_{-fh'}^{h'} \frac{1}{\eta'(x',\breve{z},t')} d\breve{z}}$

in which $\{x', h', z', \tilde{z}, \breve{z}, t', v'_x, \eta', \rho', g'\}$ are dimensionless quantities referenced to the aforementioned scales.

It is worth mentioning that these two governing equations are coupled partial differential equations that depend on integrals over the vertical coordinate. The only horizontal derivatives are for vertically-integrated quantities. This particular feature allows for a rather simple grid definition and a rather easy numerical solution.

2.7. Appendix B: Numerical treatment

2.7.B.1 Numerical solution: Finite differences in space and time.

The integrals over the vertical coordinate, both in equation (A32) when calculating v_x and in equation (A31) when calculating the integral of v_x over depth (volume flux), are computed using Simpson's rule for quadrature. This method uses quadratic polynomials every 3 points to approximate the unknown function and integrate it. It is a good compromise between accuracy and simplicity. At the initial point of quadrature (first point above the Moho), trapezoidal integration with one tenth of grid spacing was used (avoiding lower order method contamination).

For the partial derivative of the volume flux with respect to x, a classical two-point, centered (regarding the equation symmetry) derivative is used.

For time integration of equation (A31) we have used the explicit Runge-Kutta 2, also known as 'improved Euler method'. This scheme is, theoretically, second order accuracy.

Therefore when solving equation (A31), updating the height $h(x,t)$ implies updating the isostatic Moho as well; consequently, the space grid adapts to the time-changing geometry of the crust at each time step. The horizontal coordinates of the grid points are kept fixed for all times and they consist of an equally spaced set of points. For instance, in the non-dimensional space, the grid spacing is $dx = 1/(nx\text{-}1)$ at all times, with nx being the total number of points on the horizontal (a constant in the program). The vertical coordinates of the grid points change with time and they also depend on x. They are defined as an equally spaced set of points over each column length vertical interval $(1+f)\cdot h(x,t)$ in such a way that we define a matrix for the z coordinates as:

$$z_{ij}(t) = -f\,h(x_j,t) + i\cdot dz \qquad \text{(B1)}$$

where i is the index that sweeps over the vertical, j over the horizontal, and dz is the vertical increment.

This grid, being extremely simple, can handle the calculation of the velocity field (equation (A32)) at each grid point at each time, because even though it is inhomogeneous and time-dependent, it constitutes a well-defined Eulerian frame. The upper and lower mesh boundaries are the actual position of the bathymetric surface and the Moho respectively.

2.7.B.2 Numerical instabilities' treatment

When needed, a symmetric, weighted, three-point, moving average stability filter was selectively applied to *h(x,t)* over *x*, with the aim of damping spurious oscillations arising at some time steps, in some particular simulations. The filter is applied only at some time steps, under the criterion of an 'instability threshold trigger' given by slope contrasts every 3 spatially adjacent samples of the bathymetry.

The filter code's name is 'smoother_3w' , and its equation is:

$$sh_j = 0.5(1-w)h_{j-1} + w\,h_j + 0.5(1-w)h_{j+1} \qquad \text{(B2)}$$

where the index *j* refers to the *x* coordinate, *h* being the input height function and *sh* the output smoothed height function.

The filter was investigated exhaustively, and the desired performance was given by a low threshold trigger (adjacent segments' slope changes of 50% to 80%), but acting with a tiny amount of damping: typical values of w=0.99995 or higher were employed. The filter's effect is subtle, and only intended to suppress small, unphysical oscillations and not the desired features of the bathymetry and velocity field. Keeping the bathymetric flow front displacement virtually undamped was among the controlling criteria in choosing filter parameters.

The filter was needed and applied occasionally in the preparation of animated plots on those simulations with a rather extended hot thermal perturbation (large L_{Tx}) in which, due to the overall mechanical weakness of the system, large velocities and deformations are produced. For instance, the filter was not needed when extracting topographic functions (slopes, tilting rates, etc.) for analysis.

2.7.B.3 Benchmarking

Huppert [1982] provides an analytic solution for a gravity current over a horizontal surface, but at the same time sets the essential principles from which *McKenzie et al.* [2000] derive a more general partial differential equation for mass redistribution in a constant-viscosity thin fluid layer of variable-thickness (based on the Stokes equation). We have considered this equation and implemented its solution numerically, for the case of horizontally rigid upper and lower boundaries. This equation is much simpler because it is derived from an analytic expression for the velocity (a parabolic profile), and it reads:

$$\dot{h} = \frac{(1+f)^2 \rho_c g}{12\,\eta_c} \left(h^3 h_{,x}\right)_{,x} \qquad \text{(B3)}$$

(upper dot being time derivative, Einstein notation in space)

The next plots compare numerical solutions of this relatively simple equation, with outputs from our main code (using numerical solution of full integrals applied on the space- and time-

dependent viscosity formulation) but now simply set up for a constant viscosity. Two different cases are shown in Figure 2.B1:

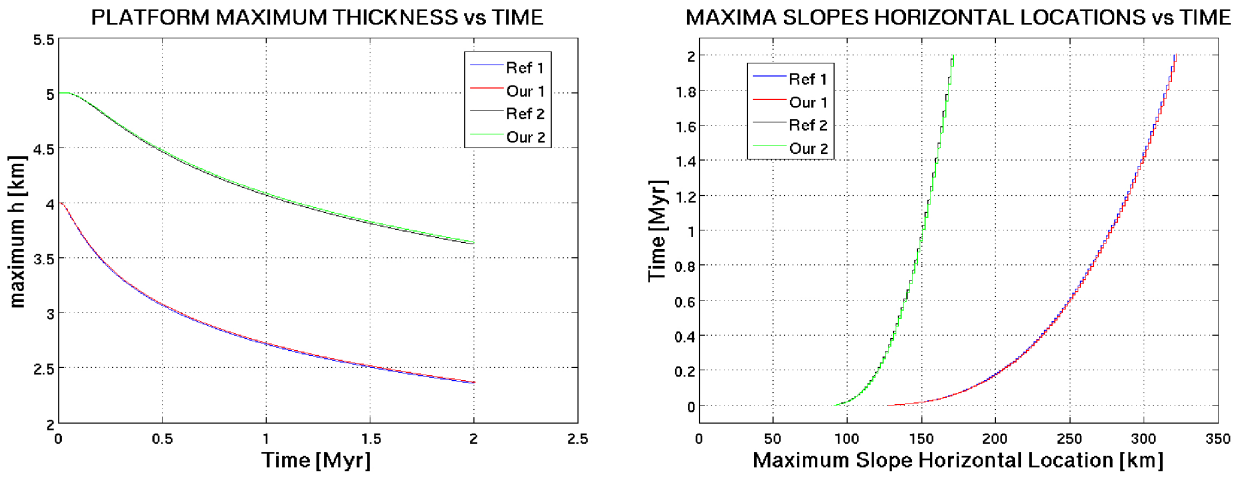

Figure 2.B1. Comparison of the reference solution given by equations in *McKenzie et al.* [2000], with the solution given by our code when set up for constant viscosity.

Case 1: $Visc=10^{19}$ Pa·s, $H_{plat}=4$ km, $x_0=0.35$, $N_{steep}=8$, $L=350$ km

Case 2: $Visc=10^{20}$ Pa·s, $H_{plat}=5$ km, $x_0=0.25$, $N_{steep}=12$, $L=350$ km

Note: The 'platform maximum thickness' is the space-maximum value of the platform thickness (the platform considered as built over the background crust), always found at $x=0$, and evolving in time. This quantity is slightly different from the bathymetry elevation (function of x and t), which is simply the platform thickness (function of x and t) plus the isostatically-defined constant fraction of the background crust, as explained in the methods section. This note applies to all the subsequent figures.

2.7. Appendix C: Sensitivity Analysis

The purpose of this section is to illustrate some features of the model's behavior, more specifically, to show the effect of the controlling parameters. The system's behavior is determined by the initial condition of the bathymetry, the boundary conditions and the viscosity structure parameters. The boundary conditions were described previously, and their effects will not be investigated further here.

2.7.C.1 Initial condition of Bathymetry

The initial bathymetric function controls the system evolution to some degree. As was explained in the methodology section, the initial bathymetry is described by a Butterworth filter equation. We prescribed the horizontal length scale as $x_0 = 0.35 \cdot L$ a priori as a reasonable value for our purposes. We have chosen the initial platform thickness $H_{platform}$ with regards to geological criteria particular to each study transect.

In the following, model sensitivity will be shown in the vicinity of one of our model simulations, the one associated with the Eastern platform. The value of initial platform thickness is set to $H_{platform} = 2$ km (overlying a background 6 km-thick oceanic crust).

An important parameter in this function is the exponent 'N_{steep}' that controls how steep and wide the initial bathymetry ramp is.

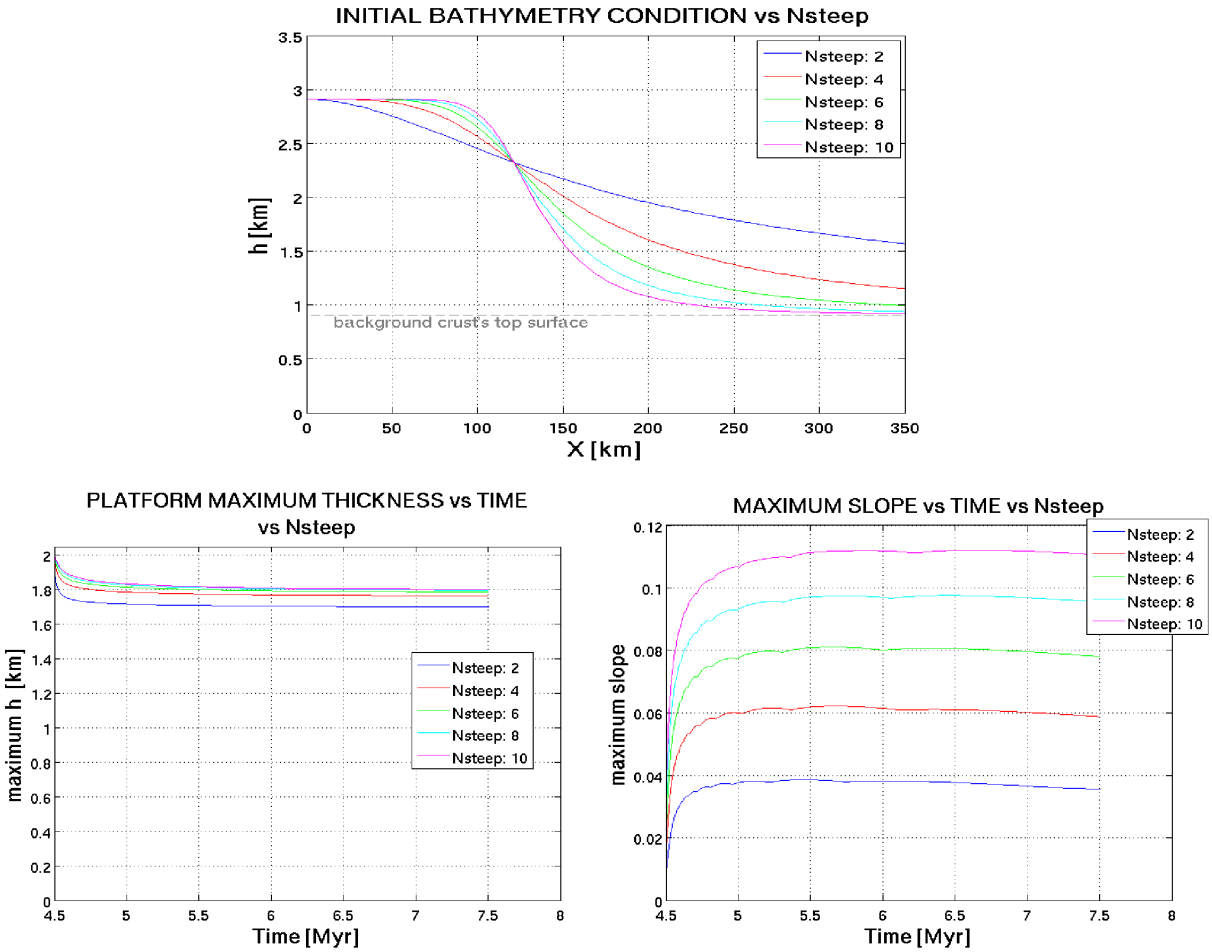

Figure 2.C1. Above: Different initial bathymetry profiles vs. the slope exponent 'N_{steep}' (determining the escarpment steepness and width). Below: Model sensitivity to the exponent 'N_{steep}', here shown for two model output variables: the platform maximum thickness vs. time, and the escarpment's maximum slope vs. time.

2.7.C.2 Definition of the viscosity structure

Following the methodology section, the viscosity structure is defined by the following geometrical, thermal and rheological parameters:

1. Horizontal Length scale of the Gaussian hot thermal perturbation (provided that the vertical length scale was fixed a priori), defining how extended the weak region is inside the system.

2. Initial age of the background crust, here taken as the reference initial age at x=0 (central platform area), from which the horizontal age gradient defines the initial ages over the system for $0<x\leqslant L$.

3. Scaling of viscosity reference values: solidus viscosity, minimum viscosity, maximum viscosity.

For example, variations in the values of the maximum viscosity have little effect on the system's behavior, therefore will not be shown here.

As can be seen in Figure 2.C1, the index N_{steep} determines the initial steepness of the bathymetric ramp and also the horizontal extension of it. For the combination of parameters defining this model (the location in the parameter space), the effect of N_{steep} is not important over the platform thickness over time. Nevertheless, its effect over the spatial maximum platform slope is significant. As can be seen, the ordering relation of the slope values is conserved, higher initial slopes remaining higher over time. The slope increase is due to the development of a flow front. The time scale is related to the relevant geologic time for the Eastern platform evolution (last 3 Myr). The time is referred to the reference thermal age of the background oceanic crust under the central platform which (not considering thermal rejuvenation due to volcanism in the platform) nowadays is roughly 7.5 Myr (between the 5 Myr and 10 Myr isochrons). This time definition will apply to all of the items of this section.

Figure 2.C2 shows the effect of different values of the horizontal length scale of the hot-thermal perturbation have on the spatial maximum slope (left) and the horizontal position of the points where that maximum slope is reached (recall that the horizontal position of the material points over the bathymetric surface is fixed for all times due to the applied boundary condition). Larger values of the thermal length scale L_{Tx} are expressed as larger extensions of the mechanically weak zone, and are therefore associated with larger deformation volumes and enhanced mobility, producing greater front slopes and larger front displacements.

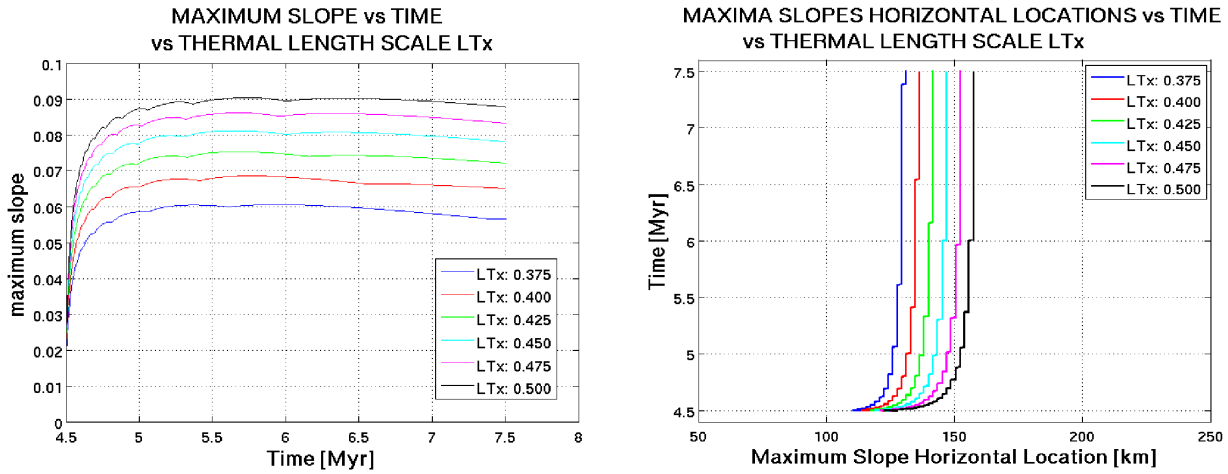

Figure 2.C2. Model sensitivity to the hot thermal perturbation's horizontal length scale 'L_{Tx}', here shown for two model output variables: the escarpment's spatial maximum slope vs. time, and the escarpment's maximum slope locations vs. time.

In Figure 2.C3, model sensitivity to the initial reference age of the background oceanic crust is shown for the maximum platform-thickness vs. time (left) and the position of the bathymetric flow-front (left). The effect of this parameter is not so important on this region of the parameter space, due to: (i) relatively old initial ages > 4.0 Myr, and (ii) the presence of a hot-thermal perturbation that controls the system's evolution to a greater degree. Nevertheless, the different systems evolve to different final asymptotes.

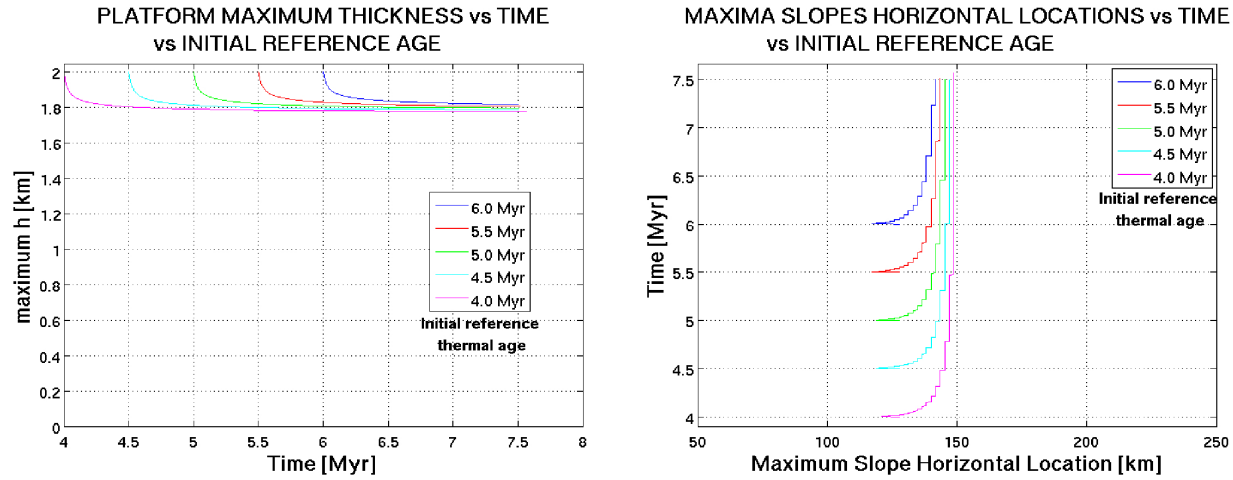

Figure 2.C3. Model sensitivity to the background crust's initial reference age (including the horizontal gradient in age), here shown for two model output variables: the platform maximum thickness vs. time, and the escarpment's maximum slope locations vs. time.

Figure 2.C4 illustrates the effect of the simultaneous amplification of the three viscosity reference values (minimum, solidus, maximum) by a constant factor (0.25,0.5,1,2,4,10), observed over the spatial maximum platform-thickness and the horizontal position of the maximum slope, vs. time. At earlier times (roughly 4.5 to 5.0 Myr) the systems' evolution time scales seem to be proportional to their viscosity reference values (as predicted by linear theory for time-independent viscosity Stokes fluids). At later times, the proportionality is explicitly broken: higher viscosity systems (a = 4 , 10) evolve more slowly in time, and they take longer (than proportional) to reach the same values of 'maximum thickness *h*' than lower viscosity systems (a = 0.25 , 0.5). This behavior is due to the time-dependent nature of the viscosity of the systems here considered: the thermal cooling due to aging imposes a natural and independent clock that produces higher viscosities at later times, therefore increasing the space-average viscosities in time, say, for corresponding time intervals with lengths proportional to the reference viscosity values (minimum, solidus, maximum).

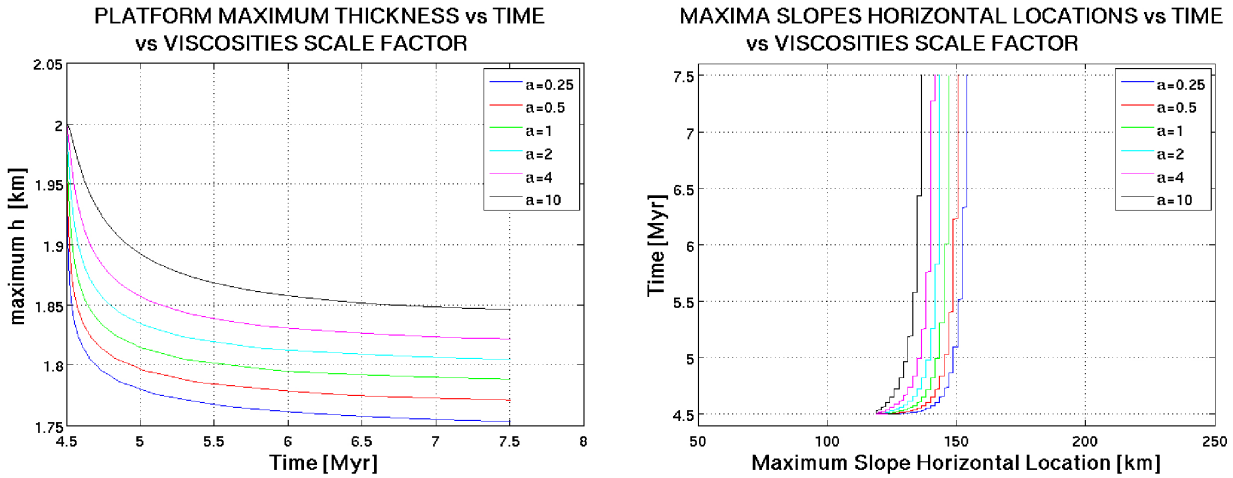

Figure 2.C4. Model sensitivity to the simultaneous scaling of the three viscosity reference values (minimum, solidus, maximum), here shown for two model output variables. Here, 'a' is the scale factor for the viscosities. Note that the scale for the maximum thickness '*h*' starts at 1.75 km, so the relative difference among the curves is small.

From the inspection of the sensitivity analysis and of all the simulations performed, we learn that high-viscosity systems (for example a = 4 , 10) not only evolve slower in time relatively to low-viscosity systems (for example a = 0.25 , 0.5), but also that high-viscosity systems finally do not reach the same states as low-viscosity systems. The systems considered in this study show asymptotic behavior, yet at long time scales, high-viscosity systems evolve to different asymptotes and tend to "freeze" in different final states than low viscosity systems.

2.8 References

Christie, D., R. Duncan, A. McBirney, M. Richards, W. White, K. Harpp, and C. Fox (1992), Drowned islands downstream from the Galápagos hotspot imply extended speciation times, *Nature*, v.355, 246-248.

Christie, D., R. Werner, F. Hauff, K. Hoernle, and B. Hanan (2005), Morphological and geochemical variations along the eastern Galápagos Spreading Center, *Geochem. Geophys. Geosys.*, v.6, 1, Q01006.

Contreras-Reyes, E., and D. Carrizo (2011), Control of high oceanic features and subduction channel on earthquake ruptures along the Chile-Peru subduction zone, *Phys. Earth Planet. Int.*, 186, 49-58, doi:10.1016/j.pepi.2011.03.002.

Cuffaro, M., and C. Doglioni (2007), Global kinematics in deep versus shallow hotspot reference frames, *The Geological Society of America*, special paper v. 430, 359-374.

Deschamps, A., C. Grigne, M. Le Saout, S.A. Soule, P. Allemand, B. Van Vliet Lano, and F. Floch. (2014), Morphology and dynamics of inflated subaqueous basaltic lava flows, *Geochem. Geophys. Geosys.*, v.15, 6, doi: 10.1002/2014GC005274.

Detrick, R., J. Sinton, G. Ito, J. Canales, M. Behn, T. Blacic, B. Cushman, J. Dixon, D. Graham, and J. Mahoney (2002), Correlated geophysical, geochemical, and volcanological manifestations of plume-ridge interaction along the Galápagos Spreading Center, *Geochem. Geophys. Geosys.*, v.3, 10, 8501.

Farnetani, C., A.W. Hofmann, C. Class (2012), How double volcanic chains sample geochemical anomalies from the lowermost mantle, *Earth Planet. Sci. Lett.* 359-360, 240–247.

Feighner, M., and M.A. Richards (1994), Lithospheric structure and compensation mechanisms of the Galápagos Archipelago, *J. Geophys. Res.*, 99, 6711-6729.

Feighner, M., and M.A. Richards (1995), The fluid dynamics of plume-ridge and plume-plate interactions: An experimental investigation, *Earth and Planetary Sc. Lett.*, 129, 171-182.

Geist, D., B. Diefenbach, D. Fornari, M. Kurz, K. Harpp, and J. Blusztajn (2008), Construction of the Galápagos platform by large submarine volcanic terraces, *Geochem. Geophys. Geosys.*, v.9, 3, Q03015.

Geist, D., W. White, and A. McBirney (1988), Plume-asthenosphere mixing beneath the Galápagos archipelago, *Nature*, v.333, 657-660.

Geist, D. J., H. Snell, H. Snell, C. Goddard, and M. Kurz (2014), A Paleogeographic Model of the Galápagos Islands and Biogeographical and Evolutionary Implications, in *The Galápagos: A Natural Laboratory for the Earth Sciences* (eds K. S. Harpp, E. Mittelstaedt, N. d'Ozouville and D. W. Graham), John Wiley & Sons, Inc, Hoboken, New Jersey, doi: 10.1002/9781118852538.ch8.

Gibson, S. A. and D. Geist (2010), Geochemical and geophysical mapping of lithospheric thickness variations beneath Galápagos. *Earth and Planetary Sc. Lett.*, 300 (3-4). 275-288, doi: 10.1016/j.epsl.2010.10.002.

Gibson, S. A. and Geist, D. and Richards, M.A. (2015) Mantle plume capture anchoring and outflow during Galápagos plume-ridge interaction. *Geochem. Geophys. Geosys.*, 16 (5). n/a-n/a. ISSN 15252027.

Harpp, K., and W. White (2001), Tracing a mantle plume: Isotopic and trace element variations of Galápagos seamounts, *Geochem. Geophys. Geosys.*, v.2, 6, 1042.

Hey, R. (2010), Galápagos Tectonics and Evolution, Eos Trans. AGU, 91, Fall Meet. Suppl., V52A-01.

Hey, R., K. Deffeys, L. Johnson, and A. Lowrie (1972), The Galápagos triple junction and plate motions in the East Pacific, *Nature*, v. 237, 20-22.

Hey, R., and P. Vogt (1977), Spreading center jumps and sub-axial asthenosphere flow near the Galápagos hotspot, *Tectonophysics, 37*, 41-52.

Hirth, G., and D. Kohlstedt (1996), Water in the oceanic upper mantle: implications for rheology, melt extraction and the evolution of the lithosphere. *Earth and Planetary Sc. Lett.* 144 (1), 93-108.

Hoernle, K. A., R. Werner, J. P. Morgan, D. Garbe-Schonberg, J. Bryce, and J. Mrazek (2000), Existence of complex spatial zonation in the Galápagos plume for at least 14 m. y., *Geology*, 28 (5), 435 – 438.

Hooft, E., B. Bryndis, D. Toomey, R. Detrick, R. Mjelde, S. Solomon, H. Shimamura, and Y. Murai (2010), Seismic Constraints on the Formation of the Galápagos and Iceland Platforms, AGU 2010 abstract.

Huppert, H. (1982), The propagation of two-dimensional and axisymmetric viscous gravity currents over a rigid horizontal surface, *J. Fluid Mech.*, v.121, 43-58.

Ito, G., and T. Bianco (2014), Patterns in Galápagos magmatism arising from the upper mantle dynamics of plume-ridge interaction, in *The Galápagos as a Laboratory for the Earth Sciences*, edited by K. S. Harpp, et al., Chapter 13, *Geophys. Monogr*., 204, Amer. Geophys. Union, Washington D. C.

Ito, G., J. Lin, and C. W. Gable (1997), Interaction of mantle plumes and migrating mid-ocean ridges: Implications for the Galápagos plume-ridge system, *J. Geophys. Res.*, v.102, B7, 15,403–15,417, doi:10.1029/97JB01049.

Jones, S., and J. Maclennan (2005), Crustal flow beneath Iceland, *J. Geophys. Res*., v.110, B09410, doi:10.1029/2004JB003592.

Keller, T., D. May and B. Kaus (2013), Numerical modeling of magma dynamics coupled to tectonic deformation of lithosphere and crust, *Geophys. J. Int.*, 195, 1406-1442.

Mackwell, S. J., M. Zimmerman, and D. Kohlstedt (1998), High-temperature deformation of dry diabase with applications to tectonics on Venus, *J. Geophys. Res.*, v.103, 975 – 984.

Mark, R. K., and J. G. Moore (1987), Slopes of the Hawaiian ridges, U.S. Geo. Surv. Prof. Paper 1350, 101-107, U.S. Government Printing Office, Washington.

McKenzie, D., F. Nimmo, J. Jackson, P. Gans, and E. Miller (2000), Characteristics and consequences of flow in the lower crust, *J. Geophys. Res*., v.105, B5, 11029-11046.

Mittelstaedt, E., S. Soule, K. Harpp, D. Fornari, C. McKee, M. Tivey, D. Geist, M. Kurz, C. Sinton, and C. Mello (2012), Multiple expressions of plume-ridge interaction in the Galápagos: Volcanic lineaments and ridge jumps, *Geochem. Geophys. Geosys.*, v.13, 5, Q05018.

Moore, J. G. (1987), Subsidence of the Hawaiian ridge, U.S. Geo. Surv. Prof. Paper 1350, 85-100, U.S. Government Printing Office, Washington.

Morgan, W., and J. Morgan (2007), Plate velocities in the hotspot reference frame, *The Geological Society of America*, special paper v. 430, 65-78.

Naumann, T., D. Geist, and M. Kurz (2002), Petrology and Geochemistry of the volcan Cerro Azul: petrologic diversity among the western Galápagos volcanoes, *Journal of Petrology* (Oxford University Press) 43 (5): 859–883.

Richards, M., E. Contreras-Reyes, C. Lithgow-Bertelloni, M. Ghiorso, and L. Stixrude (2013), Petrological interpretation of deep crustal intrusive bodies beneath oceanic hotspot provinces: *Geochem. Geophys. Geosys.*, v.14, 3, 604–619.

Richards, M., and R. Griffiths (1989), Thermal entrainment by deflected mantle plumes, *Nature*, v.342, 21/28, 900-902.

Sallares, V., P. Charvis, E. Flueh, J. Bialas, and the Salieri scientific party (2005), Seismic structure of the Carnegie ridge and the nature of the Galápagos hotspot, *Geophys. J. Int.*, 161, 763-788, doi: 10.1111/j.1365-246X.2005.02592.x

Sallares, V., Ph. Charvis, E. Flueh, and J. Bialas (2003), Seismic structure of Cocos and Malpelo Volcanic Ridges and implications for hot spot-ridge interaction, *J. Geophys. Res*., v.108, B12, doi:10.1029/2003JB002431.

Umino, S. (2012), Emplacement mechanism of off-axis large submarine lava field from the Oman ophiolite, *J. Geophys. Res.*, v.117, B11210, doi:10.1029/2012JB009198.

Villagomez, D., D. Toomey, D. Geist, E. Hooft, and S. Solomon (2014), Mantle flow and multistage melting beneath the Galápagos hotspot revealed by seismic imaging, *Nature*, 7, 151-156, doi:10.1038/NGEO2062.

Villagomez, D., D. Toomey, E. Hooft, and S. Solomon (2011), Crustal structure beneath the Galápagos Archipelago from ambient noise tomography and its implications for plume-lithosphere interactions, *J. Geophys. Res.*, v.116, B04310, doi:10.1029/2010JB007764.

Werner, R., K. Hoernle, U. Barckhausen, and F. Hauff (2003), Geodynamic evolution of the Galápagos hotspot system (Central East Pacific) over the past 20 m.y.: Constraints from morphology, geochemistry, and magnetic anomalies, *Geochem. Geophys. Geosys.*, v.4, 12, 1108.

White, W. M., A.R. McBirney, and R.A. Duncan (1993), Petrology and geochemistry of the Galápagos Islands: Portrait of a pathological mantle plume. *J. Geophys. Res.*, v.98, B11, 19,533–19,563, doi:10.1029/93JB02018.

Chapter 3

Island emergence/subsidence histories and their bearing upon biological speciation in the Galápagos

by
Felipe Orellana Rovirosa and Mark Richards

Chapter Abstract

In the context of plate motion reconstructions for the Nazca, Cocos and South American plates in relation with the Galápagos hotspot, it is found that the age-depth dependence of bathymetry, dynamic topography due to the Galápagos plume, crustal relaxation, and magmatic production allow for us to estimate the subsidence of islands and seamounts along the Carnegie Ridge. Our estimates are partially based on geodynamic theory (fluid mechanics and elasticity), but also on detailed bathymetric observations and analysis. For the Carnegie Ridge saddle, we estimate subsidence of about ~2 km occurring during the past ~13 Ma. Because the present-day depths of the region are in the range 2-2.5 km, this assessment shows that the deepest region of the present-day Carnegie Ridge may have been above sea level when it was closer to the active hotspot, therefore providing habitat for land species for a few (<5) million years. Moreover, the migrating hotspot swell may have caused the emerging of different portions of the Carnegie Ridge on a spatio-temporal progression. A more sophisticated 3D numerical model including an asthenosphere and plume interacting with the overlying Nazca plate may provide an improved understanding of geological-biological co-evolution in the Galápagos-Carnegie Ridge.

3.1 Introduction

In 1831, 22-year-old Charles Darwin embarked upon an historic expedition of discovery, circumnavigating the world in a small British survey vessel *HMS Beagle*. In 1835, after departing from extensive explorations in South America, he arrived in the Galápagos archipelago, where he remained for only about four weeks. However, his observations there, and his deeply inquisitive spirit, led him to undertake a a life-long study of the underlying causes of evolution and biological species diversity. Almost 25 years later, he published *On the Origin of Species*, the seminal book in evolutionary biology, and one of the most important intellectual accomplishments in human history. Darwin's theory of natural selection as the primary mechanism of evolution explains that the species characteristics (genotype and phenotype) are long-term products of the interaction of individuals with the environment they inhabit.

Darwin's acumen as a trained geologist led him to recognize that the geographic isolation and geological youth of the Galápagos provided a unique natural laboratory for pitting creationist ideas against more modern notions of evolution. In particular, he recognized that most of the islands peculiar assortment of fauna must have originated in nearby South America, but evolved from the original colonists. Nowadays, the Galápagos still serve as the archetypal natural laboratory for studying the evolution of species inhabiting new and isolated landscapes, with classical studies of famous and unique species of Darwin's finches, iguanas, and tortoises, as well as many other groups, including over 120 endemic species of land snails (*Parent et al.* [2008]. This treasure-trove of phylogenetic information reflects, and constrains the emergence and subsidence histories of the volcanic Galápagos Islands, with global implications for evolutionary biology. However, geophysical studies of controls on these emergence/subsidence histories are few. This chapter seeks to bring new geodynamic perspectives to constraining these histories, and, ultimately, applying them to evolutionary studies.

Some of the answers to these questions, are likely to be found in Earth sciences. For example in recent work, *Ali and Aitchinson* [2014] showed that eustatic sealevel changes must have played a crucial role in shaping the habitat of several Galápagos species during the last 0.7 Ma. As a case study, iguanas are at the center of our attention. Although land iguanas are found in many locations, including Central and South America as well as Galápagos, the endemic Galápagos marine iguanas are a are unique to the Galápagos. Genetic studies on marine iguanas suggest that the marine iguanas diverged from land species undoubtely more than 10 Ma ago *Parent et al.* [2008]. This age is paradoxical when considering that the oldest rocks dated in the islands (Santa Fe, San Cristobal, Española) are ~3 Ma, and the oldest rocks dated on the Carnegie Ridge (west of the saddle point) are ~9 Ma (*Christie et al.* [1992], *Kurz and Geist* [1999], *Geist et al.* [2014]). These creatures are nowhere else to be found. Despite being good swimmers, they are not fish, and they rely on the coastal terrestrial environment to rest, nest, etc. Thus some coastal habitat, geographically not evident at the present day, must have existed for them somewhere, in the geologic past, presumably along the now-submerged eastern extension of the Galápagos hotspot track.
The study of *Geist et al.* [2014] shows how during the last ~5 Ma the archipelago's geography changed, likely experiencing variations in the number of islands, the islands' areal extent, and

their connectivity (or geographical interconnectedness), etc. These geometric-geographic variations had direct effects on vicariance and therefore conditioned how the species diversified and how the populations evolved throughout time. One of *Geist et al.'s* [2014] main conclusions is: "*The use of the present-day map of the Galápagos to deduce biological processes that take 10^5 to 10^6 yrs. will yield incorrect results*", and "*For any model for dispersal, colonization, speciation, and radiation that involves island geography more than 20,000 years ago, the current map of the Galápagos Islands is completely irrelevant*".

Making use of the present-day topography-bathymetry of the Galápagos archipelago region, *Geist et al*. [2014] estimated paleo-elevations via resorting to a standard age-depth relationship (ocean island subsidence due to lithospheric cooling) back in time along the hotspot track for the last ~5 Ma, to produce maps of paleo-geography. This result allows the visualization of the approximate morphologies of the paleo-archipelago, thus yielding a rough idea about the possible major paleo-islands and the most likely interconnectivity relations: "*The Pleistocene Galápagos had a much greater area than the present islands. Land bridges existed between a few of the major islands, and many more minor islands and islets were exposed. We hypothesize that between 1 and 5 Ma, at least 19 major Galápagos Islands formerly existed but are currently submerged*". Furthermore, this assessment provides an understanding of potential styles of biological speciation in the region: "*Owing to the competition between subsidence and island growth, the subset of islands existing at any given time is complex, but the reconstructions suggest that at least seven major islands have existed since 5 Ma, permitting the opportunity for allopatric speciation of terrestrial organisms*". Altogether, their study shows that an accounting for the paleo-geography is crucial in understanding the phylogenetics of the target region. Taking this study as a primary reference, our goal is to go further back in time and try to understand the paleo-elevations along the Carnegie Ridge, and also to incorporate a broader range of geodynamic effects into models for island emergence/subsidence histories.

Plate reconstructions show that the Nazca plate (upon which the volcanic Galápagos Islands are emplaced) is converging with the South American plate at a present-day rate of ~80 km/Ma, and also that both plates are moving with respect to the Galápagos hotspot. In particular, the entire Carnegie Ridge extending from the Galápagos archipelago area eastward over the saddle point, and further east until the Nazca-South America subduction trench, is considered to be the topographic expression of volcanism and intrusion from the Galápagos mantle plume on the overlying moving Nazca plate Furthermore, this hotspot track extends eastward into South America, with the associated flood basalt province located perhaps in the Caribbean basin (*Richards et al.* [1989]).

The present-day relative speed between the Nazca plate and the Galapagos hotspot is of about ~40 km/Ma (*Christie et al.* [1992], *Werner et al.* [2003]). Nevertheless, before ~4 Ma ago, the speed was larger, perhaps up to 75 km/Ma (*Christie et al.* [1992]). The lack of systematic age measurements along the track, combined with the well-known fact that a simple age-distance progression is not likely to apply in the Galápagos platform area (where active volcanism is currently broadly distributed), makes the accounting for the relative plate velocities in a thermal subsidence model challenging. The Carnegie Ridge saddle point region's oldest volcanic rock

age is ~11.1 Ma (*Werner et al.* [2003]) at longitude ~85.1 ºW, although the magmatic edifice age must be slightly older than that. This yields an average (over the last ~12 Ma) relative speed value of about ~ 670 km/12 Ma ~ 56 km/Ma, consistent with the value of 59 km/Ma reported by *Geist et al.* [2014]. In Figure 3.2, ages along the track are shown as regional averages of dated volcanic samples.

Geodynamic considerations suggest that hotspot tracks are characterized by space-time-dependent topography, with elevated topography above and in the vicinity of the underlying plume conduit (*Davies* [1988], *Ribe and Christensen* [1999]), responding to the fluid dynamics of stagnation and buoyancy of highly-viscous flows (*Sleep* [1990]). Aside from this, geophysical studies have demonstrated the regular time dependence of ocean basin depth with plate age [*Johnson and Carlson*, 1992], as well as the associated effects on volcanism (*Orellana-Rovirosa and Richards*, [2017]). Here we review how mechanical and thermodynamic considerations regarding plate tectonics, mantle plume dynamics, and volcanism can account for paleo-elevations with respect to the current topography/bathymetry of the region. We seek to understand the genesis of present-day bathymetry of the Galápagos Archipelago, and also how accounting for various factors affecting island submergence can improve our understanding of the paleogeography along the Carnegie Ridge over the past ~20-30 Ma. Our longer-term aim is to provide a geophysical/geological framework in which the enormous Galápagos phylogenetic data base can ultimately be integrated with an accurate paleographic time history, perhaps providing the marine iguanas and their companions with a long-sought ancestral history, which is currently (*Parent et al.* [2008]) traced back to the South American continent.

3.2 Observations

The present-day topography/bathymetry is a primary source of information and point-of-departure for paleo-geographic studies. Spectacular topographic/bathymetric gradients are observed in the area. As shown by *Feighner and Richards* [1994], the present-day Galápagos mantle plume underpins lithosphere of ~11 Ma of age, with elastic thickness of about 12 km, which is clearly suggested by the flexural moat and bulge southwest from the archipelago's platform.

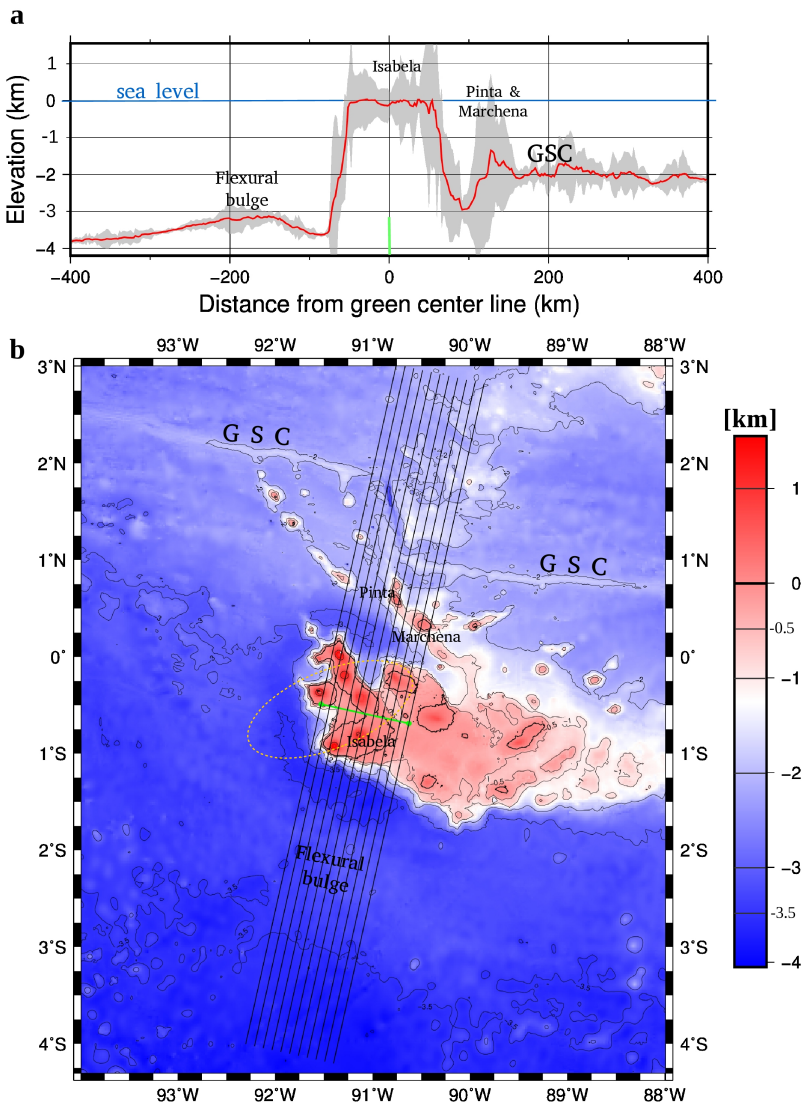

Figure 3.1. Present-day Galápagos Hotspot Swell: (a) Cross sectional profile, and (b) map view. Each profiling black line in (b) samples the bathymetry and contributes to the profiles envelope in gray (a), from which a median bathymetry profile is computed (red). The Galápagos Spreading Center (GSC) is offset by the 91ºW transform fault. Fine-dashed yellow ellipse marks the present-day location of the mantle plume creating responsible for the hotspot (*Villagomez et al.* [2014]).

Most of the present-day Galápagos Archipelago has been constructed upon an elevated platform, which decreases in height towards the east (with San Cristobal the easternmost island). The along-hotspot-track topographic profile (Figure 3.2) shows the elongated Carnegie Ridge decreasing in height toward the East down to a minimum on the saddle point region. It has long been understood (e.g. *Geist et al.* [2014], *Detrick and Crough* [1978]) that bathymetric depth increases with age of the volcanoes/seamounts along the Carnegie Ridge. *Geist et al.* [2014] suggest that island height decreases with the square root of time (age) along the Galápagos-Carnegie track, consistent with many studies and with theoretical considerations of thermal diffusion and subsidence. Beyond this, the red line profile in Figure 3.2(a) is probably, to this date, the best overall characterization of bathymetry along the Galápagos-Carnegie track. The bathymetry, although undoubtedly increasing in depth with age, does not behave precisely as the square root of distance along the track (which argues against the time relationship in the case of assuming a constant plate speed). The scaling with time, which is not linear as suggested by the deceleration of the Nazca plate relative motion, would render the first ~6 Ma of distance-history (eastern side of the profile) shorter on a time axis owing to a faster relative plate speed (up to ~75 km/Ma), and would render the signal less like the square-root-of-time, not confirming the relationship. The causes for this discrepancy are likely severalfold: (i) The study of *Geist et al.* [2014], does not consider the track at our sampling resolution level, and the 8-points curve fitting they performed is helpful, but not very accurate. (ii) Along the Galápagos-Carnegie Ridge, unlike in the Hawaiian Ridge (main referential system), the lithospheric age (and thickness) is discontinuous (owing to the presence of the 91ºW transform fault). (iii) The effective plume-melt flux delivered to the Nazca plate increased dramatically between 15-10 Ma due to the relative motion of the GSC with respect to the hotspot, which placed the underlying plume conduit fully beneath the Nazca plate. In summary of (ii) and (iii), the number of significantly-varying factors is larger in the Galápagos-Carnegie system than in the Hawaiian system and most hotspot tracks on Earth. (iv) When compared to Hawaii, the smaller plate-hotspot relative speed in the Galápagos makes the age-distance relationship less accurate in the volcanic expression, more so considering the space-time distributed age pattern of volcanism in the Galápagos archipelago (with Santa Fe being the oldest island, still active, in the middle of the platform; and with San Cristobal and Fernandina being the two most distant volcanic centers of the system, currently simultaneously active).

Our task is to explain the underlying causes for the geometry of this system, trying to disentangle or decouple the different causes and mechanisms that combined produce the observed bathymetry, or in other words, explain the topographic/bathymetric signal as the superposition of different independent signals. In particular, and following the line of *Geist et al.* [2014], we want to determine the likelihood of a paleo-Carnegie Ridge as comprising emerged land portions (islands) capable of having hosted abundant land species. Could the submerged regions along the Carnegie ridge have been above sea level at some point in the geologic past? How much shallower was the currently-deepest (>2 km depth) saddle point region in the past? Was this region above sea level at the time it was created by the Galápagos hotspot?

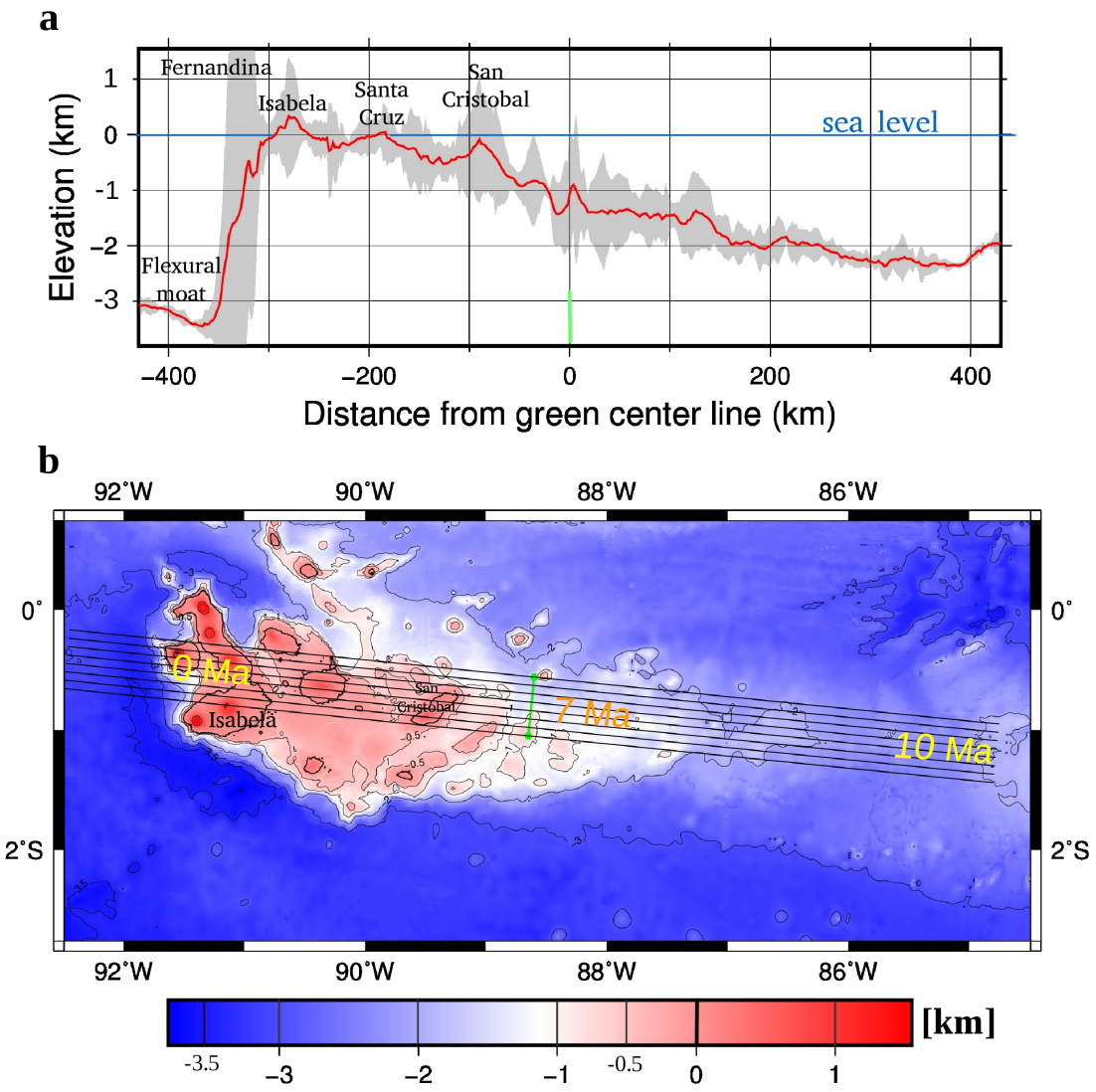

Figure 3.2. Present-day bathymetry of Galápagos and Carnegie Ridge saddle point area: Along-track profile (a), and map view (b). Each profiling black line in (b) samples the bathymetry and contributes to the profiles envelope in grey (a), from which a median bathymetry profile is computed (red). Ages in [Ma] are regional averages of volcanic rock samples ages (*Christie et al.* [1992], *Werner et al.* [2003]). As can be seen, the ages versus distance reveal some deceleration of the relative motion. The deepest region of the track (average ages ~10 Ma) is the Carnegie Ridge saddle.

3.3 The mechanisms for variable bathymetry over time in the Galápagos - Carnegie Ridge mantle plume province

In this section we analyze the important factors controlling island emergence and subsidence in the Galápagos - Carnegie Ridge region.

3.3.1 Lithospheric age

A primary cause of bathymetric subsidence comes from increasing plate age. The Carnegie Ridge saddle region developed by intrusion and extrusion of magmas from the Galápagos plume during times ~15-9 Ma, when the plume lay mainly beneath the Cocos plate, and in close proximity to the Galápagos Spreading Center; thus local seamounts, guyots, and intrusively-thickened crust of the Carnegie saddle region formed at depths corresponding to the plume-affected spreading center axis depth at the time. From present-day bathymetry, the region in the Galápagos Spreading Center from which the Carnegie saddle basement created, which is currently located about ~650 km away (NEE) from the hotspot, has average depths of about ~ 2.5 km. The background seafloor surrounding the Carnegie Ridge saddle (currently about 670 km East from the hotspot) has a depth of about ~3 km. Nevertheless, the whole region is still affected by some thermal buoyancy from the underlying plume, and the likely chemical buoyancy from depletion. Therefore, estimating the effective lithospheric subsidence age from present-day bathymetry cannot be done directly/reliably for the region. Noting that the plume swell would tend to reduce elevation contrasts between those two points, we anticipate an age-related subsidence of approximately 1 km.

Published age constraints (*Werner et al.* [2003]; *Barkhausen et al.* [2001]; *Wilson and Hey* [1995]) show that currently the Carnegie saddle region (a ~180 km-wide strip, Figure 3.3) overlies crust of age of order ~7-16 Ma (large uncertainties). Global data and theoretical considerations of thermal subsidence (e.g., *Turcotte and Shubert* [2002]) show that this age interval corresponds with a change in elevation of 0.94 - 1.42 km with respect to the spreading center. This range is consistent with our rough estimate based on the observed bathymetry, and thus it is likely a reasonable confidence interval. A central value of 1.18 km will be considered.

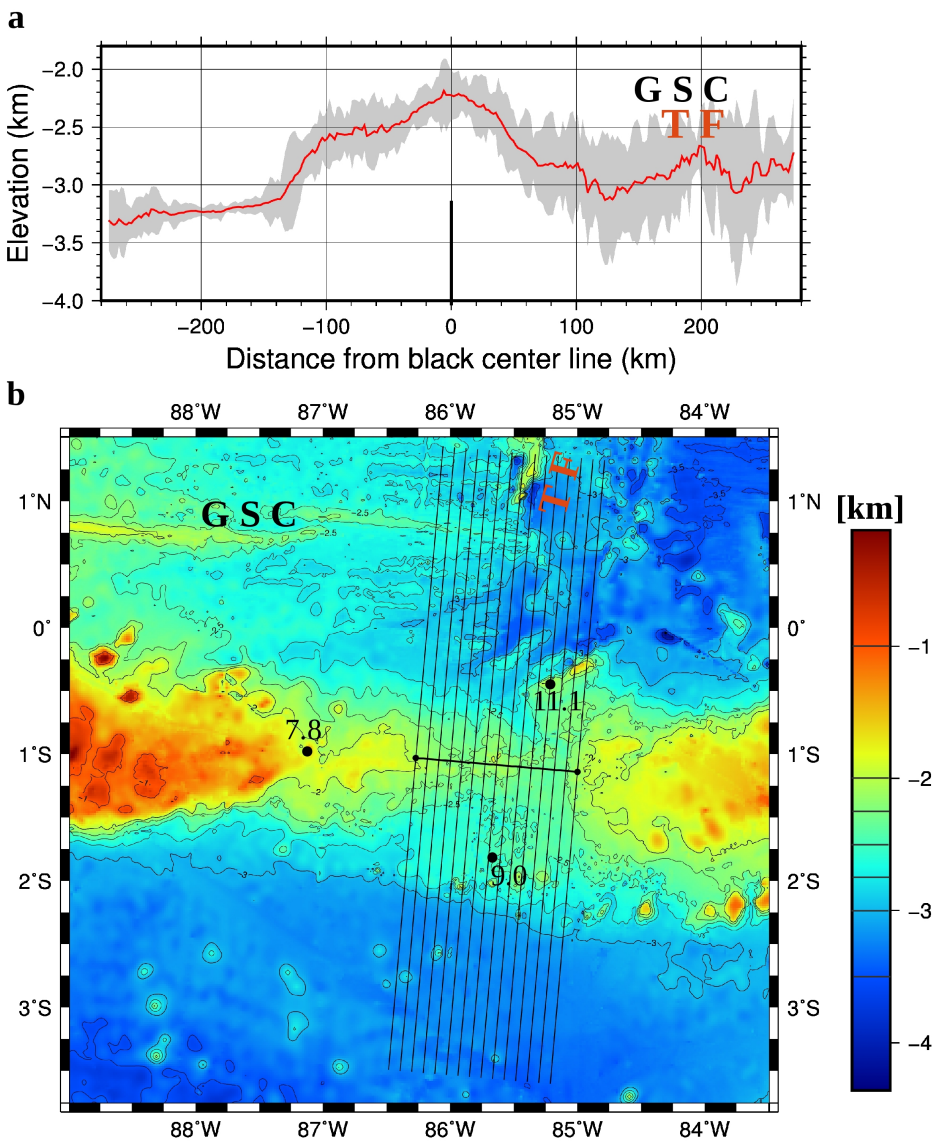

Figure 3.3. Present-day bathymetry of the Carnegie Ridge saddle region: (a) Cross-sectional profile, and (b) map view. Each black line profile in (b) samples the bathymetry and contributes to the profiles envelope in grey (a), from which a median bathymetry profile is computed (red). On the profiles (a), the Galápagos Spreading Center (GSC) and the Transform fault (TF) are expressed as bathymetric highs on a locally low area. In (b), numbers for black dots are dated ages in Ma (*Werner et al.* [2003], *Sinton et al.* [1996]). The average age of volcanic seamounts in the Carnegie saddle is about 10 Ma. The initial age of the magmatic construction must be older than the oldest sample of 11.1 Ma.

3.3.2 Mantle plume hotspot swell

The buoyant plume material stagnates under the moving lithosphere, creating a dynamic space-time-dependent bathymetric signal. The maximum height of this signal, roughly above (and slightly downstream) of the plume conduit, is determined by stagnation dynamics for a Stokes' flow, in which the buoyancy force is braked by velocity gradients that produce shear and normal viscous stresses.
The present-day Galápagos hotspot swell, as assessed by *King and Adams* [2014] from analysis of bathymetry, exhibits a full transverse width of about ~800 km, and a maximum height of ~0.793 km (these values represent an average of their two methods' results). Currently, the plume conduit as revealed by seismic tomography (*Villagomez et al.* [2014]), underpins lithosphere of ~11 Ma (likely a 8-14 Ma interval) which corresponds to an elastic thickness T_e ~10 km according to global data (*Watts* [1978], *Watts and Daly* [1981]), or perhaps more accurately to T_e ~12 km according to the local gravimetry analysis of *Feighner and Richards* [1994] (see Figure 3.B1 on the Appendix).

We wish to estimate the amount of vertical elevation change occurring in the Carnegie Ridge saddle region, over the past ~13 Ma, due to the mantle-plume effects alone. For this, we will estimate the difference between the past height and the present height associated with the hotspot swell for that region of the Nazca plate (which has moved and aged accordingly). The age of ~13 Ma is approximate, but it is assumed to be a good estimate for the initial age of construction of the local magmatic edifice, after considering the 11.1 Ma oldest rock, which is a seamount, and thus a minimum age of the edifice.

3.3.2.1 Past: Estimating hotspot-swell maximum height at the Carnegie ridge saddle 13 Ma ago

The Carnegie Ridge saddle region was emplaced at lithospheric ages of less than 2 Ma, corresponding to an approximate lithospheric elastic thickness of T_e~5 km (data for East Pacific rise, *Watts* [1978], *Watts and Daly* [1981]), and T_e<6 km according to *Feighner and Richards* [1994]; with the mantle plume conduit impinging underneath. So, recalling the aforementioned present-day stagnation conditions of the hotspot (T_e~12 km), we conclude that during the last ~13 Ma, the plume has stagnated under lithosphere of variable thickness, with a factor ~2+ increase in thickness during recent times.

Although from the purely isostatic point of view such an increase should not produce any important change in topographic uplift, elasticity must play some role in the problem. Considering the lithosphere as an elastic plate resting over a viscous mantle and overlain by seawater, and subjected to a constant vertical line force, the theory predicts a vertical displacement u scaling with $\sim T_e^{-3/4}$. With these considerations, the factor 2 increase in lithospheric thickness (with time) translates into a factor 1.68 decrease in uplift. Thus, the flexural response of the lithosphere suggests a higher past value of the hotspot-swell height, of ~1.68 x 0.793 km = 1.33 km. Finally, regarding elasticity as playing only a subordinate role in a mantle plume province on young lithosphere, we estimate that the past value of uplift must have

been between the ones predicted by isostasy and flexure, but closer to the isostatic end. For the past value of hotspot-swell maximum uplift: the isostatic value is 0.793 km, and the flexural response value is 1.33 km. Then, the perhaps more likely confidence interval for the past uplift would be upper-bounded by ~(0.793+1.33)/2 = 1.06 km.

These estimates assume time-invariance of the plume buoyancy flux and the Nazca-plate-hotspot relative speed. Regarding the deceleration of the relative motion Nazca plate-Galápagos hotspot, it would tend to slightly lower the value of the predicted past maximum uplift (owing to a larger relative speed in past times). This further confirms the previous confidence interval to be the lower half of the extremes (isostasy-flexure) interval. For the final estimate of the past maximum uplift, a central point value of 0.93 km uplift will be considered (located at a quarter of the extremal interval).

3.3.2.2 Present: Estimating the current hotspot-swell maximum height at the Carnegie ridge saddle

This hotspot-swell uplift signal does not fully decay in time and downstream, due to remnant buoyancy (thermal and compositional) of the underlying plume material. For the saddle region, currently located ~670 km east from the hotspot, after 13 Ma, there is no current estimate for the surface swell amplitude. Figure 3.3 shows a detailed map with the local bathymetry.

Our approach is to use the currently estimated plume volume-flux to estimate the evolving width and thickness of the ponded plume material downstream, based on scaling theory; from it, isostasy will provide an estimate of the topography. Considering the strip of sublithospheric plume material to be a buoyant stagnated fluid layer, its thickness s is given by an expression of the form

$s \approx \left(\frac{Q\cdot\eta}{\delta\rho\cdot g}\right)^{1/4}\cdot G\left(a\cdot\pi_b\right)$ with $\pi_b = \frac{Q\cdot\delta\rho\cdot g}{\eta\cdot U^2}$ the buoyancy number and G a function to be determined.

Ribe and Christensen [1999] used numerical simulations to obtain the proportionality constant a and the function G for the scaling law (over a range of values of the buoyancy number), for a quasi-isothermal problem. Summarizing, they found $a \approx 0.0208$ and $G\left(\pi_b\right) \approx 1.26\cdot\tanh\left(1.01\,\pi_b + 0.687\right)$.

For the Galápagos, this method yields characteristic values for the plume strip thickness of s~78 km and strip half-width of about ~450 km. This method ignores the dynamic stagnation in the region where the plume conduit transitions to plume strip.
Horizontal spreading of the plume strip by buoyancy and stagnation reduces its thickness in time (assuming incompressibility). At distances of 670 km downstream, the hotspot (which equates to almost ~1.5 times the half-width), a factor ~1.45 of spreading (using the results of *Ribe and Christensen* [1999]) has reduced the strip thickness to 69% its initial value, or ~54 km.

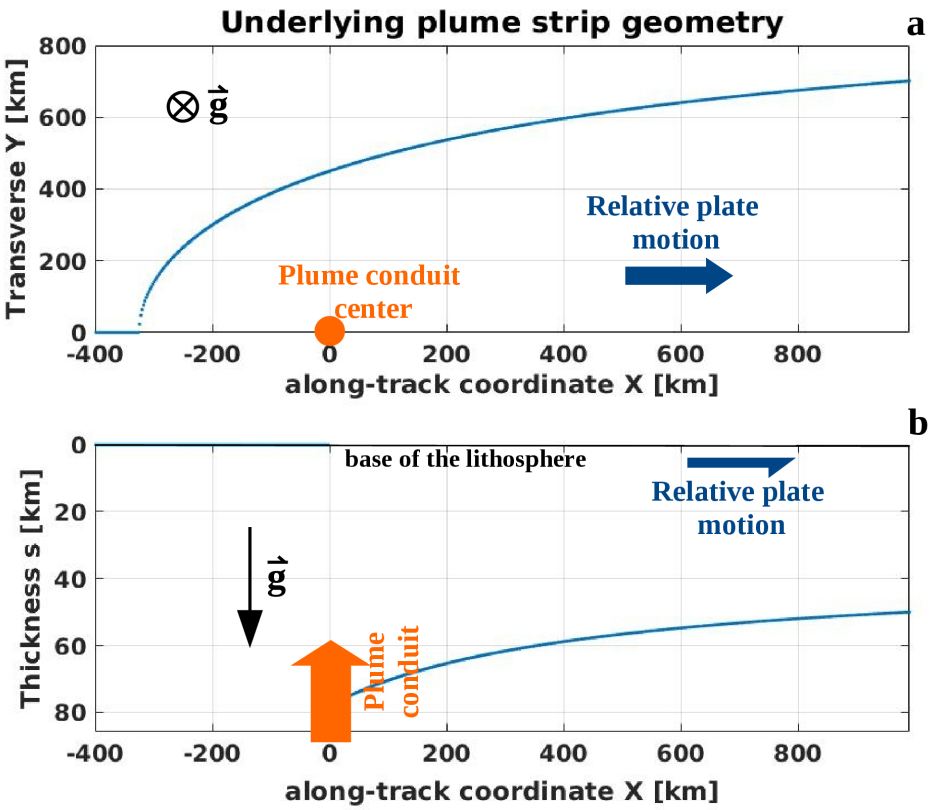

Figure 3.4. Evolution of the plume stagnation zone and strip, following the theoretical-numerical assessment of *Ribe and Christensen* [1999]. (a) View from above: The ponded plume material, with a characteristic transverse width of ~450 km at the conduit coordinate, spreads horizontally downstream with plate motion. (b) Vertical axial mid-plane view: plume strip thickness evolution responding to incompressible mass conservation.

Nevertheless, this 'isothermal' calculation neglects diffusive cooling of the buoyant plume strip. Regarding the heat conducted upward to the lithosphere and seawater as that responsible for buoyancy loss, and neglecting the locally thin (<6 km) lithospheric elastic thickness (*Feighner and Richards* [1994]); if we consider half the strip thickness as a reasonable thermal length-scale (the actual cooling length scale could be even smaller) and calculate the thermal diffusion timescale at this stage, 670 km (~13 Ma) downstream the hotspot, we get τ_{th_diff}~20 Ma. This means that after 13 Ma, thermal diffusion starts to become important. Therefore, the actual buoyant plume-strip thickness must be smaller than 54 km, and we consider that values of ~35-45 km might be reasonable. Finally, with these estimates of plume strip thickness, isostatic compensation would predict topographic heights of ~0.3-0.38 km. A central value of ~0.34 km will be considered for the subsidence calculation. A fraction of this buoyancy-driven topography is expected to be perennial, as the depleted mantle plume is characterized by a mild compositional positive buoyancy.

3.3.2.3 Net difference

Finally, the height-extremes difference between the past value (0.93 km) and the present value (0.34 km) gives the hotspot-swell net subsidence for the Carnegie saddle during the past 13 Ma, which would be of about ~0.59 km, with a confidence interval of about 0.45-0.76 km.

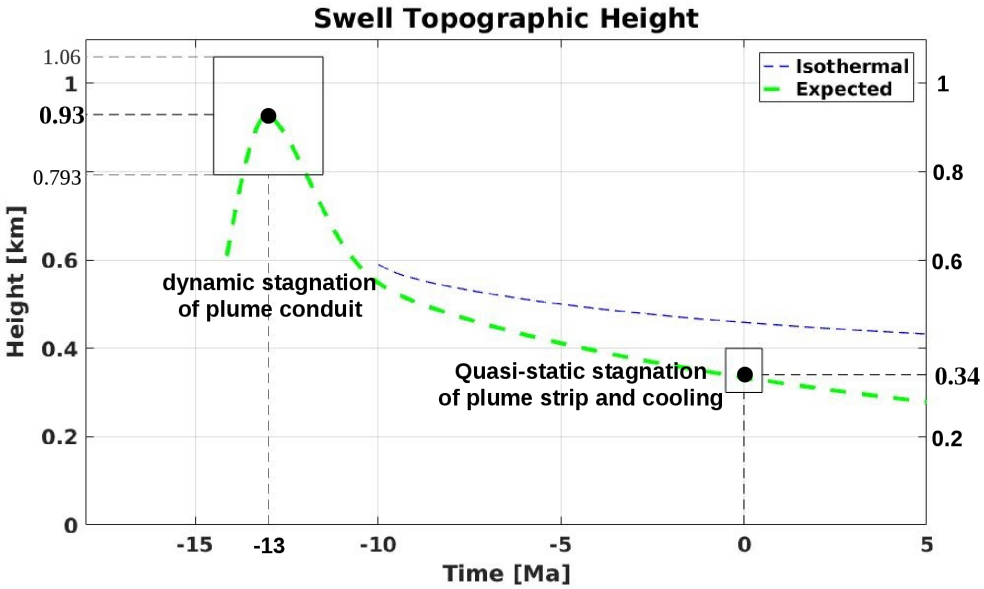

Figure 3.5. Evolution of the hotspot swell topographic height evaluated at a material point fixed on the Carnegie saddle rock mass. Time scale goes with the normal arrow of time. The two rectangles represent confidence intervals. Starting after ~15 Ma (creation at the GSC) the Galápagos mantle plume was in the vicinity, therefore dynamic stagnation of the plume conduit under the young lithosphere generates the maximum swell uplift. The lower value of 0.793 km would be predicted if pure isostasy applied throughout the history of the process, whereas 1.06 km is an upper bound responding to some degree of elasticity (extremes interval mid point, see text). During the last ~9 Ma, the stagnation of the ponded plume strip reduces its thickness and topography above, as predicted by the isothermal calculation of *Ribe and Christensen* [1999]; but some cooling takes place further decreasing the plume strip thickness and topography.

In addition to all the aforementioned mechanisms, cyclic sea level changes due to glacial cycles also enter into the island emergence/subsidence histories. Nevertheless, most of the Eustatic signal is contained in periods of fractions of 1 Ma, thus likely not altering the evolutionary clock synchronous with the hotspot swell migration across the Nazca plate, on time scales of tens of Ma.

3.3.3 Geometrical variations in excess crust generation

3.3.3.1 Magmatic construction development and crustal thickening

i) Seamounts intrinsic height: Given by the volume and height of the proper volcanic cones/seamounts (with horizontal length-scales of less than 20 km), whose geometry is defined by basaltic eruption and solidification dynamics. This bathymetric signal component develops on timescales of normally less than ~1 Ma responding to the time history of local basaltic volcanism, and is virtually constant although perhaps slightly diminished by erosion.

ii) Underlying magmatic rise: Defined by both intrusive and extrusive construction with horizontal length-scales of more than 20 km (platform, plateau, rise, ridge) over which the seamounts are emplaced. Mantle-plume-derived magmatism increases crustal mass and thickness, allowing for vertical and horizontal transport of magma and crustal emplacement, , finally developing bathymetry in the form of ridges and platforms, mostly by intrusion (>50% mass).

For the Carnegie Ridge saddle bathymetry at the present-time (Figure 3.3), (i) and (ii) amount to a height perhaps of order ~0.5 km, considering that the full height of the rise is close to 1 km.
Since it is impossible to perfectly isolate the magmatic edifice from the plume buoyancy strip isostatic rise solely based on bathymetric maps, a high error in the estimate is expected. Increase in the mass of shallow intrusion and extrusion during the creation of these magmatic edifices generates rising seamounts. If volcanic growth occurs near sea level, it might cause the magmatic construction to emerge during the process. In this case, the edifice height is a variable that would enter on the calculation for subsidence.

3.3.3.2 Deformation and relaxation of the magmatic edifices

Once the magmatic construction takes place, it remains largely unchanged in time, with mild contributions to subsidence. We need to account for processes that alter the geometry of the magmatic edifices once created. Submarine erosion as well as sea-level erosion might have potentially lowered the highs in time; their effect is nevertheless likely very small. Relaxation of lithostatic pressure gradients occur, broadening the construction and lowering its highs, in timescales of a few million years, as shown by *Orellana-Rovirosa and Richards* [2015] (with their model for the Eastern platform region having an initial 2 km-thickness, experiencing a ~0.25 km subsidence during a 3 Ma span). Yet at the same time, volcanic construction takes place over the deforming platform.
The present-day Carnegie Ridge saddle region (Figure 3.3) is roughly a ~180 km wide rise, likely composed of magmatic construction (estimated maximum vertical thickness ~0.5 km) plus buoyant plume-strip swell (estimated maximum uplift in ~0.34 km). In the same way as the Galápagos eastern platform, its vertical expression above the background suggest that it must have undergone some relaxation: its height of ~ 0.85 - 1 km (comparatively smaller driving force), and its creation more than 10 Ma ago (comparatively larger time span), suggest a ~0.2 km subsidence contribution as a reasonable estimate.

3.3.4 Total subsidence

With the three mechanisms above considered, we can estimate the total subsidence likely undergone by the seamounts on the Carnegie Ridge saddle point area since ~13 Ma.

$$\text{Expected } S = S_{\text{plate age}} + S_{\text{hotspot swell}} + S_{\text{crustal relaxation}}$$

$$= 1.18 \text{ km} + 0.59 \text{ km} + 0.2 \text{ km}$$

$$= 1.97 \text{ km}$$

Expected Confidence Interval bounds: Min S ~ 1.54 km , Max S ~ 2.43 km

On the other hand, the observed, present-day depths of the elevated portions of the saddle point region are on the interval (2 - 2.5) km (considering the profile (a) and contour levels (b) on Figure 3.3, which seemingly enclose some area, potentially having been paleo-islands). This observed range is well overlapped with our expected confidence interval. This means that there is a good chance for the present-day seamounts at the Carnegie Ridge saddle point to have been emerged back in time between 15-10 Ma ago.

These calculations represent one way to estimate the change in elevation using theory and observations, and will be taken as reference for the numerical calculations presented in the next section.

Considering that the observed depth range of the region falls roughly between our expected value (~2 km) and our maximum value, there is a non-negligible probability of a slight deficit in our estimation if the region was actually emerged in the past.
As an aside, the size of the volcanoes might have changed during the process, in which case they would be a variable entering the equation. We will treat these problems in the discussion section.

3.4 Numerical modeling

In this section we will show preliminary results from our numerical computations, aimed at modeling the Galápagos environment and the effects of the mantle plume on dynamic topography. For this purpose, we made use of the Software ASPECT, developed by CIG (Computational Infrastructure in Geodynamics), in particular, ASPECT version 1.5.0 (*Bangerth et al.* [2017], *Kronbichler et al.* [2012]) published under the GPL2 license. ASPECT is a finite element parallel code to simulate problems in thermal convection, and uses adaptive mesh refinement.

3.4.1 Model settings

We model thermal convection in a box 1800 km-long in the plate-hotspot motion horizontal direction (x), 1200 km-wide in the transverse horizontal direction (y), and 550 km-deep (with gravity acting on the direction (-z)). This box is an Eulerian control volume for the fluid it contains, which satisfies the Stokes flow equation, incompressible mass conservation equation, and the energy equation for temperature. Thermal expansivity (variable density) plays its role via the Boussinesq approximation.
The velocity boundary conditions reflect the relative motion of the plate and asthenosphere with respect to the plume, with this latter one having its source 'anchored' to the box frame. The plate motion defines the up/downstream directions. The vertical wall upstream (x=0), the horizontal upper boundary (z = H = 550 km) and the vertical wall downstream (x=1800 km) have a general Dirichlet velocity B.C. with $\vec{v} = v_0 \cdot (z/H)\,\hat{x} + 0\,\hat{y} + 0\,\hat{z}$; which produces a Couette-like ambient mantle wind. These conditions produce mass inflow on the upstream wall and mass outflow on the downstream wall. The lateral vertical walls (y=0 , y=1200 km) have tangential flow: Dirichlet normal velocity conditions $v_y = 0$, and Neumann condition $\partial v_x / \partial y = 0$ (shear stress free). The velocity at the lower boundary (z=0) is free in 3D, simply with a zero net mass-flow across it.
The Temperature boundary conditions are zero heat flux (Neumann type) at the lateral vertical walls (y=0 , y=1200 km) and at the trailing vertical wall (x=1800 km). The upper, lower and upstream boundaries have Dirichlet-type temperature BCs. At the top surface (z=550 km) T_{surf}=7ºC. At the lower boundary surface (z=0 km), the temperature corresponds to an ambient asthenospheric isotherm T_{surf} + DT , plus a 2D-Gaussian hot-thermal perturbation intended to mimic the plume source:

$$T(z=0) = T_{surf} + DT + \Delta \cdot \exp\left(-(r/r_p)^2\right)$$

with *DT* the background temperature difference across the box depth *H*, and Δ the plume's thermal perturbation amplitude.
Variable r is the polar radius on the lower boundary surface:

$r^2 = (x-x_c)^2 + (y-y_c)^2$; with (x_c,y_c) the plume source center coordinates, and r_p the Gaussian radius of the plume anomaly (see parameters table).

At the upstream wall (x=0) there is a prescribed, inhomogeneous Dirichlet, incoming asthenospheric geotherm with a temperature profile given by a depth-dependent error function:

$$T_{upstream}(z) = T_{surf} + DT \cdot erf\left((H-z) / 2\sqrt{(\kappa \cdot t_0)}\right)$$

where t_0 is the initial time and κ the average thermal diffusivity.

The model employs Arrhenius-type temperature-dependent viscosity, with a linearized form for the argument in T:

$$\eta = \eta_0 \cdot \exp(-\beta(T - T_0)/T_0)$$

The temperature initial condition of the system is given by an error function geotherm with the same form and amplitudes as the boundary condition of the upstream vertical wall, so there is a perfect matching at the initial time.
For our velocity boundary conditions on the upper boundary, ASPECT provides an equivalent dynamic topography computation, using the total vertical normal stress (viscous plus pressure), to calculate the associated isostatic topography, given the mass densities of the mantle and sea water.

As a model test, we have benchmarked against the numerical model of *Ribe and Christensen* [1994] for the Hawaiian plume. There are some incompatibilities between the two computer programs, specifically in the lower boundary condition implementations, but the agreement is good. A brief summary of this benchmarking is found in the Appendix.

3.4.2 Results

We have chosen a set of parameters that are appropriate for the Galápagos situation.

Parameter	value	units	description
t_0	5	Ma	initial time
t_f	45	Ma	final time
Lx	1800	km	box length (along plate motion)
Ly	1200	km	box width (transverse)
Lz or H	550	km	box height (vertical)
c	1250	J / kg·^{0}K	specific heat capacity
κ	9.7×10^{-7}	m^2/s	thermal diffusivity
ρ_m	3300	kg/m^3	mantle mass density
ρ_w	1000	kg/m^3	sea water mass density
α	3.5×10^{-5}	$^0K^{-1}$	thermal expansion coefficient
η_0	10^{21}	Pa·s	reference viscosity (at $T=T_0$)
β	8	-	viscosity law exponent
T_0	1150	^{0}K	reference Temp. in viscosity law
v_0	40	km/Ma	plate relative horizontal speed
T_{surf}	280	^{0}K	sea water temperature
DT	1300	^{0}K	temperature difference
Δ	200	^{0}K	plume thermal anomaly
x_c	600	km	plume source center x coordinate
y_c	600	km	plume source center y coordinate
r_p	37	km	plume thermal Gaussian radius
g	10	m/s^2	gravity acceleration

Parameters Table

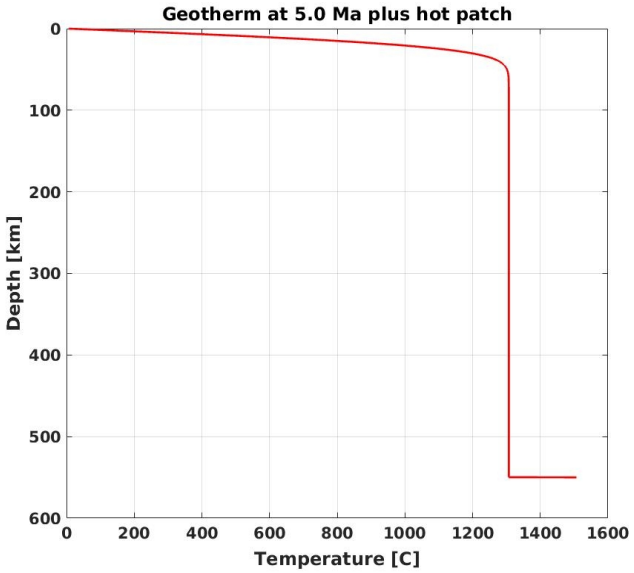

Figure 3.6. Temperature vs. depth valid for the initial condition of the system at 5 Ma (valid throughout the entire volume). The boundary condition on the upstream wall (x=0) has an identical temperature profile except for the absence of the hot patch at the bottom.
For the parameters used here, the theoretical diffusive length scale $2\cdot(\kappa\cdot t)^{1/2}$ ~ 25 km, and the depth of the 1300 ºC isotherm is of about ~50 km.

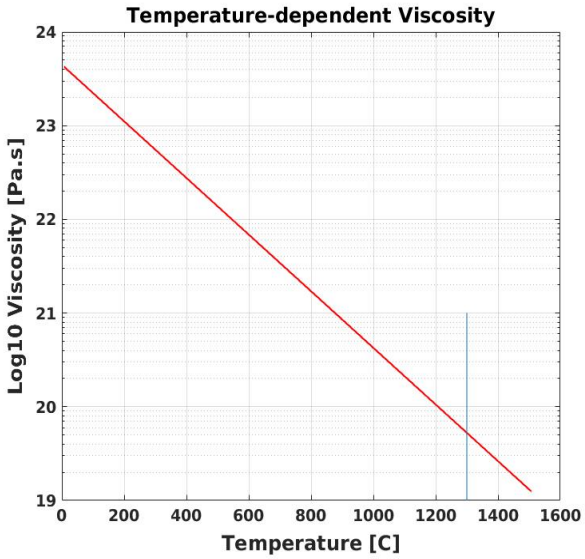

Figure 3.7. Viscosity vs. Temperature: general function for our model. The blue line marks the maximum temperature in the absence of the plume source, which defines the temperature profile on the upstream wall (x=0) boundary condition. The minimum viscosity of the model (at the center of the plume source) is ~1.2 x 10^{19} Pa·s.

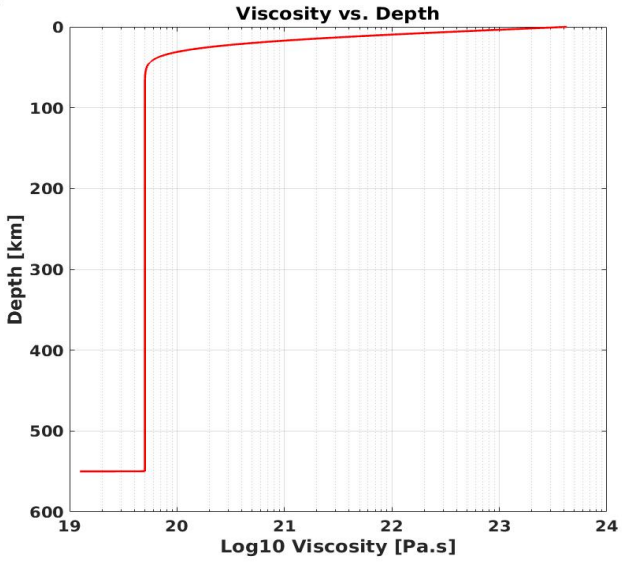

Figure 3.8. Viscosity vs. depth valid for the initial thermal condition of the system. The minimum and maximum viscosities of the system are ~1.2 x 10^{19} and ~4.2 x 10^{23} Pa·s. Most of the mass (~80 %) of the system has a viscosity of ~ 5 x 10^{19} Pa·s.

3.4.2.1 Initial condition: t_0 = 5 Ma

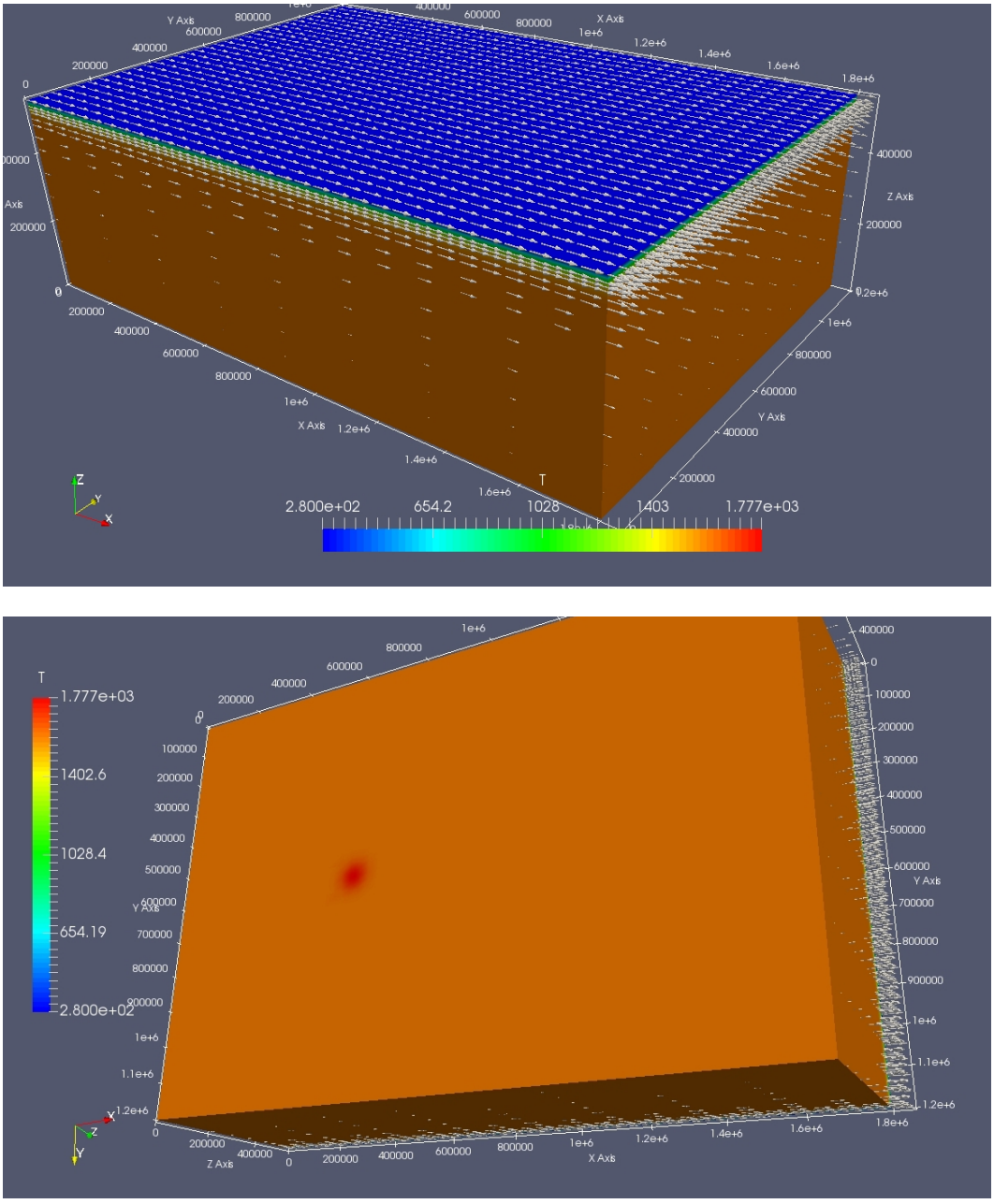

Figure 3.9. Initial condition of the system (time t_0 = 5 Ma), temperature field (ºK) and velocity vectors. Upper: oblique view; the ambient Couette asthenospheric wind can be observed, mass is outflowing across the downstream wall. Lower: bottom view, where the Gaussian temperature anomaly (plume source) can be observed.

3.4.2.2 State of the system at t = 45 Ma

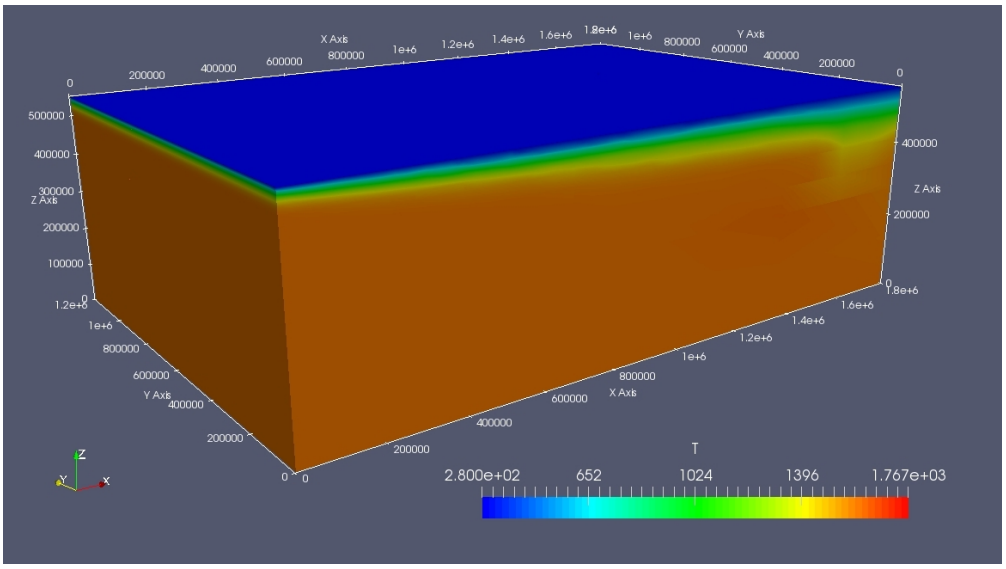

Figure 3.10. Condition of the system at time t=45 Ma; temperature field (ºK). The thermal boundary layer (thermal lithosphere) has developed downstream. Some extra localized thickening occurs as given by negative buoyant instabilities. At this stage, the plate has advanced a distance of about 1600 km, which means that the trailing 200 km of the domain have a thermal age of 45 Ma. Some negatively buoyant instabilities have manifested in that region.

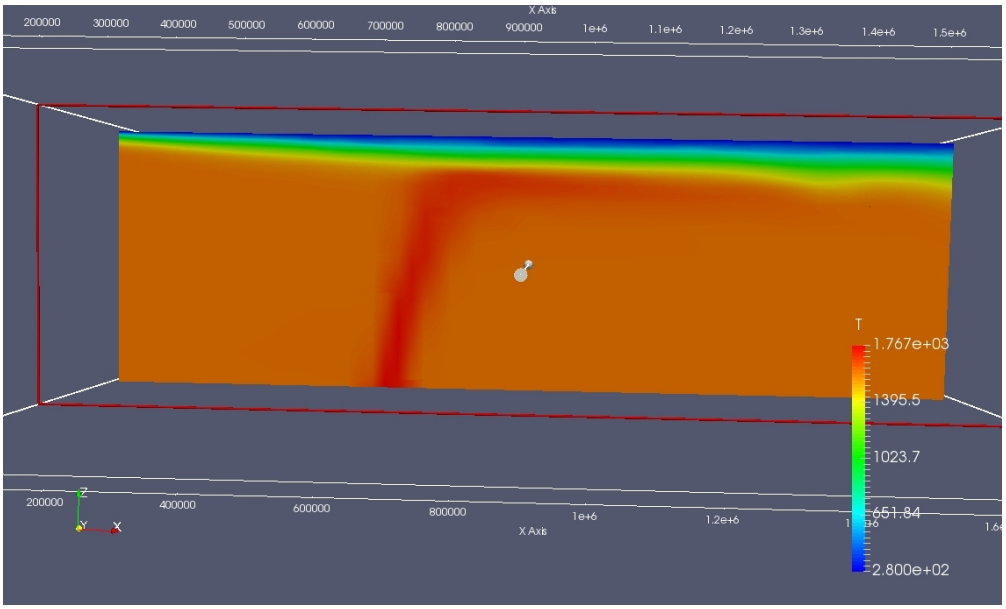

Figure 3.11. Condition of the system at time t=45 Ma; temperature field viewed by clipping on the mid plane (y=600 km). The plume conduit and the dragged-and-stagnated plume strip can be clearly appreciated. The plume conduit undergoes substantial advection and dragging starting from depths of ~300 km, and bends and stagnates under the moving lithosphere.

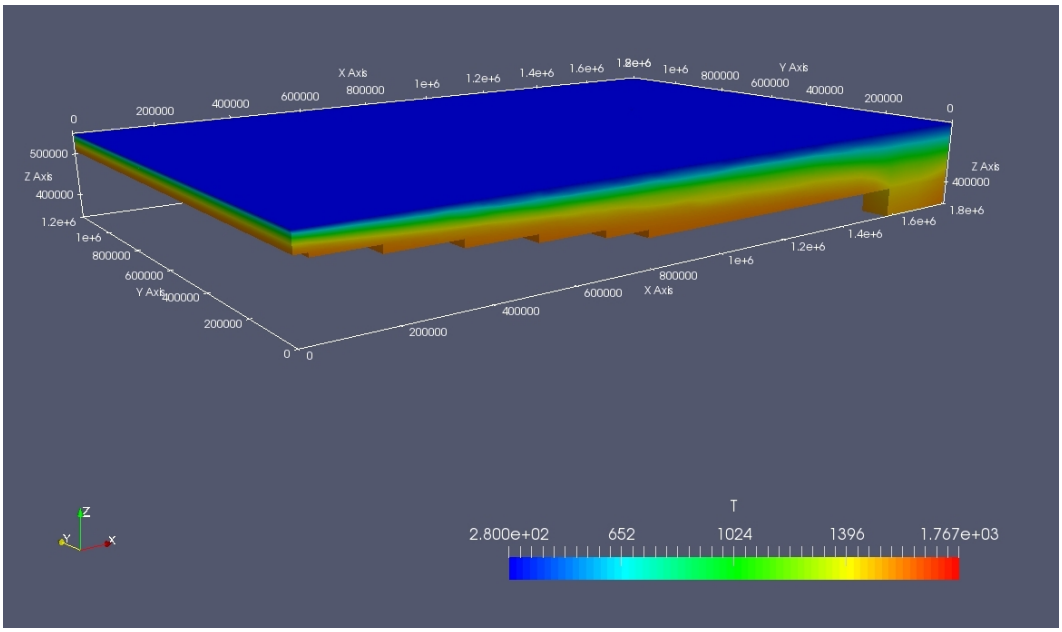

Figure 3.12. Condition of the system at time t=45 Ma; temperature field, cold domain subset defined by T in [280, 1573] ºK, which should define the thermal lithosphere of T ≤1300 ºC.

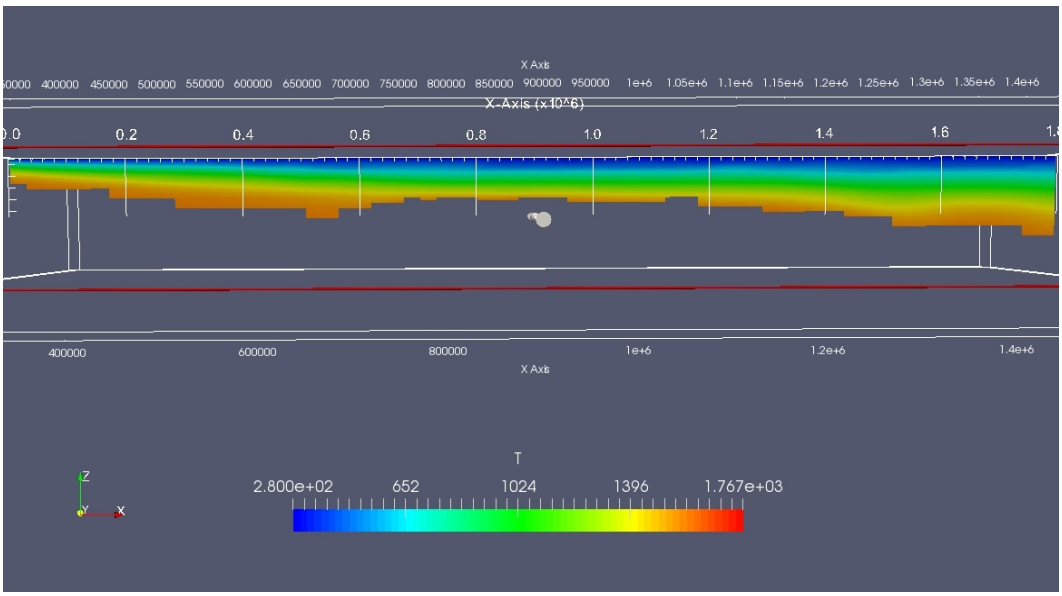

Figure 3.13. Condition of the system at time t=45 Ma; temperature field, cold domain subset defined by T in [280, 1573] ºK, which should define the thermal lithosphere of T ≤1300 ºC, view on the mid-plane (y=600 km) slice. Thermal erosion of the lithosphere has clearly taken place, with a maximum erosion above the plume stagnation region, between 200-600 km downstream the plume stem. The minimum lithospheric thickness is ~75 km, occurring at x~900 km (300 km downstream the plume source). This value contrasts with the ~100 km lithospheric thickness at x=500 km, and also with the depth value the 1300 ºC isotherm should have at x=900 km (age 27.5 Ma) in the absence of a plume, which would be ~115 km.

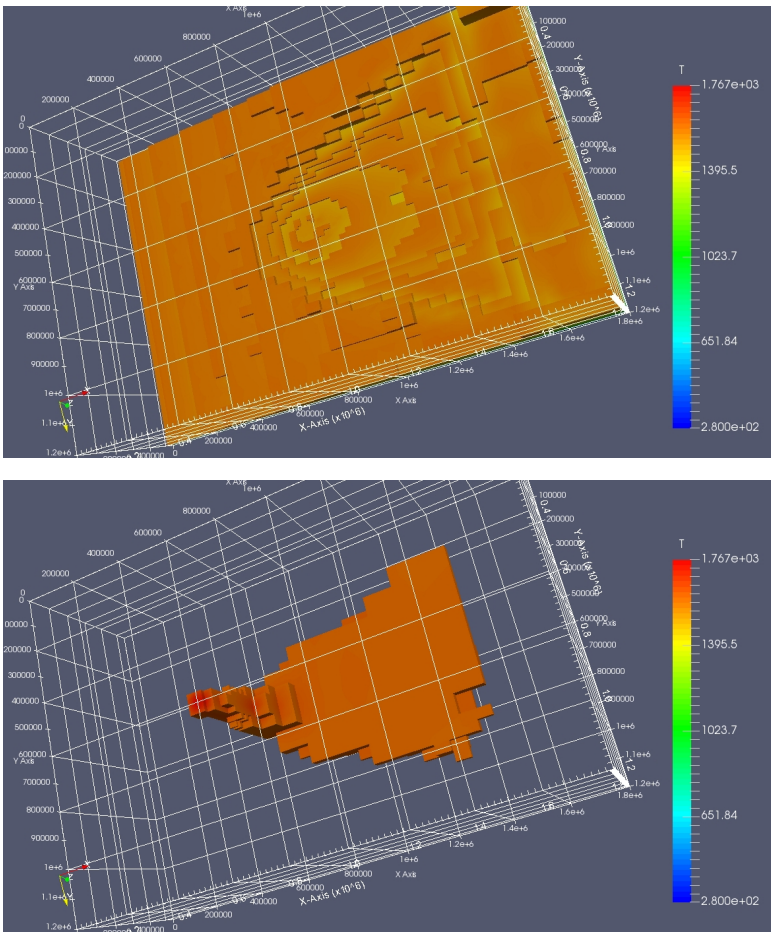

Figure 3.14. Condition of the system at time t=45 Ma; temperature field, viewed from below. Upper: cold domain subset defined by T ≤1300 ºC. Lower: hot domain subset defined by the hottest ~196 ºC of the system, which adequately isolates the plume. Ponded plume material is advected downstream as a stagnant strip under the lithosphere, and broadens significantly with time and distance, producing an erosive imprint on the lithosphere's base.

Given our model parameters and the temperature boundary conditions, the background Rayleigh number is $Ra \sim 5x10^6$. Analogously but at the local level, the plume conduit, having a 200 ºC excess temperature, would have an associated $Ra_{plume} \sim 2x10^7$(with respect to the upper boundary). These values, beyond guaranteeing convection, should guarantee the manifestation of a small degree of time-dependent convection.

In this simulation, the buoyancy flux of the upwelling plume, as measured at the lower boundary (z=0), is of about B ~0.85-1.0 [Mg/s], or equivalently, a surface volume flux $Q_s \sim 0.36 – 0.42$ [m^3/s]. These values are in between those reported by *Sleep* [1990] and *King and Adams* [2014] for the Galápagos mantle plume.

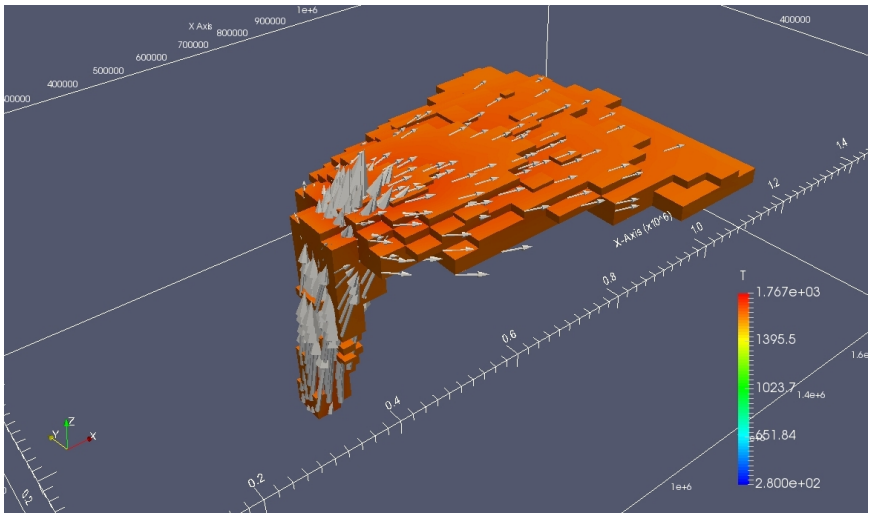

Figure 3.15. Condition of the system at time t=45 Ma; temperature field. Hot domain subset defined by the hottest 196 ºC of the system, which adequately isolates the plume. Scaled velocity vectors superimposed (with a plotting stride of one sample per 20 grid points). Maximum ascent speeds are of about ~280 km/Ma.

Considering the model velocity field at the final stage (40 Ma after the initial condition), the maximum speed in the domain is found on the plume conduit center line (ascent speed) with a magnitude of ~284 km/Ma, and a conduit average of ~95 km/Ma; these values are found at depths of more than 300 km. The maximum and average conduit ascent speeds, when compared to the overlying plate horizontal speed (~40 km/Ma) give ratios of about 7 and 2.4 respectively. Although the plume conduit has a radial influence (in temperature and velocity) of almost 200 km, the region with significant ascent speeds is confined to a radius of about ~40 km (consistent with the plume source anomaly at the bottom).

At shallow depths (<200 km) the ascent speeds are smaller than the plate speed (horizontal velocity), because the plume material is affected by drag due to the overlying plate. In this respect, the strong drag and deflection experienced by the plume material prevents the formation of an upstream stagnation bulge of plume material (Figure 3.11), the plume conduit bends with the mantle wind and plate motion starting at depths of approximately ~300 km. This result, coming from a purely numerical simulation, would predict the absence of volcanism upstream of the plume conduit, the volcanism should only manifest starting some distance downstream (about ~100 km from the original source at x=600 km). The geological validity of this prediction will be assessed in the discussion section.

3.5 Discussion

Beyond the conceptual assumptions, biases and errors in biological species age determination, we will focus just on the immediate work presented here and discuss uncertainties in the geophysical assessment.

3.5.1 Subsidence estimation

There are important sources of error in the estimation of bathymetric depths, lengths and seafloor ages. Beyond that, the age-depth formulas of *Johnson and Carlson* [1992], *Turcotte and Shubert* [2002] were produced from global data analysis and are likely robust.

Some errors may result from our analytical estimation of the hotspot swell, owing to underlying assumptions of fluid mechanics (such as incompressibility of the plume strip) and thermodynamics, and the approximations to the general equations. Moreover, the scaling laws provided in the work by *Ribe and Christensen* [1999], although covering a wide range of the buoyancy number, were intended to understand the Hawaiian system. One of the underlying assumptions on our estimation of uplift-subsidence, is the superposition principle. We aimed at an estimation of the subsidence via a decomposition into separate components (age-depth, hotspot swell, crustal relaxation). Nevertheless, it is not entirely clear that a theoretical assessment of the hotspot swell by considering it being an isostatic (and slightly flexural) response of a horizontal layer underlain by a viscous fluid, will actually be a good approximation for a real mid-ocean ridge environment, in which topographic gradients and different buoyancy distribution and velocity field patterns exist.

As an aside, the growth of the magmatic edifices (with perhaps ~0.5 km maximum height, Figure 3.3) might have taken place during the period of maximum elevation of the background (shallowest depths of the region) and close to sea level, in which case their height would be a time variable that would implicitly relate to the islands emergence and area development. So somehow, if the magmatism took place near sea level, the height or thickness of the magmatic edifices also enters in the equation, perhaps with a negative sign.

For all these reasons, in our estimates we have presented broad confidence intervals.

Beyond these uncertainties, the calculations above show that plate age-dependent topography, plus dynamic hotspot swell topography plus crustal relaxation, all combined seem to suffice to account for a paleo-geography on the Carnegie Ridge saddle point area, that comprised seamounts at elevations around sea level, potentially allowing for emerged topography (paleo-islands that are currently submerged). Due to the relative plate-hotspot motion, this elevated topographic signal migrates relative to the plate. With transverse characteristic dimension w~150-200 km, and assuming a roughly circular (or square) bulge (the elevated portion of the ridge), the characteristic timescale for elevated topography is w/u_{plate} ; then considering u_{plate}~3.5-7.5 km/Ma, this would yield values of 2 - 5.7 Ma. This means that along the Carnegie Ridge, the characteristic time span an archipelago (of ~180 km characteristic length) remains emerged is of about ~4 Ma. This time-dependent island/seamount elevation history implies important variations in island areal extent and connectivity. Changes in the islands' areal extent and connectivity are controlling factors for speciation of land flora and fauna, controlling the number of species and the number of individuals.

Over the past 15 Ma, the average Nazca plate - Galápagos hotspot relative horizontal speed was ~55-60 km/Ma. If this average speed was similar in past times, and considering the present-day distance between the Galapagos hotspot and the Nazca - South American trench, of ~1150 km; it would have been ~20 Ma ago that the hotspot swell was on the trench region. Nevertheless, the Nazca and South American plates are currently converging; thus, the time for this hotspot swell to have visited the trench was probably larger, perhaps 30 Ma ago or more. These are the timescales that must be considered for speciation events along the Carnegie Ridge, if a South American origin is to be sought, which is the case for most of the Galápagos endemic land faunal species, e.g. *Parent et al.* [2008].

3.5.2 Numerical model

Our numerical model, still in a preliminary stage, contains a number of approximations and biases. Among them are incompressibility and Boussinesq approximation (very common in numerical models); as well as the purely temperature-dependence of viscosity (with a linearized form for the Arrhenius law) that although provides a completely reasonable profile (that implicitly incorporates the lithostatic pressure effect), neglects the dynamic pressure effects on viscosity, which are certainly of second order. With the assumption of Newtonian viscous behavior, we are for example discarding dislocation creep, which could produce more concentrated deformation zones.

The discarding of more complex constitutive models, for example considering elasticity (although likely having a small effect on a plume-affected young lithosphere province) is also a source of error. For that reason we presented an analytical estimation of the swell height that makes reference to the mild elastic effects the lithosphere has on the hotspot swell height.

Our model has a constant plate-hotspot relative velocity, and a decelerating motion will be implemented in the future.

In addition to the aforementioned approximations, additional numerical errors arise from round-off, mesh resolution, etc.

Volatiles present in the mantle plume, although not modeled here, are implicitly considered in the viscosity values, as we assume that they reduce the asthenospheric viscosity.

Our simulations show the plume conduit being bent from the vertical by advection from the ambient mantle wind, and show strong dragging of the ponded plume material by the moving overlying plate. These advection effects prevent the formation of an upstream stagnation bulge of plume material. This might not be true in the real Galápagos region, owing perhaps to a low viscosity layer (localized weak region) confined between the lithosphere and the lower asthenosphere. The lack of robust estimates for the hotspot swell volume-flux (owing to the presence of the GSC which adds great complexity to the bathymetry), might be yielding underestimations the real buoyancy flux. There is a chance that the real plume, being somewhat more powerful, actually produces upstream ponding and therefore volcanism manifests right above the conduit, and perhaps slightly upstream. The work by *Villagomez et al.* [2014] shows that volcanism (Fernandina, Isabela) manifests above a low velocity anomaly, but also reveals plume conduit advection, with bending in a direction oblique to plate velocity; the overall flow pattern seems complex, also perhaps confirmed by the work of *Mittal and Richards* [2017] suggesting melt transport in a direction perpendicular to the plate motion.

The plume partial melting and magma production are considered unimportant in a first order calculation of dynamic topography, owing to: (i) narrowness of the melting region when compared to the full plume strip width (as pointed out by *Ribe and Christensen* [1999]), and (ii) virtually unaffected total vertical upward forces (when viewed from/experienced by the upper crust). The most important effect of plume melts on topography is considered to be the localized weakening of the lithosphere arising from magma transport through it (weakening produced by melt-induced fracturing and heating), as suggested by Tushar Mittal (personal communication). These effects should tend to enhance the short-wavelengths of the topographic swell, locally above the region intruded by plume-derived melts.

3.6 Conclusions

1. Plate motion reconstructions, hotspot dynamic topography, crustal relaxation and magmatic production allow for an estimation of the subsidence undergone by the rock mass composing the Carnegie Ridge saddle point. These estimates are partially based on geodynamic theory of viscous fluids and elasticity, but also on detailed bathymetric observations and analysis. These estimates yield an expected amount of subsidence of about ~2 km occurring during the last ~13 Ma. Because the present-day depths of the region are in the range 2-2.5 km, this assessment shows that the present-day Carnegie Ridge region might have been emerged back then, and might perhaps have hosted land living species for a few (<5) million years.

2. Given the plate-hostpot relative velocity, these conclusions may be feasibly extended to the west Carnegie Ridge (between the saddle point and the Galápagos archipelago) at the corresponding times in regard to the relative plate velocity. Similarly but perhaps with more uncertainty, they can be extended to the east Carnegie Ridge from the saddle point toward the Nazca - South America subduction trench, with the Galápagos mantle plume impinging under the west South American trench perhaps ~30 Ma ago.

3. The westward migration and evolution of species on currently-submerged paleo-archipelagos along the Carnegie Ridge is plausible when considering the geophysical context of the Galápagos and Carnegie Ridge development, which was greatly influenced by age-dependent topography and the dynamic hotspot swell on the Nazca plate as it moved over the Galápagos mantle plume. This is important in the context of what is already known about biological evolution in the Galápagos platform area, as shown for example by *Geist et al.* [2014], *Ali and Aitchinson* [2014], *Parent et al.* [2008]; as it extends the logical framework to a much larger geographical area and a much longer time span.

3.7 Acknowledgements

We thank Stephen Thompson and Charles Paffenbarger at UC Berkeley, for being helpful and friendly system administrators, who provided technical support on the local cluster usage, crucial for our numerical simulations debugging.
We also thank the Texas Advanced Computing Center for their formal, prompt and helpful technical support on the Stampede cluster usage, without which much of the numerical work would not have been possible.
We are grateful for the ASPECT software community, Wolfgang, Timo, Rene, Julianne, J. Naliboff, and a long list of people who were kind in answering questions throughout the project.
We thank David Sandwell for directing us to the Scripps (UC San Diego) bathymetric database (available at http://topex.ucsd.edu/cgi-bin/get_data.cgi.).
We also thank Denis Geist for his openness to discussion and his overall support.
This work was supported by CONICYT Chile, the US National Science Foundation and the Esper Larsen Fund at UC Berkeley.

3.8 Appendix

3.8.A Benchmark to *Ribe and Christensen* [1994] model

The parameters employed in our benchmark are, when possible, exactly the same as in *Ribe and Christensen* [1994] work. Beyond this, there are some incompatibilities between their model and our one:

1) Their model's lower boundary (z=0) condition for velocity enforces zero horizontal velocity on that surface, and free vertical velocity (mass flow across the boundary), this means, $v_x=v_y=0$ and v_z free.
Our model has v_x, v_y, v_z all free.

2) Their model 's temperature on the lower boundary (z=0) uses a boundary condition of the third kind, i.e. a Robin B.C. Our model uses a simpler, Dirichlet boundary condition. The difference is the extra term with the Biot number they consider.

3) For the velocity boundary conditions on the upstream/downstream vertical walls, our model uses a Couette flow as prescribing the upstream inflow and downstream outflow. In their work, it is unclear what type of velocity boundary conditions are employed on those walls.

4) It is unclear what exact viscosity structure was used in their model.

Beyond these model incompatibilities, their model was run until reaching a steady state (unspecified time). Our model snapshot shown here is evaluated at 30 Ma after the initial condition, and has not quite reached a steady state.

Ribe and Christensen [1994]

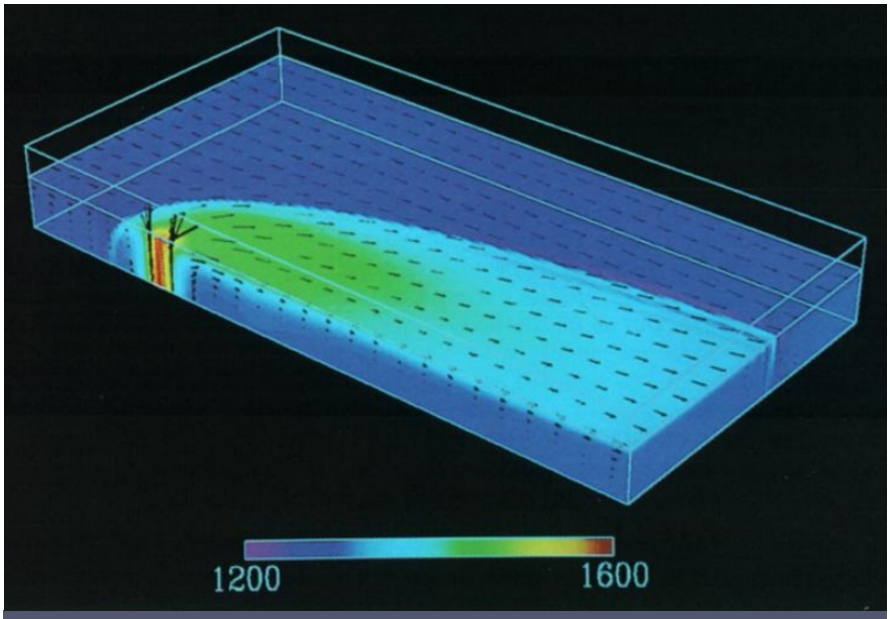

Our model

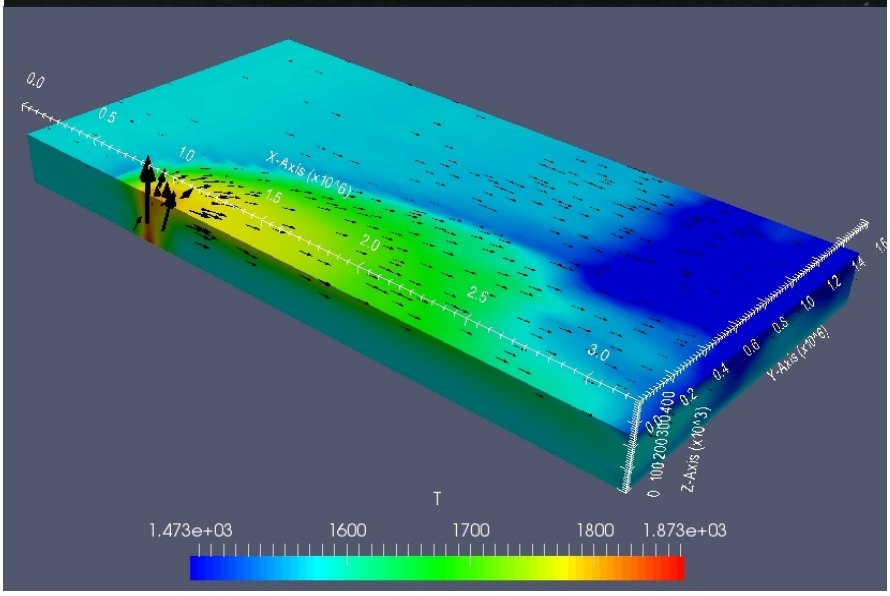

Figure 3.A1. Benchmarking comparison 1: temperature field with color scale between 1473 ºK (1200 ºC) - 1873 ºK (1600 ºC). Although the color scale ranges are the same, the color maps are different, and that explains part of the notable discrepancy in the upstream region. The velocity field is affected by the plume spreading.

Ribe and Christensen [1994]

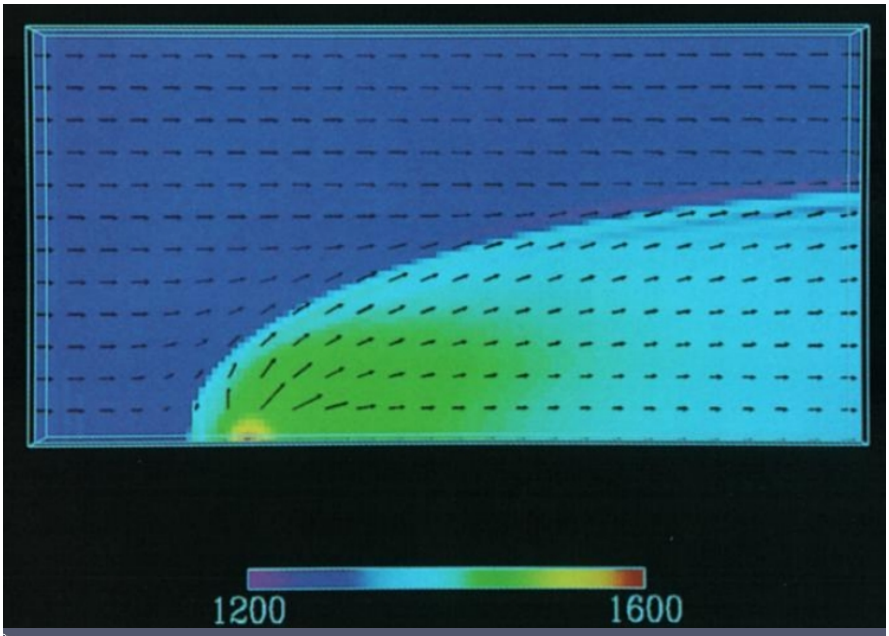

Our model

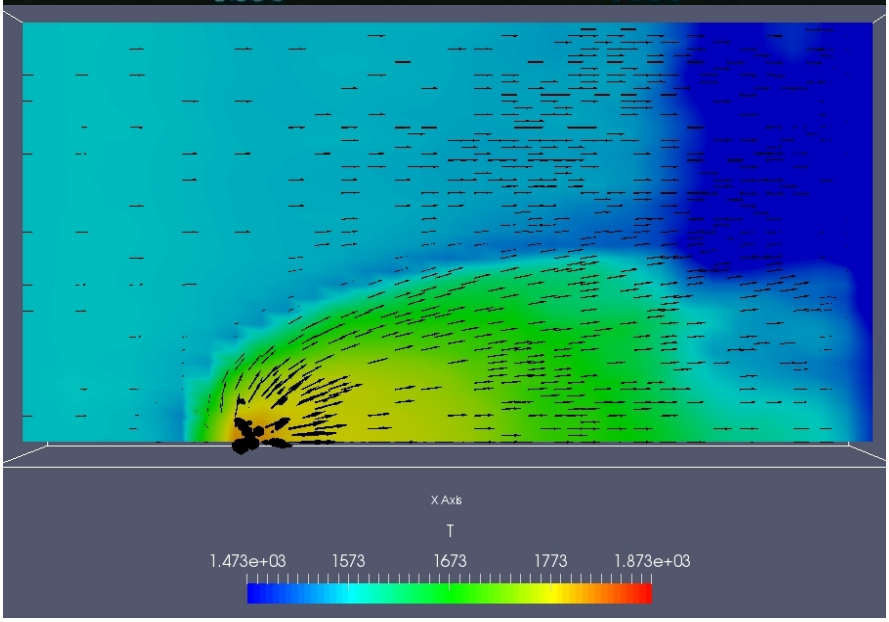

Figure 3.A2. Benchmarking comparison 2: temperature field with color scale between 1473 ºK (1200 ºC) - 1873 ºK (1600 ºC). Although the color scale ranges are the same, the color maps are different, and that explains most of the notable discrepancy in the upstream region (most of the light blue region in our model would become blue in the R&C color scale). The velocity and temperature fields look highly coupled.

3.8.B Additional figure for the area

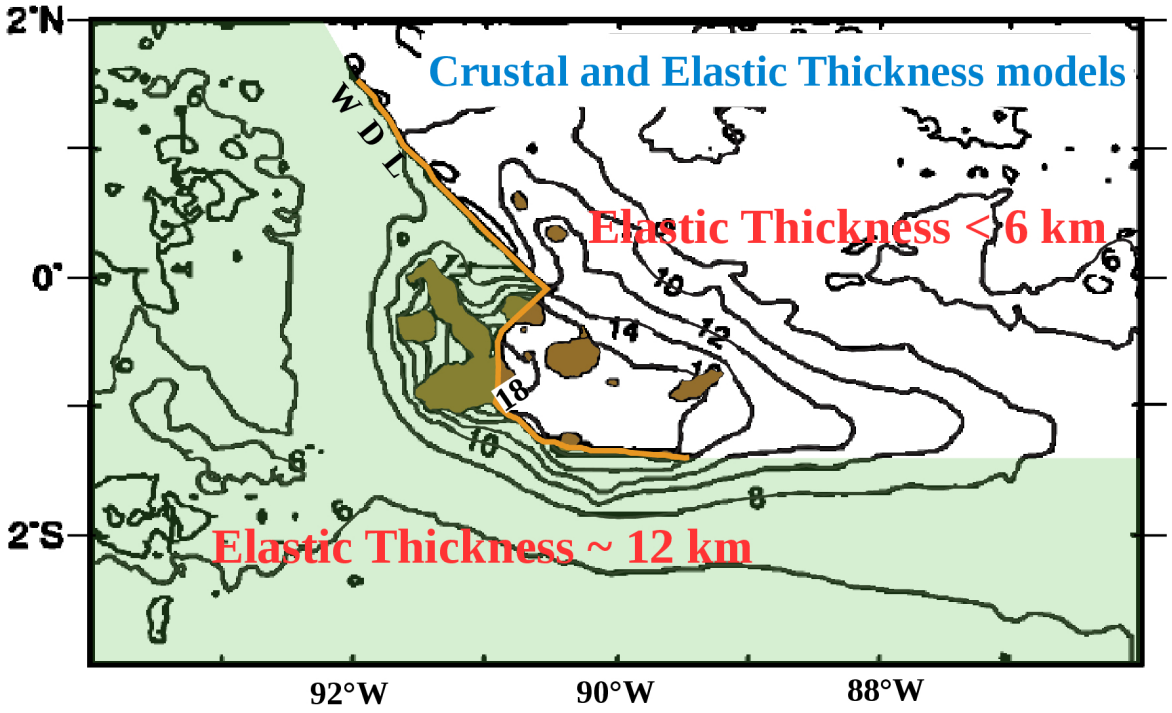

Figure 3.B1. Crustal thickness and Elastic thickness models from *Feighner and Richards* [1994] (combining their figures 12(a) and 13(a)). The crust on Nazca plate, having a background thickness of ~6 km, is substantially thicker under the Galápagos platform region, with a maximum thickness of ~18 km. The elastic thickness exhibits essentially two major domains: a thin lithosphere of thickness < 6 km (white area) and a thick lithosphere of thickness ~12 km (light green area), likely separated by deep lithospheric faults and the Wolf-Darwin Lineament (WDL) as suggested by *Feighner and Richards* [1994].

The results of this figure are accurate in the archipelago's platform region and vicinity and towards the east along the hotspot track, also subjected to the original shipborne gravimetric mapping lines. Nevertheless, on the thick lithosphere domain (light green area), some age-dependence of the lithospheric thickness (here unacknowledged) must exist, as expected from global data analysis (*Watts* [1978], *Watts and Daly* [1981]). The discontinuity effects of the 91 ºW transform also seem to be missing in the model.

3.9 References

Ali, R. and J. Aitchinson (2014), Exploring the combined role of eustasy and oceanic island thermal subsidence in shaping biodiversity on the Galápagos, *J. Biogeography*, v41 , 7 , 1365-2699 .

Barckhausen, U., C. R. Ranero, R. von Huene, S. C. Cande and H. A. Roeser (2001), Revised tectonic boundaries in the Cocos Plate off Costa Rica: Implications for the segmentation of the convergent margin and for plate tectonic models, *J. Geophys. Res.*, 106, 19,207 – 19,220.

Christie, D., R. Duncan, A. McBirney, M. Richards, W. White, K. Harpp, and C. Fox (1992), Drowned islands downstream from the Galápagos hotspot imply extended speciation times, *Nature*, v.355, 246-248.

Davies, G. (1988), Ocean bathymetry and mantle convection: 1. Large-scale flow and hotspots, *J. Geophys. Res*., 93, B9,10,467-10,480, DOI: 10.1029/JB093iB09p10467.

Detrick, R.S. & Crough, T. (1978) Island subsidence, hot spots, and lithospheric thinning. *J. Geophys. Res.*, 83, 1236-1244.

Johnson, H. P., and R. L. Carlson (1992), Variation of sea floor depth with age: A test of models based on drilling results, Geophys. Res. Lett. 19, 1971–1974

Feighner, M., and M.A. Richards (1994), Lithospheric structure and compensation mechanisms of the Galápagos Archipelago, *J. Geophys. Res.*, 99, 6711-6729.

Feighner, M., and M.A. Richards (1995), The fluid dynamics of plume-ridge and plume-plate interactions: An experimental investigation, *Earth and Planetary Sc. Lett.*, 129, 171-182.

Geist, D. J., H. Snell, H. Snell, C. Goddard, and M. Kurz (2014), A Paleogeographic Model of the Galápagos Islands and Biogeographical and Evolutionary Implications, in *The Galápagos: A Natural Laboratory for the Earth Sciences* (eds K. S. Harpp, E. Mittelstaedt, N. d'Ozouville and D.W. Graham), John Wiley & Sons, Inc, Hoboken, New Jersey, doi: 10.1002/9781118852538.ch8.

King, S. D., and C. Adam (2014) Hotspot Swells Revisted, *Phys. Earth Planet. Int.*, 235, 66-83, DOI: 10.1016/j.pepi.2014.07.006.

Kurz, M.D. & Geist, D.J. (1999) Dynamics of the Galápagos hotspot from helium isotope geochemistry. Geochimica et Cosmochimica Acta, 63, 4139-4156.

Mittal T. and M.A. Richards (2017), Plume-ridge interaction via melt channelization at Galápagos and other near-ridge hotspot provinces, *Geochem. Geophys. Geosyst.* v18, 4, 1711–1738.

Orellana-Rovirosa, F., and M.A. Richards (2015), Evidence and models for lower crustal flow beneath the Galápagos platform, *Geochem. Geophys. Geosyst.*, 16, doi:10.1002/2015GC006136.

Orellana-Rovirosa, F., and M. Richards (2017), Rough versus smooth topography along oceanic hotspot tracks: Observations and scaling analysis, *Geophys. Res. Lett.*, 44, 4074–4081, doi:10.1002/2016GL072008.

Parent C., A. Caccone A and K. Petren (2008) Colonization and diversification of Galápagos terrestrial fauna: a phylogenetic and biogeographical synthesis. Philosophical Transactions of the Royal Society of London B: Biological Sciences 363: 3347-3361.

Ribe and Christensen (1994), Three-dimensional modeling of plume-lithosphere interaction, *J. Geophys. Res.*, v. 99, B1, 669-682.

Ribe. N.M. and U.R. Christensen (1999), The dynamical origin of the Hawaiian volcanism, *Earth Planet. Sc. Lett.*, 171, 517-531.

Richards, M., R. Duncan and V. Courtillot (1989), Flood basalts and hot-spot tracks: plume heads and tails, *Science,* v 246, 4926, 103-107, doi:10.1126/science.246.4926.103.

Richards, M., B. Hager and N. Sleep (1988), Dynamically supported geoid highs over hotspots: observations and theory, *J. Geophys. Res., v.* 93, B7, 7690-7708.

Sinton, C. W., D. M. Christie and R. A. Duncan (1996), Geochronology of Galápagos seamounts, *J. Geophys. Res*., 101, 13,689 – 13,700.

Sleep, N. (1990), Hotspots and Mantle Plumes' Some Phenomenology, *J. Geophys. Res.*, 95, n. B5, 6715-6736.

Sleep, N. (2002), Ridge-crossing mantle plumes and gaps in tracks, *Geochem. Geophys. Geosyst.*, 3(12), 8505.

Turcotte, D., and G. Shubert (2002), *Geodynamics*, second edition, Cambridge University Press, NY.

Villagomez, D., D. Toomey, D. Geist, E. Hooft, and S. Solomon (2014), Mantle flow and multistage melting beneath the Galápagos hotspot revealed by seismic imaging, *Nature*, 7, 151-156, doi:10.1038/NGEO2062.

Werner, R., K. Hoernle, U. Barckhausen, and F. Hauff (2003), Geodynamic evolution of the Galápagos hotspot system (Central East Pacific) over the past 20 m.y.: Constraints from morphology, geochemistry, and magnetic anomalies, *Geochem. Geophys. Geosys.*, v.4, 12, 1108.

Wilson, D. S., and R. N. Hey (1995), History of rift propagation and magnetization intensity for the Cocos-Nazca spreading center, *J. Geophys. Res.*, 100, 10,041 – 10,056.

Software:

ASPECT version 1.5.0 (*Bangerth et al.* [2017], *Kronbichler et al.* [2012]) published under the GPL2 license. A development by CIG (Computational Infrastructure for Geodynamics).

Google Earth software (version 7.1.8.3036), plus Gobal Sattelite-derived Gravity Anomaly http://topex.ucsd.edu/grav_outreach/.

Thank you.

Felipe Orellana Rovirosa
PhD dissertation
UC Berkeley
2017